MAGNETOTELLURIC AND TRANSIENT ELECTROMAGNETIC IMAGING FOR GEOTHERMAL RESOURCES IN ARUS-BOGORIA AREA IN KENYA

DANIEL STEPHEN WAMRIEW BED (SCIENCE)

I56/CE/28358/2013

A thesis submitted in partial fulfillment of the requirements for the award of the Degree of Master of Science (Physics) in the School of Pure and Applied Sciences of Kenyatta University

March 2019

DECLARATION

This thesis is my original work and has not been presented for the award of a degree or any other award in any other University.

Daniel S. Wamriew Signature …… Date …….

Department of Physics

This thesis has been submitted for examination with our approval as University supervisors.

Dr. Willis J. Ambusso Signature…… Date …….

Department of Physics

Kenyatta University

Dr. Githiri J. Gitonga Signature…… Date …….

Department of Physics

Jomo-Kenyatta University of Agriculture and Technology

DEDICATION

To my beloved mother, Jane Atieno, the sole patient explorer; the world is beautiful because you live.

ACKNOWLEDGEMENTS

Firstly, I would like to express my sincere gratitude to my supervisors Dr. W. J. Ambusso and Dr. J. G. Githiri for their continuous support during this study; for their patience, motivation, and immense knowledge. Their guidance helped me in all the time of research and writing of this thesis.

Besides my supervisors, I would like to thank the rest of my thesis committee of Physics Department Kenyatta University led by Prof. Singh, for their insightful comments and encouragement, but also for the hard questions which incented me to widen my research from various perspectives. In particular, I am grateful to Dr. L. O. Ochoo of Physics Department Kenyatta University for enlightening me on the first glance of research.

My sincere thanks also go to Dr. S. M. Simiyu, Mr. J. Lagat, and Dr. B.M. Linyiru, of Geothermal Development Company who provided me an opportunity to join the Geothermal Development Company (G.D.C) team as intern, and who gave me access to the equipment, data, software and other research facilities. Without their precious support it would not have been possible to conduct this research.

In a very special way, I would like to thank the Geophysics team from G.D.C led by Mr. Charles Muturia and Mr. Raymond Mwakirani for sharing with me their vast geophysical exploration knowledge and experience both in the office and out in the field during exploration. I could not forget Mr. Nicholas Kipoipoi who was not only our wonderful driver but also broke the boredom with his timely yet so hilarious humor. I am also greatly indebted to Mr. Charles Muturia who came in handy both as a mentor and a confidant.

I thank my fellow classmate and roommate Mr. Joseph Ogidi for the stimulating discussions, for the sleepless nights we were working together, and for all the fun we have had during our study years.

I would like to thank my friend Ms. Esther B. for keeping me company long hours into the night and for the moral and financial support she offered me during this research work. You have really stretched the cost of friendship to the extremes.

In a very special way; I would like to thank my loving family for supporting me spiritually throughout writing this thesis and my life in general. Brothers Mr. John Kennedy, Mr. Elijah Wamriew and sisters Ms. Essy J., Ms. Grace N. and Ms. Cate O.; your magnificent contributions I could not have done without. You are so amazing. Not forgetting the little Ms. Vanessa M., Ms. Malia A. and Mr. Alvin M. whose humor, joy and abundant energy always kept me motivated. You were in deed bundles of joy and hope to see you grow to greatness.

And to the Almighty God who gives life, health, strength and wisdom, Glory and Honor be.

May Almighty God bless you all abundantly.

TABLE OF CONTENTS

LIST OF FIGURES

LIST OF ACRONYMS

1D	One dimension
2D	Two dimensions
3D	Three dimensions
AVG	Abstand Verstarung Grosse
CGG	Compagnie Générale de Géophysique
DC	Direct Current
EDI	Electrical Data Interchange
EM	Electromagnetic
GDC	Geothermal Development Company
GDP	Geophysical Data Processor
GPS	Global Positioning System
IGSN	International Gravity Stations Network
KRISP	Kenya Rift International Seismic Project
KRV	Kenyan Rift Valley
m.a.s.l	metres above sea level
m.b.s.l	metres below sea level

MT	Magnetotelluric
MW	Megawatt
NLCG	Non-Linear Conjugate Gradient
NOCK	National Oil Corporation of Kenya
TEM	Transient Electromagnetic
UNDP	United Nations Development Program
UNU-GTP	United Nations University Geothermal Training Program

MEANING OF SYMBOLS

CO_2	Carbon Dioxide
$\boldsymbol{B}$ (T)	Magnetic induction
$\boldsymbol{D}$ (Cm^{-2})	Electric displacement
$\boldsymbol{E}$ (Vm^{-1})	Electric field intensity
F (Hz)	Frequency
$\boldsymbol{H}$ (Am^{-1})	Magnetic field intensity
$i = \sqrt{-1}$	Imaginary number
I (C)	Electric current
$\boldsymbol{J}$ (Am^{-2})	Electric current density
k (m^{-1})	Propagation constant (Wave number)
M_q	Length of the imaginary part of the induction arrow
M_r	Length of the real part of the induction arrow
t (s)	Time
T (s)	Period
x, y and x', y'	Reference frame and reference frame rotated through an angle
$\hat{Z}$ (Ω)	Impedance tensor (2 x 2 matrices)
$\Im$	Imaginary part of the tipper
$\Re$	Real part of the tipper
$\mathcal{T}$	Tipper
δ (m)	Electromagnetic skin depth
ε (Fm^{-1})	Electric permittivity
ε_0 (Fm^{-1})	Permittivity of free space = 8.85×10^{-12}

η (Cm^{-3})	Electric charge density of free charges
μ (Hm^{-1})	Magnetic permeability
μ_0 (Hm^{-1})	Permeability of free space = $4\pi \times 10^{-7}$
ρ (Ωm)	Specific resistance (resistivity)
ρ_a (Ωm)	Apparent resistivity
σ (Sm^{-1})	Electric conductivity
φ	Porosity expressed as a fraction per unit volume of rock
ω ($rads^{-1}$)	Angular frequency
ϕ (^{o})	Impedance phase

ABSTRACT

Details of the Earth's subsurface are largely obscured because it's difficult to make direct observation of the Earth's subsurface. Geophysical exploration methods, however, provide a means of remotely examining the Earth's subsurface. This study therefore seeks to image for geothermal prospects in Arus-Bogoria area using Magnetotelluric (MT) and Transient Electromagnetic (TEM) methods. MT method has the greatest exploration depth whereas TEM has the best resolution at shallow depths. MT and TEM measurements were conducted in Arus-Bogoria geothermal prospect area and the resulting data analyzed and interpreted. The MT data were corrected for static shift using TEM data from stations in their proximity and an integrated data set obtained. WinGlink interpretation software was used to perform 1D inversion on the TEM and MT data and the results obtained used to plot iso-resistivity maps and cross-sections for Occam inversion at different elevations to describe the resistivity distribution. Two-dimensional resistivity models were generated using five profiles cutting across the study area. The results from the resistivity analysis indicate that the hotter reservoir conditions are to the Northwest (NW) around Molo Sirwe area. This area is potentially a good high-temperature area. This may well be the upflow of the geothermal system. Resistivity distribution confirms a possible geothermal system up flowing to the NW and is structurally controlled. TEM imaging shallower depth indicates a small irregular relatively resistive anomalous body that may be gas reservoirs; this may explain the numerous gas emitting holes in Mukuyuni area. The potential area determined using resistivity anomaly is about 36 km^2 to the west of the study area. More infill data however need to be collected. Feasibility studies to be conducted to determine whether the naturally existing hot springs and gas reservoirs are commercially viable.

CHAPTER ONE

INTRODUCTION

1.1 Background to the study

Arus-Bogoria is one of the geothermal prospects located along the central Kenyan Rift Valley (KRV) 2 km north of the equator and bound by narrow graben to the West and a half graben to the East. It is bounded by latitude 0º00' and 0º30'N and longitudes 35º50'E and 36º50'E. Figure 1.1 shows the location of Arus - Bogoria prospect (outlined) within KVR.

Geothermal resource invariably occurs in trans-tensional and extensional tectonic environments, which for a long time have been the main targets in geothermal resource exploration. Interactions between normal faults and strike-slip faults, acting either as strain relay zones have led to considerable interest in exploration of geothermal resources since they often lead to fault-controlled dilatational corners with improved permeability and thus have the potential to geothermal prospects. This is classical of Arus geothermal prospect. The geothermal fluids in Arus appear to be controlled by major faults and subsidiary faults. The fault breaks into multiple splays or horsetails as it loses displacement. Greater number of intersections of faults and the higher concentration of faults generates a broad zone of highly fractured and consequently highly permeable rocks, which enhances upward movement of geothermal fluids.

There are seven types of geothermal manifestations in Arus geothermal prospect which include fumaroles, boiling springs, bubbling springs, mud pools, steam jets, altered ground and travertine deposits. These are biased to a fault scarp that bounds the Molo

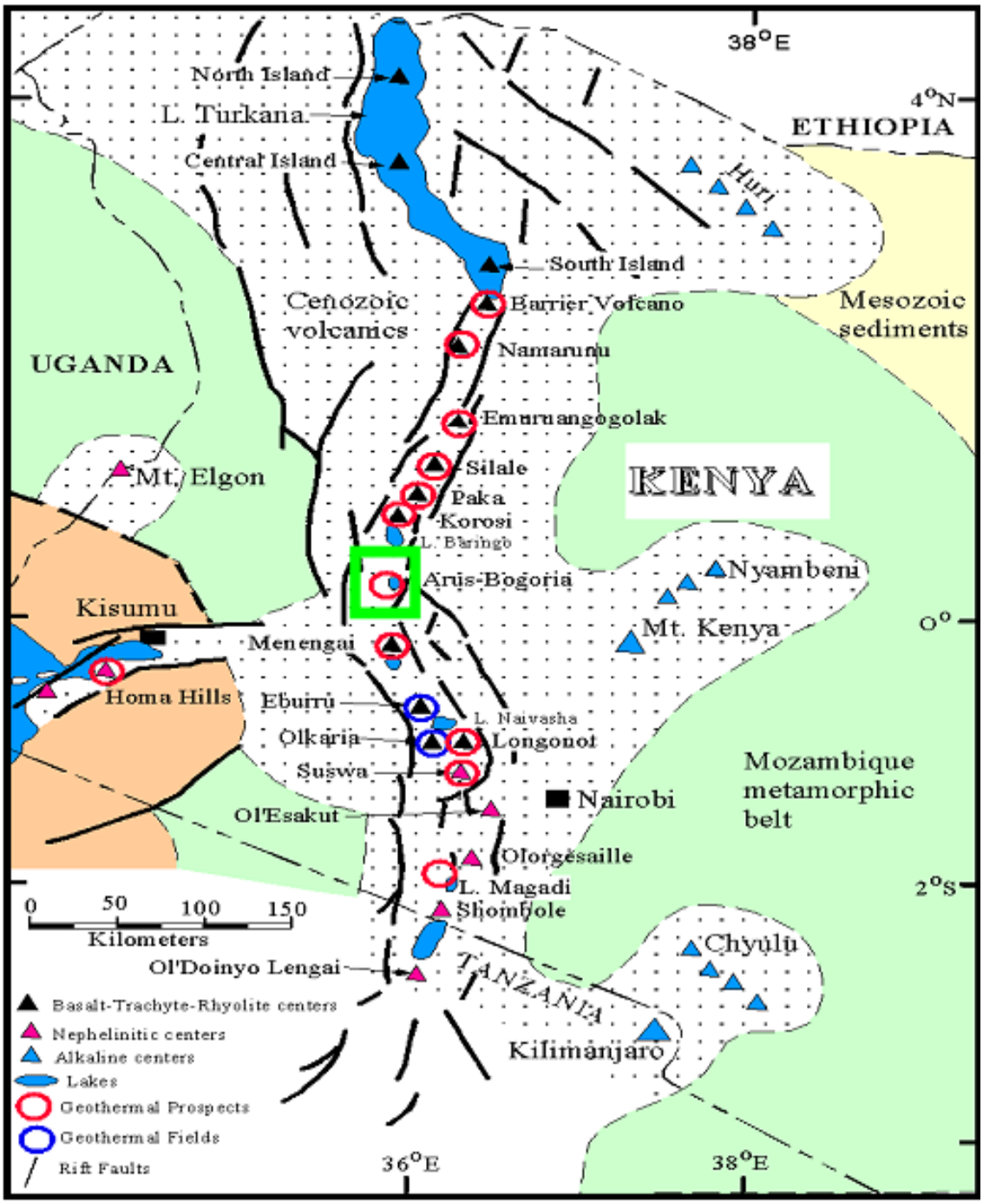

Figure 1.1: Location of Arus-Bogoria prospect within KVR (modified from Mariita, 2003)

River on the Northern zone of the prospect where they delineate the upflow zone. Vents oozing carbon dioxide gas are also present along fault zones in the Mukuyuni and Pombo areas and are significant in determining the kind of geothermal system that is present in Arus. The occurrence of the manifestations in linear array is an indication of structurally controlled activities in the prospect area.

MT and TEM measurements were conducted so as to give worthwhile information on the presence, size, and location of geothermal systems in this area. MT method uses the naturally occurring earth's EM field as its source of power. The time varying earth's natural magnetic field induces fluctuating electrical currents in the subsurface of conductive earth. If the signals of the time varying magnetic field as well as the fluctuating electrical currents on the surface of the earth are measured, it is then very possible to correlate this to the resistivity of the rocks below the measuring site. The probing depth relates to the frequency of the signal, with low frequencies reaching deeper levels. Thus, frequencies of 0.00001 - 10 Hz are used for deep crustal investigations, while higher frequencies, like 10 - 1000 Hz, for the upper crust (Lúdvík, 2009). In TEM, a time-varying man-made half-duty square wave current is sent through a wire loop placed on the surface of the Earth and the resulting decaying magnetic fields interpreted for subsurface electrical resistivity.

According to Hersir and Björnsson (1991), electrical resistivity of the subsurface is a crucial parameter for the characterization of geothermal settings since it relates directly to the properties that characterize geothermal systems such as salinity, porosite, permeability, level of hydrothermal alteration of the rocks and temperature.

EM methods for geothermal exploration are most suitable for geothermal systems with a system of faults and/or fractures filled with conducting geothermal fluids and altered rocks (Munoz, 2014).

1.2 Geological and Tectonic Setting

Phonolites and basalts are the major lithological units in Arus and cover large areas of the prospect although sediments and tuffs are also apparent. The geology on the eastern zone and western margin are characterized by phonolites that show discrepancy in their appearance and composition. The phonolites associated with the Bogoria half graben appear greatly dissected by NNE-SSW trending faults leaving steep scarps which clearly reveal similar alignment. The lavas are evidently fissure eruptions with no association to any central volcano. Eruption centres are however present and appear as bulges along the identified fissure feeder zones.

The phonolites in the central region appear much older and are associated with the Molo graben whose major trend is N-S. A shield volcano of basaltic composition, the Goitumet volcano is situated in the southern region of the study area near Lomolo. The lava is fresh hard and vesicular with olivine mineralization being evident in the groundmass. Coincidentally most of the active gas emitting vents is located within this formation. The rock exhibits fracturing, is unvegetated and characterized by lava tongues which exude it. Deep lava tubes and caves typical of many basalt formations are quite obvious in this formation.

The general trend of many structures within Arus prospect is NNE-SSW in the east and N-S in the central and western zone. The NNE-SSW normal fault forms a half graben

which is significant as many of the Lake Bogoria hot springs fall in its locality. The Molo graben constitutes the N-S trending faults and it is within this narrow graben that the fault controlled Arus steam jets, fumaroles and bubbling springs are found.

Figure 1.2 below shows the geological structure of Arus-Bogoria area.

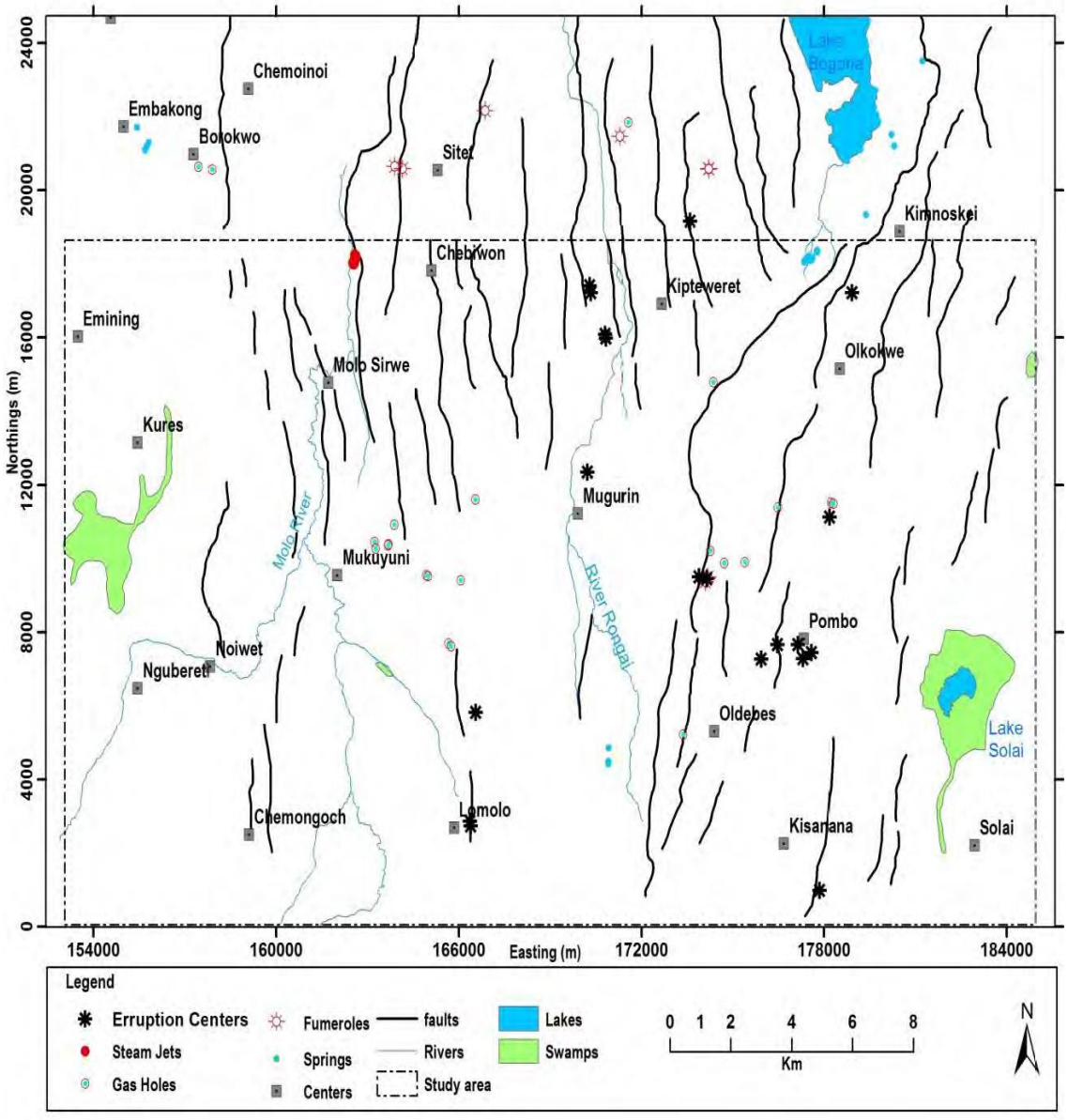

Figure 1.2: Regional geological structures (Modified after Zieke and Strecker 2009)

1.3 Statement of the Problem

Previous geophysical studies at Lake Bogoria did not cover adequately the area around Arus. More recent surveys involved data collection in part of Arus but there were still large data gaps for a conclusive delineation of the geothermal resources in the prospect area. There was therefore need for collection of infill data in order to reasonably understand the resistivity structure beneath the prospect area.

The techniques used in prior studies were to a large extent Direct Current resistivity method with some enhancement using Magnetotelluric methods. The Direct Current resistivity methods could not penetrate to sufficient depths especially due to the limitation on the length of the current cables and presence of resistive lava piles near the surface. Magnetotelluric studies suffer static shift problems which in this study were corrected by carrying out Transient Electromagnetics soundings on the same points where Magnetotelluric was conducted.

The Magnetotelluric method is more reliable in mapping deeper levels and hence the need to understand the shallow resistivity structure as well. A combination of MT and TEM is expected to resolve the resistivity structure from shallow depths to deeper levels.

1.4 Objectives

1.4.1 General Objectives

The general objective of this study is to image for geothermal prospects in Arus-Bogoria area using Magnetotelluric and Transient Electromagnetics methods.

1.4.2 Specific Objectives

The specific objectives for this study are:

i. To carry out Magnetotelluric and Transient Electromagnetics measurement of Arus-Bogoria area
ii. To develop resistivity models of the subsurface of Arus-Bogoria area
iii. To interpret models in order to delineate intrusions of geothermal system in Arus–Bogoria area.

1.5 Rationale of the study

The Magnetotelluric method is based on induced electromagnetic fields whose sources are outside the earth and therefore are not affected by terrain and electrode polarization, as is the case for Direct Current methods. It thus overcomes the challenges experienced by Direct Current methods. Through its use of a wide range of frequencies it is capable of probing the subsurface from shallow to much deeper levels. The use of Transient Electromagnetic (TEM) alongside ordinary Magnetotelluric techniques aids in enhancing the integrity of near surface resistivity structure.

The acquisition of additional data within Arus improved the existing datasets for better analysis and interpretation of the resistivity structure. This aids in the development of a more data constrained model of the subsurface for addition to existing datasets.

With better cross-sections and resistivity iso-maps, the features of the system and their characteristics are well understood.

CHAPTER TWO

LITERATURE REVIEW

2.1 Previous geophysical work in Arus-Bogoria area

The central Kenya Rift Valley and in particular the Lake Bogoria basin has been the target of several geological and geophysical investigations.

Glover (1972) collected a large number of water and steam samples from Lake Bogoria area and concluded from his analytical data that a relatively large and homogeneous body of warm water lies under much of the area. Griffiths (1977) in his dissertation did a comparative trace element study of the volcanic products in the area.

Geological work in the area with bias in geothermal exploration was carried out by Geotermica Italiana Srl (1987) in their Menengai-Lake Bogoria reconnaissance report but dwelt mainly on Menengai caldera and did not discuss geological and structural set-up for development of the extensive anomalous geothermal manifestations in the Arus-Bogoria area.

Gravity analysis by Simiyu and Keller (2001) along an axial rift profile shows a series of positive gravity anomalies at Olkaria, Eburru, Suswa and Menengai geothermal fields. The gravity highs have been modeled as resulting from volcanic centers underlain by discrete mafic bodies having a density of 2.9 gm^{-3} which are presumed to be the heat sources for these geothermal fields.

Cross-rift gravity model by Mariita (2003) to the north of Lake Bogoria basin geothermal prospect at latitude 0.6^{o} N shows that this area is underlain by about 2-4 km

thick of low density (2.3 gm^{-3}) Miocene sediments and lavas but there is no evidence of volcanic anomalies which could probably be heat sources.

In 1977, Rooney and Hutton carried out MT studies in which they found out that within the Kenyan rift, the conductor is probably due to water saturation and high temperature.

Contrary to the results of the gravity analysis of the region by Simiyu and Keller (2001) and Mariita (2003), the geochemistry work by Karingithi (2006) indicates that a geothermal reservoir exists in Lake Bogoria basin. This reservoir is estimated to have temperature ranges between 115 to 425^{o}C and its upflow zone may be located in the area close to Arus steam jets, between Molo river and longitude 36^{o} E.

Lagat (2008) found that there exist several low to intermediate temperature fault controlled geothermal systems in the Arus-Lake Bogoria prospect and that the heat sources in both the Arus-Lake Bogoria prospect are associated with the thinning of the crust and shallow intrusives.

2.1.1 Seismic studies

The United States Geological Survey conducted seismic studies at Olkaria and Lake Bogoria in 1972 and located earthquakes of magnitude 2 or less that were restricted mainly within the fields along fault zones (Hamilton and Muffler, 1972). The resulting time distance plots indicated that Olkaria and Lake Bogoria areas are underlain by a three-layer volcanic sequence of about 3.5 km thick. A layer with a P-wave velocity of 6.3 kms^{-1} in turn underlies this sequence. Interpretation of their model shows a structure

with velocities higher than the average upper crustal velocities within the rift. In addition, fewer seismic events were recorded in Lake Bogoria in comparison with Olkaria.

During the KRISP Project, the University of Leicester conducted micro-seismic monitoring at Lake Bogoria geothermal prospect (Young *et al.,* 1991). Results from here, too, indicated that seismicity is confined to faulted zones. Some events were found to originate from the Menengai-Olbanita area to the south along the Solai axis. The geological and seismic results of this area showed that the Solai axis is still the most tectonically active system characterized by normal grid faulting with blocks generally tilting towards the east.

In 1986/87 a micro-earthquake network was setup in the Lake Bogoria region in an area of about 25 km diameter in the Molo graben, Ndoloita graben and Kamaech horst comprising of 15 recording stations. Results from the survey suggested that most of the activity was connected with older, larger faults of the rift flanks as opposed to the younger grid faults cross cutting the rift. The earthquake depth distribution showed that most activities occurred above a depth of 12 km and no ‘normal’ activity takes place below 15 km, implying a deep brittle-ductile transition zone. This would suggest that the Lake Bogoria area is less attractive as a geothermal resource. The surface manifestations there might be fissure related as a result of deep penetrating faults. It is also possible that the focus of these earlier studies was not confined to the geothermal investigations and thus the determined depths are more related to the general rift

rheology. Further, the area covered is too small to make a generalized statement. Hence more data needed to be collected.

Comparison with the seismicity observed by the 1994 Lake Baringo network (Tongue *et al*., 1994) shows a similar depth to the brittle-ductile transition in each area, but a greater depth of 10 km for the peak activity beneath Lake Bogoria. This may be a pointer to a higher geothermal gradient beneath the Lake Baringo basin. Low crustal velocities below the surface were identified from the inversion of the local P-wave arrival times indicative of activities of geothermal nature in the area. The decrease in velocity is most probably attributable to the presence of fluids and increased temperatures below the surface.

2.1.2 Gravity and Ground Magnetic

The Bouguer gravity data used in this review have been obtained from the unpublished report of Arus geothermal prospect by the Geothermal Development Company, Kenya (GDC) which was obtained from two sources. The main source was the University of Texas at El Paso's (UTEP) database. It is comprised of over 60,000 stations from East Africa, and a subset for the central Kenya rift was extracted from it. The second source was reports from other researchers for this part of the rift (Fairhead, 1976; Simiyu and Keller, 1997; Swain, 1992; Swain *et al.,* 1994; Swain *et al.,* 1981). These data have been reduced to Bouguer values using an average crustal density of $2.67 gcm^{-3}$ and adjusted to a common IGSN71 gravity datum. Figure 2.1 is a gravity map from the Arus- Bogoria region.

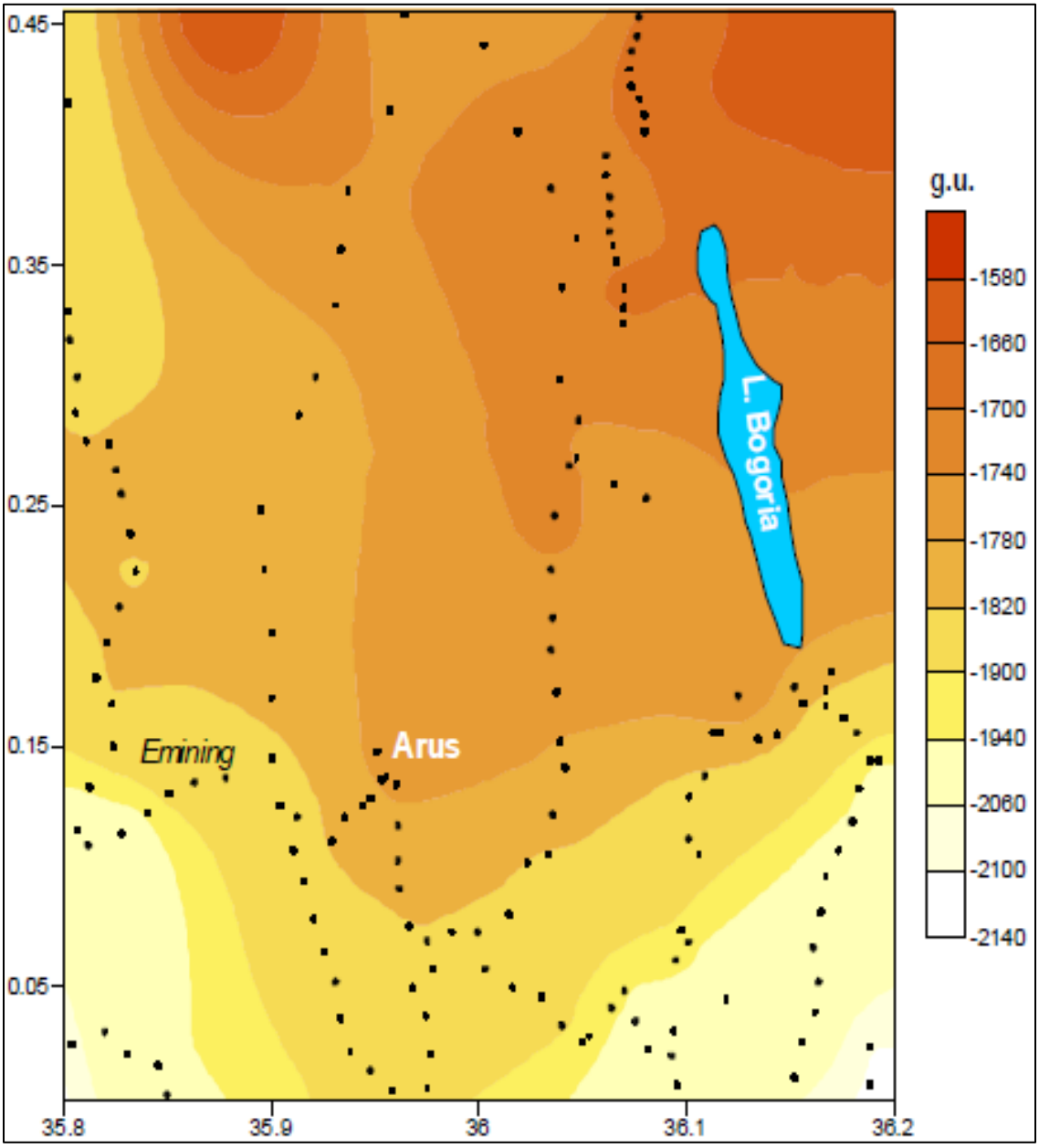

Figure 2.1: Bouguer anomaly of the area around Arus geothermal prospect (NOCK, 1987)

In the late 1980s a reconnaissance survey was conducted in the Menengai-Lake Bogoria region for the Ministry of Energy by the UNDP for geothermal energy investigations

(UNDP, 1986; UNDP, 1987). Analysis of this and earlier gravity results indicate a large positive anomaly, situated in the central part of the area running in N-S direction (Mariita, 2003). This could be related to the axial high anomaly which could be a source of heat for the geothermal system. The measured points however were too scattered, and the results could not give a comprehensive image of the localized anomalies.

In 1987 the Ministry of Energy, on behalf of the National Oil Corporation of Kenya, contracted CGG to carry out an aeromagnetic survey along the Rift Valley (NOCK, 1987). The data was collected at a terrain clearance of 2996 m.a.s.l. The northern part of the rift was found to be marked by a series of high amplitude magnetic anomalies. The wavelengths of these anomalies are less than 2.5 km, their amplitudes showing broad peaks reaching several hundred gammas and their shapes are either isometric or oval. This magnetic field is very typical of what is observed over basic volcanoes, i.e., basalts.

2.1.3 Resistivity

In the late 1960s DC-resistivity survey was done at the Lake Bogoria region for the East African Power and Lighting Company Limited. The aim of the survey was to outline reservoirs of thermal fluids at depth. Results indicated a complex resistivity pattern (Figure 2.2). High resistivity existed in the region south of Lake Bogoria over an area covered by an extensive sheet of rather impermeable phonolites that extend into the Lake Bogoria area. In the area with low to intermediate resistivities, the valleys are filled with recent sediments.

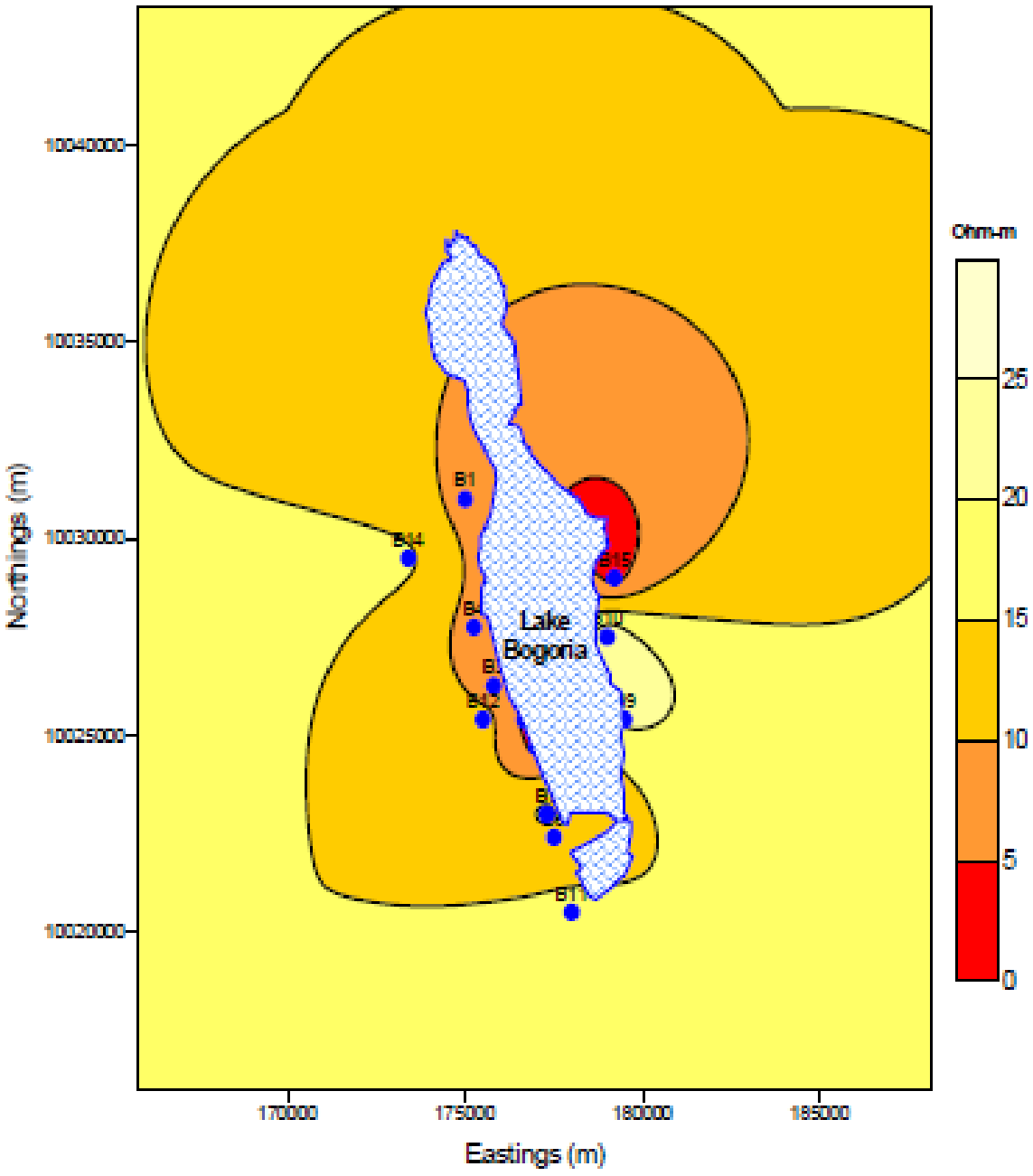

Figure 2.2: Direct Current resistivity map of the study area (NOCK, 1987)

Some of the low resistivities were also presumably connected with thermal waters but others (quite extensive) occurring in the vicinity of the lake were obviously connected

with deltaic silts, clays and saline beach deposits such as those at the northern end of the lake. Low resistivities were also observed and connected with the thermal fluids that are discharged in the Arus area on the Molo River.

The few measurements carried out near the hot springs showed low resistivities. Since discharge of thermal fluids occurs at all sides of the lake, this may indicate that the low resistivity area might be extensive. However, it is difficult to distinguish those due to thermal fluids from those due to sediments. But since, the lake forms a natural sink for the drainage of a large region; it is quite possible that the discharge features along the lake might be caused by extensive subsurface drainage of thermal fluids with potential sources found elsewhere. Previous results of Transient Electromagnetics and Magnetotelluric are shown below (Figure 2.3 and 2.4). Figure 2.3 shows Transient Electromagnetics resistivity map at 1000 m.a.s.l and figure 2.4 shows Magnetotelluric resistivity map at 2000 m.b.s.l.

From the TEM resistivity map at 1000 m.a.s.l (figure 2.3), a zone of low resistivity <16 Ohm-m predominantly covers the northern section of the plot at Marigat and were seen to spread southwesterly towards Arus. The low resistivities were also connected with the thermal fluids that are discharged around the Molo River. The map also shows the structural controls aligned in the NNE-SSW which is due to the trending faults in that area.

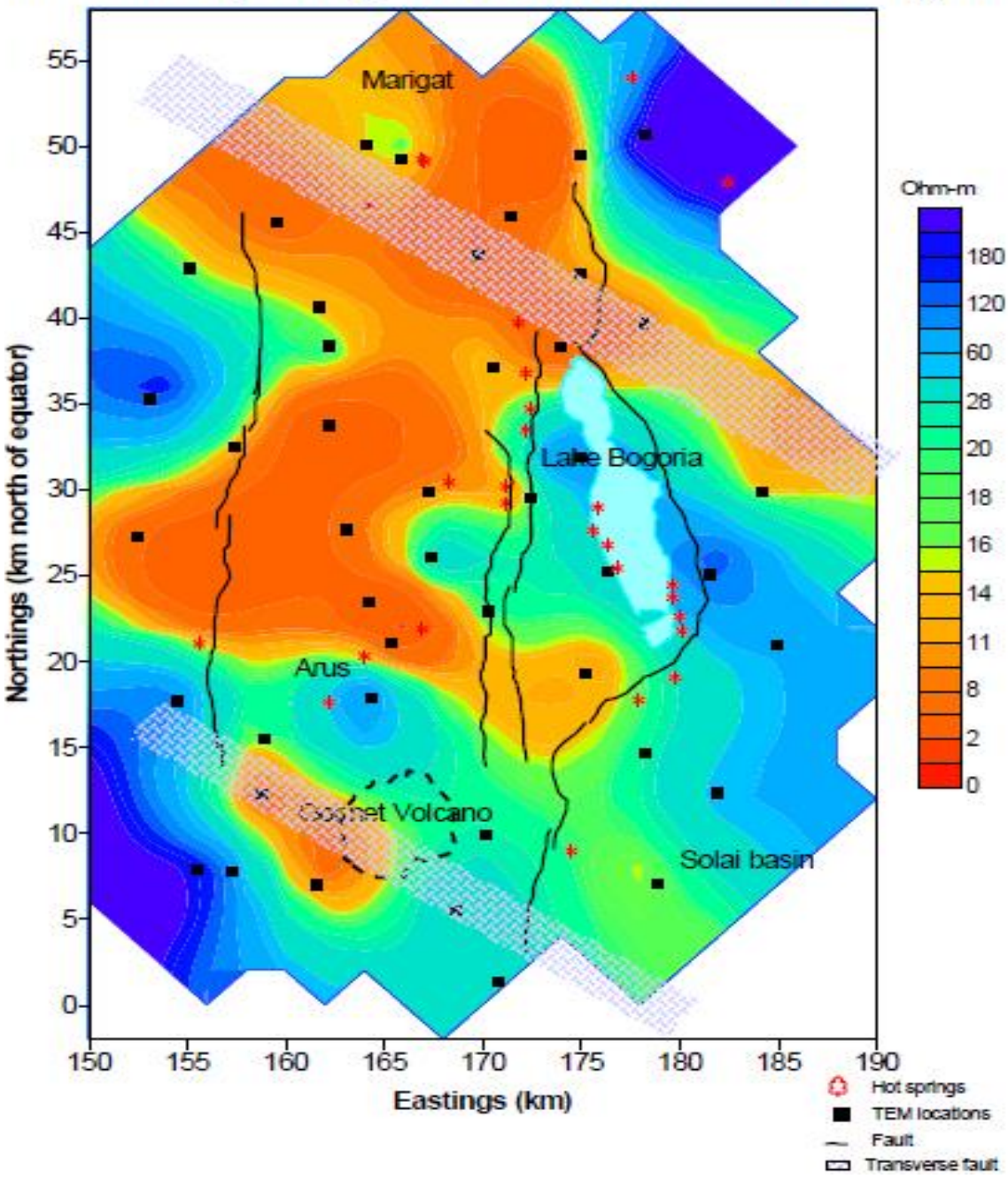

Figure 2.3: Transient Electromagnetics resistivity map at 1000 m.a.s.l (NOCK, 1987)

Deep MT resistivity imaging at 2 kilometres below sea level revealed a relatively uniformly spread resistivity with traces of lows around Lake Bogoria and on the western edge of the plot as well as at the northwest around Marigat (Figure 2.4 below). The low resistivity around the lake could be attributed to be as a result of extensive subsurface

drainage of thermal fluids. At the central part of Arus, a very high resistivity was mapped and was delineated to the source of heat at the Goimet Volcano. However, the MT points were too scattered such that it was difficult to give details of the localized anomalies.

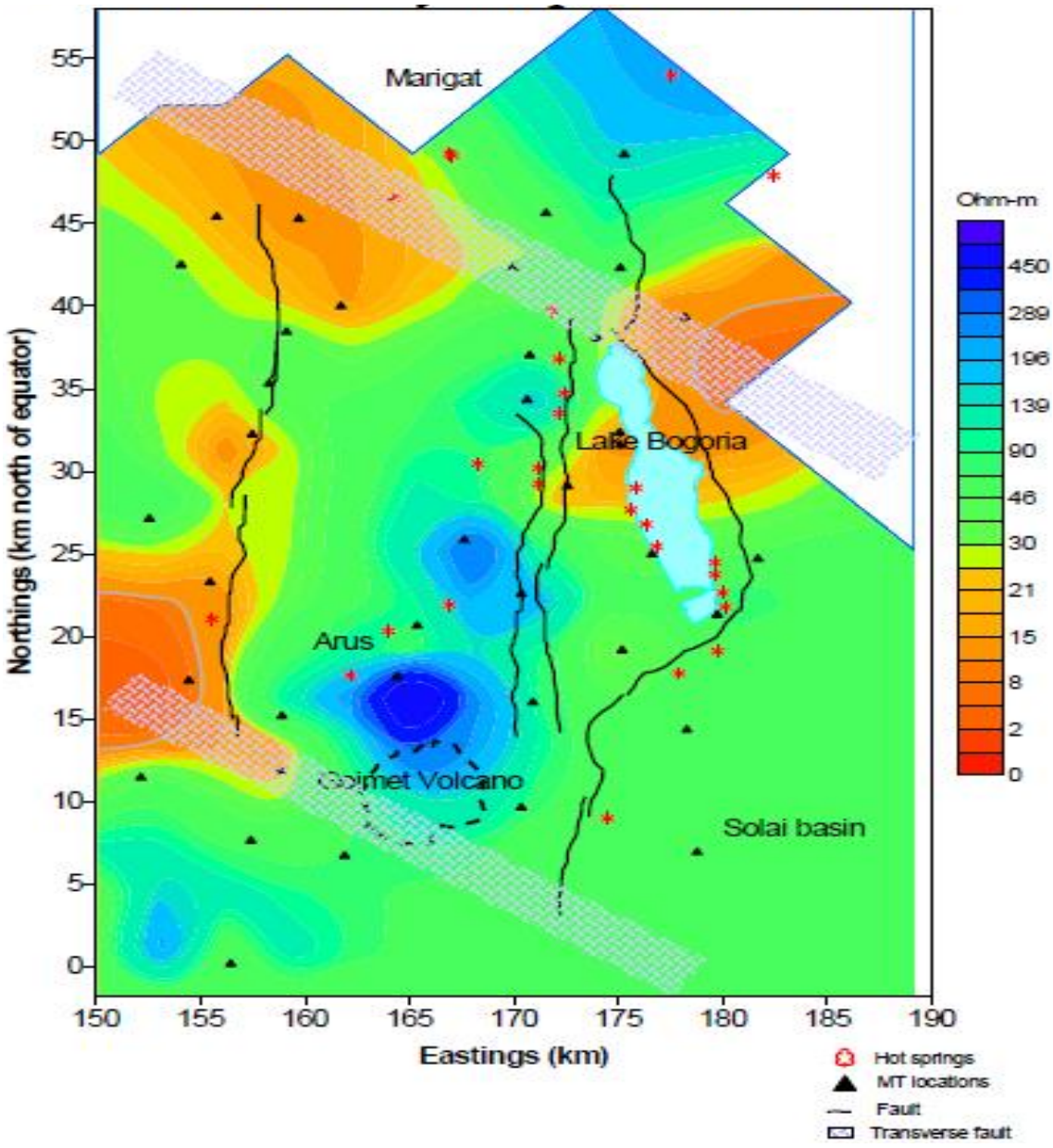

Figure 2.4: Magnetotelluric resistivity map at 2000 m.b.s.l (NOCK, 1987)

CHAPTER THREE

THEORY OF MAGNETOTELLURIC AND TRANSIENT ELECTROMAGNETIC METHODS

3.1 Theory of Magnetotelluric (MT)

MT uses the earth's natural electromagnetic fields to probe the subsurface resistivity structure of the earth. It is thus a passive geophysical exploration method as it relies on the earth's natural EM waves as its power source. The natural changes in the magnetic fields of the earth induce corresponding fluctuating electric/ telluric currents in the earth's subsurface in accordance with Faraday's law. The magnitude of this current depends on the resistivity of the rocks below. Both the electric and magnetic fields are measured on the surface of the earth in two orthogonal directions. The impedance tensor, which is the ratio of the electric and magnetic field, gives information about the conductivity of the subsurface. High frequency provides information about the near surface whereas the low frequency provides information about deeper lying structures. At frequencies higher than 1 Hz, the EM source originates from lightning discharges in the equatorial belt while low frequencies less than 1 Hz originate from the interaction between the earth's magnetic field and the solar wind.

MT data collection uses a combination of induction coil magnetometers and electric sensors that can detect changes in resistivity to great depths below the surface. The electric sensors are used to determine the electric field which is derived from measurements of the magnetic fields H_x, H_y and H_z in three orthogonal directions. The measured variations in magnetic and electric fields [$(E_x/H_y\ (\omega))$] in the earth gives

information about the subsurface resistivity structure. The EM waves are assumed to be planar components (the MT approximation, Vozoff, 1991). It follows that at a given period, only two horizontal electric components are necessary to describe any EM field component measured anywhere at the surface. The high frequency provides information about the shallow earth. The MT geophysical exploration method has the ability to investigate deep down to tens of kilometres and thus is the EM method with the greatest depth of exploration. The penetration depth of EM field below the subsurface is dependent on the conductivity structure of the earth as well as the period.

3.1.1 Elementary Electromagnetic Theory

To understand the propagation and attenuation of MT waves, we first describe Maxwell's equations that relate electric and magnetic vectors.

$$\nabla \times \boldsymbol{E} = -\frac{\partial \boldsymbol{B}}{\partial t} \qquad \text{(Faraday's Law)} \qquad (3.1)$$

$$\nabla \times \boldsymbol{H} = \boldsymbol{J} + \frac{\partial \boldsymbol{D}}{\partial t} \qquad \text{(Ampere's Law)} \qquad (3.2)$$

According to Faraday's Law the time variation in the magnetic field induce corresponding fluctuations in the electric field flowing in a closed loop with its axis oriented in the direction of the inducing field. This electric field then induces a secondary, internal magnetic field proportional to the total current flow in accordance with Ampere's Law. Ampere's Law equation represents two kinds of current flow, one $\boldsymbol{J}$ in which charge carriers flow through a medium without hindrance which is usually called ohmic, and another, $\frac{\partial \boldsymbol{D}}{\partial t}$ in which charge separation, and hence an opposing electric field, arises also known as displacement current.

3.1.2 Maxwell's Equations in Homogeneous Isotropic Medium

In Homogeneous isotropic medium;

$$B = \mu H, \qquad D = \varepsilon E \qquad \text{and} \qquad J = \sigma E \tag{3.3}$$

where σ is conductivity in Siemens.

Substituting Eqn. (3.3) in Eqns. (3.1) and (3.2); we get;

$$\nabla \times E = -\mu \frac{\partial H}{\partial t} \tag{3.4}$$

and

$$\nabla \times H = \sigma E + \varepsilon \frac{\partial E}{\partial t} \tag{3.5}$$

In some situations, there are independent current sources $\boldsymbol{J_o}$ not related to the magnetic fields (e.g from power sources). In such cases, Eqn. (3.5) can be written as;

$$\nabla \times H = J_0 + \sigma E + \varepsilon \frac{\partial E}{\partial t} \tag{3.6}$$

Taking curls of Eqns. (3.4) and (3.5) and then using the vector identity:

$$\nabla \times (\nabla \times A) = \nabla(\nabla . A) - \nabla^2 A$$

and noting that

$$\nabla . H = 0 = \nabla . E$$

we get;

$$\nabla^2 \mathrm{E} = \mu\sigma \frac{\partial E}{\partial t} + \mu\varepsilon \frac{\partial^2 E}{\partial t^2} \tag{3.7}$$

and

$$\nabla^2 \mathrm{H} = \mu\sigma \frac{\partial H}{\partial t} + \mu\varepsilon \frac{\partial^2 H}{\partial t^2} \tag{3.8}$$

In MT work, the fields E and H vary sinusoidally and hence solutions of Eqns. (3.7) and (3.8) can be expressed as:

$$\left.\begin{aligned} E(t) &= E_0 e^{j\omega t} \\ H(t) &= H_0 e^{j\omega t} \end{aligned}\right\} \tag{3.9}$$

Such that;

$$\frac{\partial E}{\partial t} = j\omega E \qquad \text{and} \qquad \frac{\partial H}{\partial t} = j\omega H \tag{3.10}$$

where $\omega = 2\pi f$ (angular frequency of the field)

Substituting Eqn. (3.10) into Eqns. (3.7) and (3.8), we get;

$$\nabla^2 \mathrm{E} = \mathrm{j}\omega\mu\sigma\mathrm{E} - \omega^2\mu\varepsilon E \tag{3.11}$$

$$\nabla^2 \mathrm{H} = \mathrm{j}\omega\mu\sigma\mathrm{H} - \omega^2\mu\varepsilon H \tag{3.12}$$

where the first and the second terms of the r.h.s of the equations relate to conduction and displacement currents respectively.

These are EM equations for propagation of electric and magnetic fields in isotropic homogeneous medium having conductivity σ, relative permeability μ, and relative permittivity ε.

Comparing Eqns. (3.11) and (3.12), the real part on the r.h.s corresponding to displacement current is negligible. As a result, in air and poorly conducting rocks;

$$\nabla^2 \mathrm{E} = 0, \qquad \nabla^2 \mathrm{H} = 0 \tag{3.13}$$

Within a good conductor, the imaginary part of the expression is significant;

$$\nabla^2 \mathrm{E} \cong \mathrm{j}\omega\mu\sigma\mathrm{E} \tag{3.14}$$

$$\nabla^2 \mathrm{H} \cong \mathrm{j}\omega\mu\sigma\mathrm{H} \tag{3.15}$$

Eqns. (3.14) and (3.15) are diffusion equations which reduce to the Laplace Eqn. (3.13) in air and rocks of low conductivity.

For a plane polarized wave; assuming the wave is propagating in z-axis such that the x-y plane is a plane of polarization, the solution becomes:

$$H = H_y(z,t) = H_0 e^{j\omega t + mz} \tag{3.16}$$

Thus,

$$H_y = H_0 e^{-\sigma z} \cos(\omega t - \sigma z) \tag{3.17}$$

The second part represents S.H.M with a phase shift, while the exponential is the attenuation of the wave with propagation distance.

3.1.3 Penetration depth of EM waves

A commonly used criterion for the penetration of EM waves in a uniform medium is the skin depth. The skin depth is defined as the distance for which the signal is reduce by e^{-1} or 37%.

From Eqn. (3.17);

$\delta(\omega) = \frac{1}{a}$, ($\delta$ is the skin depth)

$$\delta(\omega) = \sqrt{\frac{2}{\omega\mu\sigma}} \tag{3.18a}$$

The above expression shows that for higher frequencies and conductivities, there is a decrease in amplitude with depth. Letting $\mu = \mu_0 = 4\pi \times 10^{-7} Vs/Am$ (assuming $\mu = 1$, in the earth) and

$\omega = 2\pi f$, where f is the frequency of the field, we have:

$$\delta(\omega) = 500\sqrt{\frac{\rho}{f}}\ metres \tag{3.18b}$$

Or,

$$\delta(\omega) = 500\sqrt{\rho T}\ metres \tag{3.18c}$$

where ρ the resistivity of the medium and T denotes the period of the field.

From Eqn. (3.18) it can be seen that the depth of penetration of the EM wave in the subsurface increases according to the square root of the product of period and the medium's resistivity. In order to realize deeper penetration, data needs to be acquired for many hours so as to attain long periods. The skin depth explains the limitations of EM technique, particularly the decreasing resolution with increasing depth of penetration.

3.1.4 Horizontally Layered Earth

Consider a plane electromagnetic wave travelling into a flat earth consisting of a set of N horizontal layers, each with a uniform conductivity, σ_i and of thickness, d_i. The electromagnetic wave is excited in to the earth by a downward travelling plane electromagnetic wave as shown in Figure 3.1 below

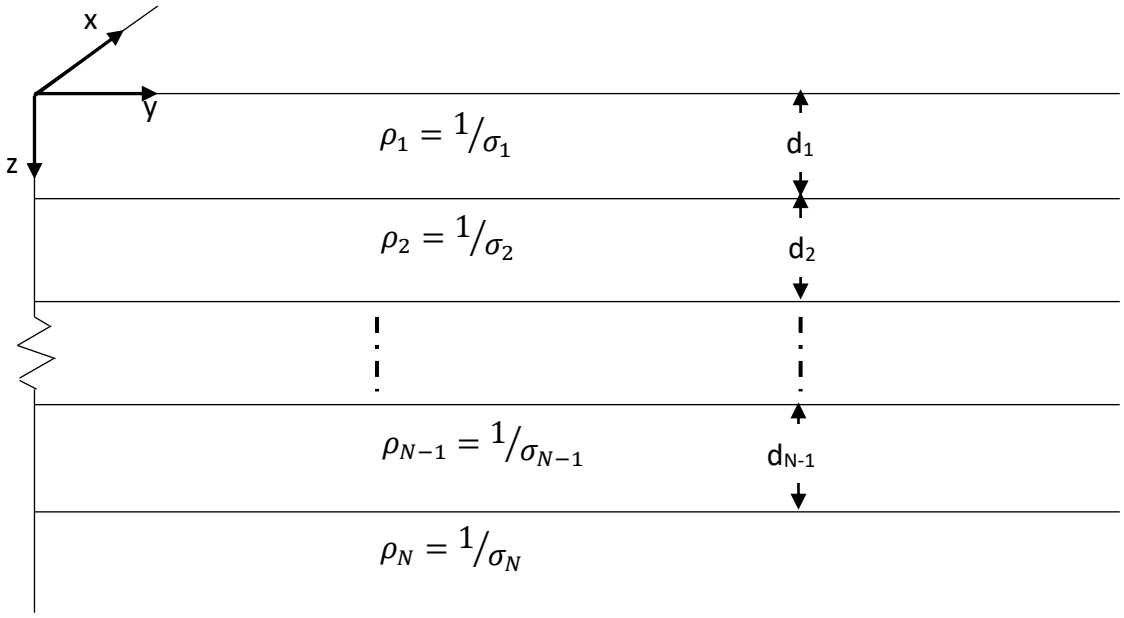

Figure 3.1: Layered earth penetration

At the boundary between the atmosphere and the solid earth, (z=0), we have:

$$\begin{pmatrix} E_x(\omega) \\ H_y(\omega) \end{pmatrix} = \begin{pmatrix} 0 & Z_{xy}(\omega) \\ Z_{yx}(\omega) & 0 \end{pmatrix} \begin{pmatrix} H_x(\omega) \\ H_y(\omega) \end{pmatrix} \tag{3.19}$$

where the impedance tensor elements are;

$$Z_{xy}(\omega) = -Z_{yx}(\omega) = \hat{Z}_1 \tag{3.20}$$

The parameter $\hat{Z}_1$is determined by a recursive relationship assuming the wave impedance is continuous across the surfaces between layers as follows:

$$\hat{Z}_i = Z_i \frac{\hat{Z}_{i+1} + Z_i \tanh(ik_i d_i)}{Z_1 + \hat{Z}_{i+1} \tanh(ik_i d_i)} \tag{3.21}$$

This recursive procedure can be used to expand the expression for wave impedance at the earth's surface (where we can measure it physically) through any number of layers, removing the arbitrary constants, one by one:

For $i = N - 1$,……, 1 and $\hat{Z}_N = Z_N$

$$Z_i = \frac{\mu_0 \omega}{k_i}; \qquad k_i = \sqrt{\mu_0 \varepsilon_0 \omega^2 - i\mu_0 \sigma_i \omega} \tag{3.22}$$

Therefore the tensor element can be written as

$$Z_i(\omega) = \left|\hat{Z}_i(\omega)\right| e^{i\phi(\omega)} \tag{3.23}$$

where $\hat{Z}_i$ and ϕ are dependent on the resistivity of the i[th] layer and angular frequency.

Similarly with homogeneous half-space, the phase and apparent resistivity can be expressed as:

$$\rho_a(\omega) = \frac{1}{\mu_0 \omega}\left|\hat{Z}_1\right|^2 = \frac{1}{\mu_0 \omega}\left|\frac{E_x}{H_y}\right|^2 = \frac{1}{\mu_0 \omega}\left|\frac{E_y}{H_x}\right|^2 \tag{3.24a}$$

$$\text{Phase, } \phi = \tan^{-1}\left(\frac{Im\hat{Z}_1}{Re\hat{Z}_1}\right) \tag{3.24b}$$

3.1.5 Magnetotelluric transfer functions

MT transfer functions contain information about the electrical conductivity in a hemisphere, with the Magnetotelluric site located at the centre of the bounding horizon. MT transfer functions are responses that relate measured EM field components at certain frequencies. These transfer functions are affected by electrical properties of the materials. MT transfer functions comprise of geomagnetic transfer functions and the Impedance tensors.

3.1.5.1 Impedance tensor transfer functions.

For real data, the impedance tensor can be described by the relationship between electric and magnetic fields at each frequency. The linear relations of the fields can be written as:

$$E_x(\omega) = Z_{xx}(\omega)H_x(\omega) + Z_{xy}(\omega)H_y(\omega) \tag{3.25}$$

$$E_y(\omega) = Z_{yx}(\omega)H_x(\omega) + Z_{yy}(\omega)H_y(\omega) \tag{3.26}$$

3.1.5.2 Geomagnetic transfer functions

This is a complex vector which provides connection between the magnetic field components in the vertical and horizontal directions. The lateral conductivity gradients within the earth produce the vertical components. The tipper ($\mathcal{T}$) describes this relationship.

$$H_z(\omega) = \mathcal{T}_{zx}H_x(\omega) + \mathcal{T}_{zy}H_y(\omega) \tag{3.27}$$

For 1-D Earth, H_z is zero and so $\mathcal{T}_{zx} = \mathcal{T}_{zy} = 0$.

In two-dimensional earth, the coordinate system is spun such that the x-axis is aligned in the direction of strike, commonly denoted by Tstrike, i.e $\mathcal{T}_{zx} = 0$, but $\mathcal{T}_{zy} \neq 0$. To achieve this, $|\mathcal{T}_{zx}|$ is minimized. It is possible to separate the tipper vector (induction arrows) to obtain a couple of real distinct vectors in the horizontal xy plane. The real induction arrows can be explained using two convections namely: reversed (Parkinson convention, Parkinson, 1959) and non-reversed (Wiese convention). According to Wiese convention, the vectors point away from lateral increase in electrical conductivity

(Wiese, 1962). The arrows have an imaginary (out-of-phase) and real (in-phase) part. The length of tipper vector depends on both the conductivity contrast and the closeness to the conductor such that, for a closer conductor, the induction arrow is long and vice-versa. Similarly, the induction arrows are longer where there is a big contrast and vice-versa.

The length of the imaginary (M_q) and real (M_r) arrows are given by:

$$M_q = \left(\Im\mathcal{T}_{zx}{}^2 + \Im\mathcal{T}_{zy}{}^2\right)^{1/2} \tag{3.28}$$

$$M_r = \left(\Re\mathcal{T}_{zx}{}^2 + \Re\mathcal{T}_{zy}{}^2\right)^{1/2} \tag{3.29}$$

where $\Im$ and $\Re$ are the imaginary and real part of tipper, respectively. In order to determine the directions of the arrows, the following equations are used:

$$\theta_q = \tan^{-1}\left(\frac{\Im\mathcal{T}_{zy}}{\Im\mathcal{T}_{zx}}\right) \tag{3.30}$$

$$\theta_r = \tan^{-1}\left(\frac{\Re\mathcal{T}_{zy}}{\Re\mathcal{T}_{zx}}\right) \tag{3.31}$$

θ_q and θ_r are dextrorotatory from the geomagnetic north.

In two-dimensional earth, both the tipper vector and the regional strike are orthogonal to each other. For the 3-D case however, the tipper direction varies and is usually in the opposite direction to the conductive body.

3.1.5.3 1-D impedance tensor

For a 1-D layered earth, the conductivity ρ varies only with depth and the MT transfer functions are independent of the orientation of the measured axes and are functions only of the frequency. Thus, the impedance tensor can be expressed as:

$$Z_{1D} = \begin{pmatrix} 0 & Z_{xy} \\ -Z_{yx} & 0 \end{pmatrix} \tag{3.32}$$

The elements in the diagonal of the impedance tensor, Z_{yy} and Z_{xx} are both null, whereas the off-diagonal components, which couple orthogonal magnetic and electric field components have opposite signs, but equal in magnitude.

The apparent resistivity for the 1-D earth can be defined as:

$$\rho_a = \frac{1}{\mu_o \omega} |Z|^2 \tag{3.33}$$

and the phase of the complex impedance can be defined as:

$$\phi_a = tan^{-1}\left(\frac{Im\ Z}{Re\ Z}\right) \tag{3.34}$$

3.1.5.4 2-D impedance tensor

For 2-D earth the subsurface resistivity varies with depth and one horizontal direction while remaining unchanged in the other horizontal direction. Geoelectric strike is the direction along which conductivity, or resistivity for this matter, remains constant.

Ordinarily the MT field layout is rarely in the strike direction, so that in order to perform 2-D analysis the data has to be rotated to the respective polarization direction (see section 3.1.6). The mode with electric field parallel to strike is called Transverse Electric (TE) mode or E-polarization and that with magnetic field parallel to strike is called Transverse Magnetic (TM) mode or B-polarization. For a perfectly 2-D earth the diagonal elements of the impedance tensor are zero. However, this condition is rarely satisfied in field data because of distortion.

$$Z_{2D} = \begin{bmatrix} 0 & Z_{xy} \\ Z_{yx} & 0 \end{bmatrix} \tag{3.35a}$$

where: $$Z_{xy}(\omega) = Z_{TE} = \frac{E_x(\omega)}{H_y(\omega)} \tag{3.35b}$$

$$Z_{yx}(\omega) = Z_{TM} = \frac{E_y(\omega)}{H_x(\omega)} \tag{3.35c}$$

The above yields the following two sets of apparent resistivities and impedance phases;

TE-mode: $\rho_{xy} = \frac{1}{\mu_o \omega}\left|Z_{xy}\right|^2;\ \phi_{xy}$ and TM-mode: $\rho_{yx} = \frac{1}{\mu_o \omega}\left|Z_{yx}\right|^2; \phi_{yx}$ (3.36)

As shown in Figure 3.2 below, the TE-mode describes currents flowing parallel to the strike direction which induces magnetic fields perpendicular to it and can be described in terms of electromagnetic field components E_x, H_y and H_z. Similarly, the TM-mode describes currents flowing perpendicular to strike which induces magnetic fields parallel to it, and can be described in terms of the electromagnetic field components H_x, E_y and E_z.

The electric field E_y in the TM-mode is discontinuous across a vertical contact, therefore Z_{xy} is also discontinuous. This means that ρ_{TM} will also be discontinuous. Consequently, lateral conductivity variations are better resolved by the B-polarization

than E-polarization. The E-polarization apparent resistivities vary smoothly across vertical contacts and usually have an associated vertical magnetic field because its associated magnetic field component is perpendicular to strike.

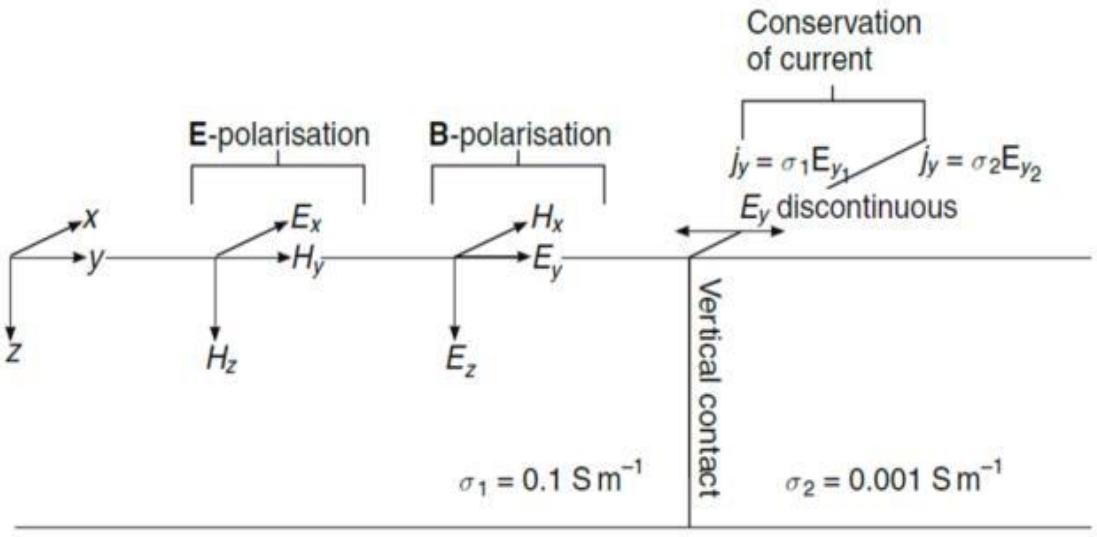

Figure 3.2: Simple 2-D model illustrating polarization and vertical contact between two zones of different conductivity (adopted from Simpson and Bahr, 2005)

3.1.5.5 3-D impedance tensor

The real earth is 3-dimensional where conductivity varies in all directions, σ(x,y,z). The impedance tensor takes the general form:

$$Z_{3D} = \begin{pmatrix} Z_{xx} & Z_{xy} \\ Z_{yx} & Z_{yy} \end{pmatrix} \tag{3.37}$$

All the components of the impedance tensor are non-zero and the diagonal elements of the impedances tensor do not vanish in any coordinate system, therefore all the tensor

elements are considered in the interpretation. Different forms of apparent resistivity can be derived from the full impedance tensor. The most common of these are:

The rotational dependent apparent resistivities (Z_{xy} and Z_{yx}), given as:

$$\rho_{xy} = \frac{1}{\mu_o \omega}\left|Z_{xy}\right|^2 \quad \text{and} \quad \rho_{xy} = \frac{1}{\mu_o \omega}\left|\frac{1}{Z_{yx}}\right|^2 \quad \text{Phase, } \phi = tan^{-1}\left(\frac{Im\, Z}{Re\, Z}\right) \tag{3.38}$$

and rotationally independent determinant, $Z_{det} = \sqrt{Z_{yy}Z_{xx} - Z_{xy}Z_{yx}}$ given as:

$$\rho_{det} = \frac{1}{\mu_o \omega}|Z_{det}|^2; \;\; \phi_{det} = \arg(Z_{det}) \tag{3.39}$$

Arithmetic mean, $Z_{ave} = \frac{Z_{xy} - Z_{yx}}{2}$ given as:

$$\rho_{ave} = \frac{1}{\mu_o \omega}|Z_{ave}|^2; \;\; \phi_{ave} = \arg(Z_{ave}) \tag{3.40}$$

3.1.6 Rotation of the impedance tensor

MT data can be collected within any arbitrary coordinate system. In data analysis we look for directional information in the data, in differently oriented coordinate system. The matrix form of the full impedance tensor is:

$$\begin{pmatrix} E_x \\ E_y \end{pmatrix} = \begin{pmatrix} Z_{xx} & Z_{xy} \\ Z_{yx} & Z_{yy} \end{pmatrix} \begin{pmatrix} H_x \\ H_y \end{pmatrix} \tag{3.41}$$

If the coordinate system is rotated through an angle θ, such that the coordinates change form x,y, to x', y' as shown in Figure 3.3 to give;

The field transforms as: $\overrightarrow{E'} = \bar{\bar{R}} \cdot \vec{E}$; $\overrightarrow{H'} = \bar{\bar{R}} \cdot \vec{H}$ (3.42)

and the tensor transforms: $E' = Z' \cdot H' = RZR^T H'$ (3.43a)

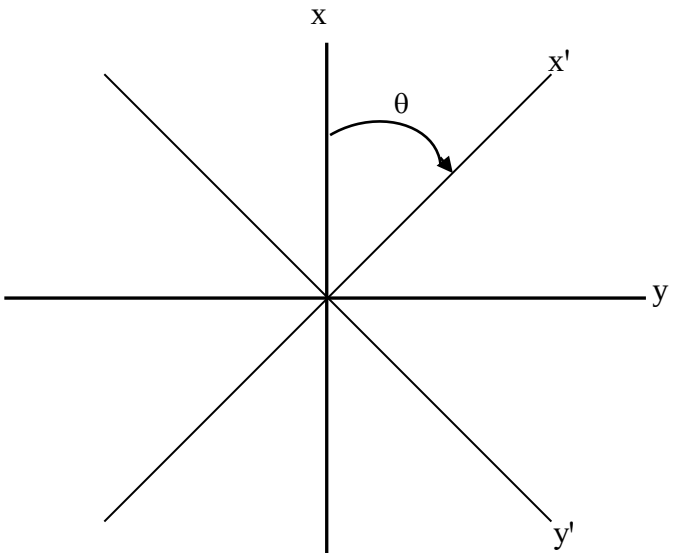

Figure 3.3: Rotation of reference frame

Therefore, $Z' = R(\theta)Z \cdot R(\theta)^T = RZR^T$ (3.43b)

where, the rotation operator is $R(\theta) = \begin{bmatrix} \cos\theta & \sin\theta \\ -\sin\theta & \cos\theta \end{bmatrix}$; and the transpose of R is R^T.

In full form this becomes;

$$Z'_{xx} = Z_{xx}cos^2\theta + \left(Z_{xy} + Z_{yx}\right)\sin\theta\cos\theta + Z_{yy}sin^2\theta \quad (3.44a)$$

$$Z'_{xy} = Z_{xy}cos^2\theta + \left(Z_{yy} - Z_{xx}\right)\sin\theta\cos\theta + Z_{yx}sin^2\theta \quad (3.44b)$$

$$Z'_{yx} = Z_{yx}cos^2\theta + \left(Z_{yy} + Z_{xx}\right)\sin\theta\cos\theta + Z_{xy}sin^2\theta \quad (3.44c)$$

$$Z'_{yy} = Z_{xx}cos^2\theta + \left(Z_{xy} + Z_{yx}\right)\sin\theta\cos\theta + Z_{xx}sin^2\theta \quad (3.44d)$$

To obtain the principal directions of the structure if the earth is two-dimensional involves minimizing $\left(|Z'_{xx}|^2 + |Z'_{yy}|^2\right)$ or maximizing$\left(|Z'_{xy}|^2 + |Z'_{yx}|^2\right)$, both of which give the same principal direction.

3.1.7 MT strike analysis

MT impedance tensor, Z contains information about dimensionality and directions. Strike analysis attempts to recover the dimensionality from the MT data such as determination of strike of dominant 2-D Geoelectrical structure. This can be difficult where there is both local distortion and noise. According to Jones and Groom (1993), the most unstable feature which can be determined from MT data is the strike angle. In MT studies, especially in 2-D interpretation, it is very important to carefully choose the interpretation coordinate frame for a particular strike angle. Although information from other sources, such as geological strike can be used, it should be demonstrated that the coordinate frame chosen is supported by the Zstrike of the MT data. Induction vectors are used as a means to describe the geoelectric strike of a region. The real component of the induction vector is usually directed perpendicular to the local geoelectric strike and points in the opposite direction to the more conductive regions (Wiese convention).

For 2-D structure, impedance tensor is given by:

$$Z_{2D} = \begin{pmatrix} 0 & Z_{TE} \\ Z_{TM} & 0 \end{pmatrix} \tag{3.45}$$

The impedances Z_{TM} and Z_{TE} compare fields perpendicular and parallel to the Geoelectrical strike respectively. The strike angle θ_0 is calculated from measured

impedances through maximization of appropriate functions of off-diagonal impedance, Z_{yx} and Z_{xy} under rotation of the axis.

$$\theta_0 = \frac{1}{4}\tan^{-1}\frac{(Z_{xx}-Z_{yy})(Z_{xy}+Z_{yx})^{*}+(Z_{xx}-Z_{yy})^{*}(Z_{xy}+Z_{yx})}{|Z_{xx}-Z_{yy}|^{2}-|Z_{xy}-Z_{yx}|^{2}} \quad (3.46)$$

here, $*$ refers the complex conjugate.

From Eqn. (3.46) we get the four angles that give the maximum values of the off-diagonal components that constitute two principal directions normal to one another.

The calculated direction of strike has a 90^0 imprecision. Tipper strike can be used to resolve the $\pm 90^0$ ambiguity. It absolutely describes the strike of the region using an assumption that the structures of the region are 2-D (Zhang *et al.*, 1987).

3.2 Transient Electromagnetic (TEM) method

3.2.1 Basic theory

In the central loop TEM method, an artificially controlled source is used to create a time-varying magnetic field in the subsurface. The method involves placing a wire loop on the ground and then passing through it a constant current. This current is switched on and off at known intervals of time. At switch off times, it causes sudden change in the magnetic field which then causes current to flow in the earth.

This current creates an image of the loops for a very short time. Since there is no source to support the induced current, it dies out generating a new secondary magnetic field that varies with time and which consequently induces a new current in the ground. This

current density migrates outwards and downwards into the earth. The receiver coil placed at the centre of the loop measures the rate of decay of induced magnetic fields.

The decay rate of the secondary magnetic field and the distribution of current are affected by the electrical resistivity of the rocks, in which case, the fields decay much quickly on conductive rocks as compared to resistive rocks (Árnason, 1989). TEM configuration and the transient responses are illustrated in figures 3.4 and 3.5 below.

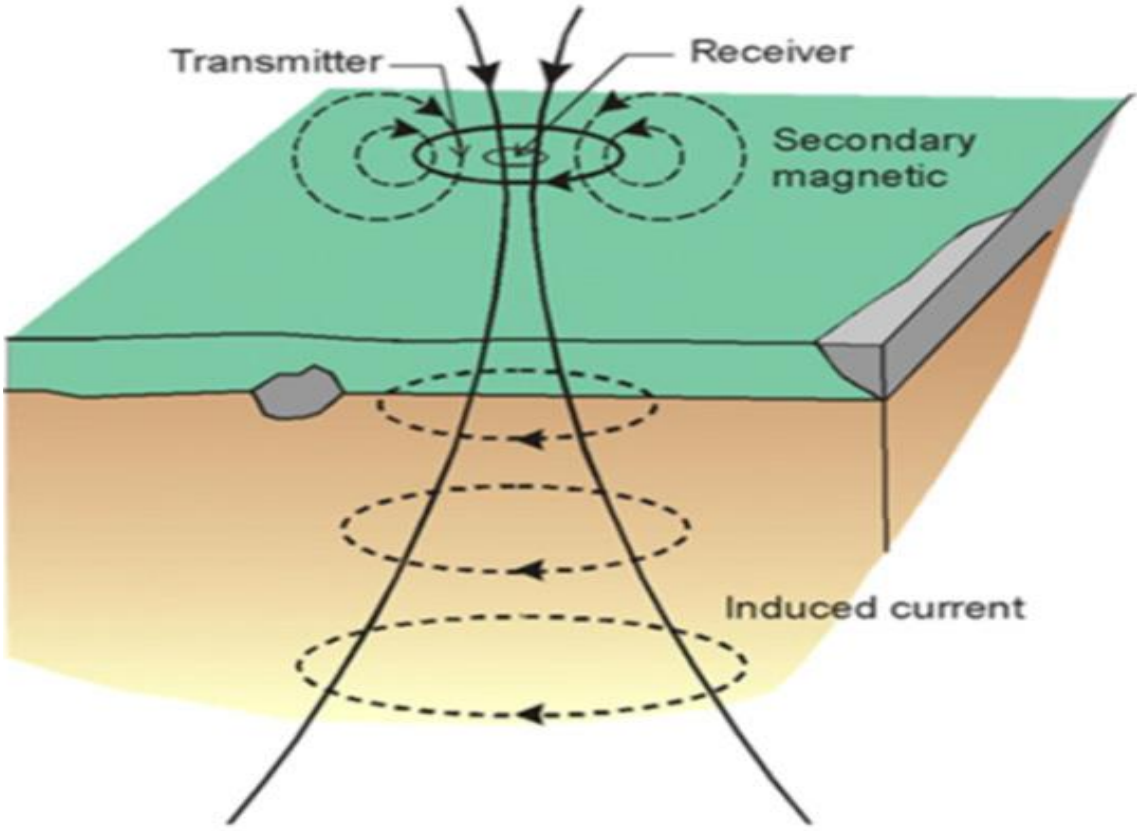

Figure 3.4: The central loop Transient Electromagnetics configuration (Hersir and Björnsson, 1991)

Figure 3.5 shows the basic principles of the TEM method; (a) shows the current in the transmitter loop. (b) is the induced electromotive force in the ground, and (c) is the secondary magnetic field measured in the receiver coil (Christensen *et al*., 2006)

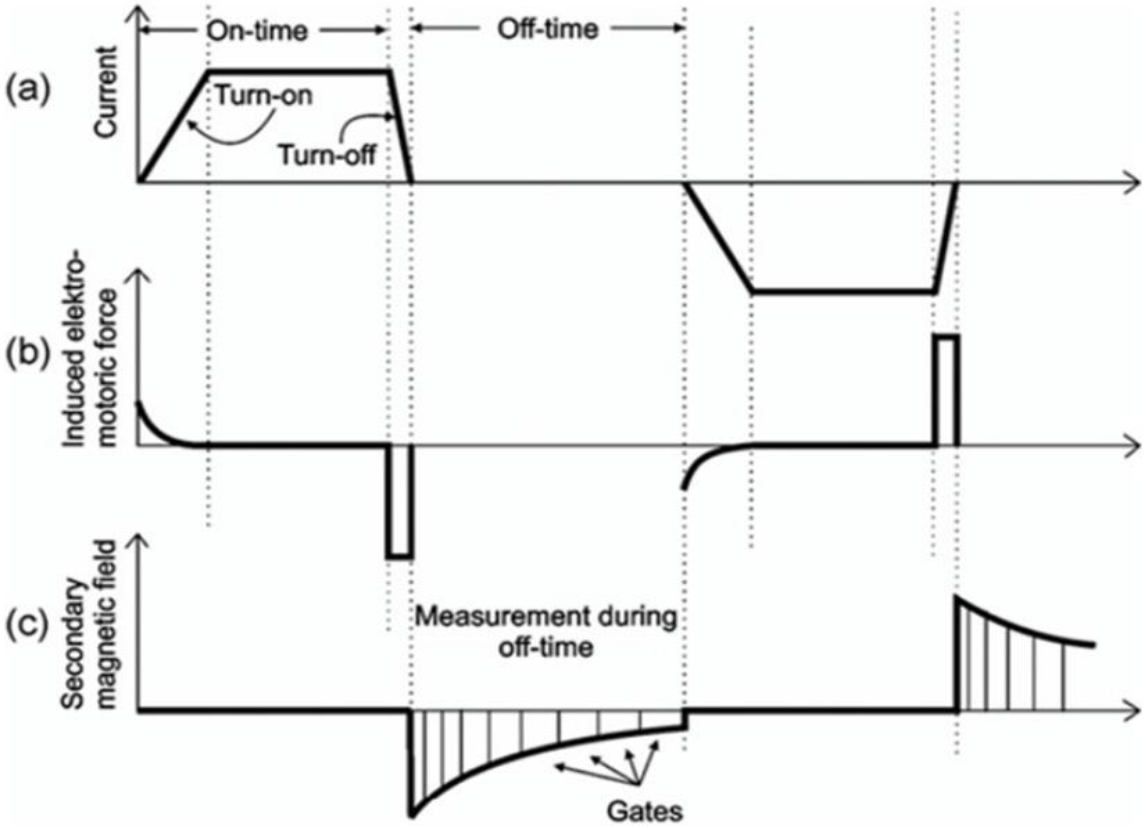

Figure 3.5: Basic principles of the Transient Electromagnetics method (Muturia, 2013)

3.2.2 Layered Earth

The voltage induced in a receiver coil placed at the centre of a circular source loop of radius r and with the harmonic current, $I = I_o e^{i\omega t}$ on the surface of an N-layered half-space is given as (Árnason, 1989):

$$V(\omega, r) = A_r n_r A_s n_s I_o e^{i\omega t} \frac{-i\omega\mu}{\pi r} \int_0^\infty \frac{\lambda^2}{m_o} \frac{S_o}{S_o - T_o} J_1(\lambda r) d\lambda \quad (3.47)$$

where, n_r = Number of turns on the receiver coil

A_r = Cross-sectional area of the receiver coil, (m^2)

n_s = Number of turns in transmitter loop

A_s = Area of the transmitting loop, (m^2)

r = Radius of the transmitter loop, (m)

$V(t,r)$ = Transient voltage, (V)

t = Time elapsed after the current in the transmitter is turned off, (s)

I_0 = Current in the transmitting loop, (A)

S_o and T_o, which depend on thickness and layer resistivity, can be expressed in recursion relationships:

$$S_{i-1} = \cosh(m_i d_i) - T_i \sinh(m_i d_i) \tag{3.48a}$$

$$T_{i-1} = -\frac{m_i}{m_{i-1}}[S_i \sinh(m_i d_i)] - T_i \cosh(m_i d_i) \tag{3.48b}$$

where d_i = Thickness of the i^{th} layer (m); and

m_i = Impedance of the i^{th} layer.

The quantities S_o and T_o, which determine the voltage in Equation (3.47) depend on angular frequency, ω and the conductivities, σ_i through $m = \sqrt{\lambda^2 - {k_i}^2}$.

The ratio between the measured voltage and the transmitted current defines the mutual impedance between the source and the receiver. Using Eqn (3.47) mutual impedance can be expressed as:

$$Z(\omega,r) = \frac{V(\omega,r)}{I_0 e^{i\omega t}} = A_r n_r A_s n_s \frac{-i\omega\mu}{\pi r} \int_0^\infty \frac{\lambda^2}{m_o} \frac{S_o}{S_o - T_o} J_1(\lambda r) d\lambda \quad (3.49)$$

Using Fourier expansion of the function describing the transmitted current, Eqn (3.49) can be transformed to time domain (Árnason, 1989). Suppose the transmitted current is denoted by *I(t)*, then the Fourier expansion of the current function will be:

$$I(t) = \frac{1}{(2\pi)^{\frac{1}{2}}} \int_{-\infty}^{\infty} I(\omega) e^{i\omega t}\, d\omega \quad (3.50)$$

where $$I(\omega) = \frac{1}{(2\pi)^{\frac{1}{2}}} \int_{-\infty}^{\infty} I(t) e^{i\omega t}\, dt \quad (3.50a)$$

From Equation (3.50), the voltage induced in the receiver coil in terms of the Fourier transform of the transmitted current and mutual impedance (as a function of frequency are expressed as:

$$V(t,r) = \frac{1}{(2\pi)^{\frac{1}{2}}} \int_{-\infty}^{\infty} Z(\omega,r) I(\omega) e^{i\omega t}\, d\omega \quad (3.51)$$

The measured voltage as a function of time after the steady current is abruptly turned off at t=0, is given by:

$$V(t) = \frac{-I_0}{2\pi} \int_{-\infty}^{\infty} \frac{Z(\omega)}{i\omega} e^{i\omega t}\, d\omega = \frac{I_0}{2\pi} \int_{-\infty}^{\infty} \Phi(\omega) e^{i\omega t}\, d\omega \quad (3.52)$$

where for convenience $\Phi(\omega)$ is defined as:

$$\Phi(\omega) = \frac{Z(\omega)}{-i\omega} \quad (3.53a)$$

$\Phi(\omega)$ depends ω on through ω^2 and $i\omega$, hence:

$$\Phi^*(-\omega) = \Phi(\omega) \quad (3.53b)$$

where * denotes the complex conjugation.

Hence:

$$\mathrm{Re}\Phi(-\omega) = \mathrm{Re}\Phi(\omega)\,; \qquad \mathrm{Im}\,\Phi(-\omega) = \mathrm{Im}\,\Phi(\omega) \tag{3.53c}$$

This can be used to simplify Equation (3.52) because if it is written in terms of imaginary and real parts, it becomes:

$$V_{-}(t) = \frac{-2I_0}{\pi}\int_0^{\infty} \mathrm{Re}\Phi(\omega)\cos(\omega t)d\omega \;\text{ or }\; V_{-}(t) = \frac{-2I_0}{\pi}\int_0^{\infty} \mathrm{Im}\,\Phi(\omega)\sin(\omega t)d\omega. \tag{3.54}$$

Árnason, (1989) in (Eqn. 3.55) gives the transient voltage generated in the receiver coil due to linearly ramped step function. In practical application, the current is turned off linearly in a time interval of length T_{OFF} (as shown on Figure 3.5a), but not turned off abruptly.

$$V(t) = \frac{I_0}{T_{OFF}}\int_{-T_{OFF}}^{0} V_{-}(t-\tau)d\tau = \frac{I_0}{T_{OFF}}\int_{t}^{t+T_{OFF}} V_{-}(-\tau)d\tau \tag{3.55}$$

At the so called late times, the induced voltage in the receiving coil on a homogenous half-space of conductivity, σ is given by (Árnason, 1989):

$$V(t,r) \approx I_0 \frac{C(\mu_0\sigma r^2)^{3/2}}{10\pi^{1/2}t^{5/2}} \tag{3.56}$$

where, $\quad C = A_r n_r A_s n_s \frac{\mu_0}{2\pi r^3}$

It follows thus from Eqn. 3.56 that when the transmitter current is abruptly switched off, the transient voltage for the late times is proportional to $\sigma^{3/2}$ and decreases with time as $t^{-5/2}$. From Eqn. (3.56) the late time apparent resistivity ρ_a, can now be obtained as:

$$\rho_a = \frac{\mu_0}{4\pi}\left[\frac{2I_0\mu_0 A_r n_r A_s n_s}{5t^{5/2}V(t,r)}\right]^{2/3} \tag{3.57}$$

3.2.3 Homogenous earth

Voltage response of homogenous half spaces with different resistivities has the same general character and can be divided into three stages as shown in Figure 3.6 below.

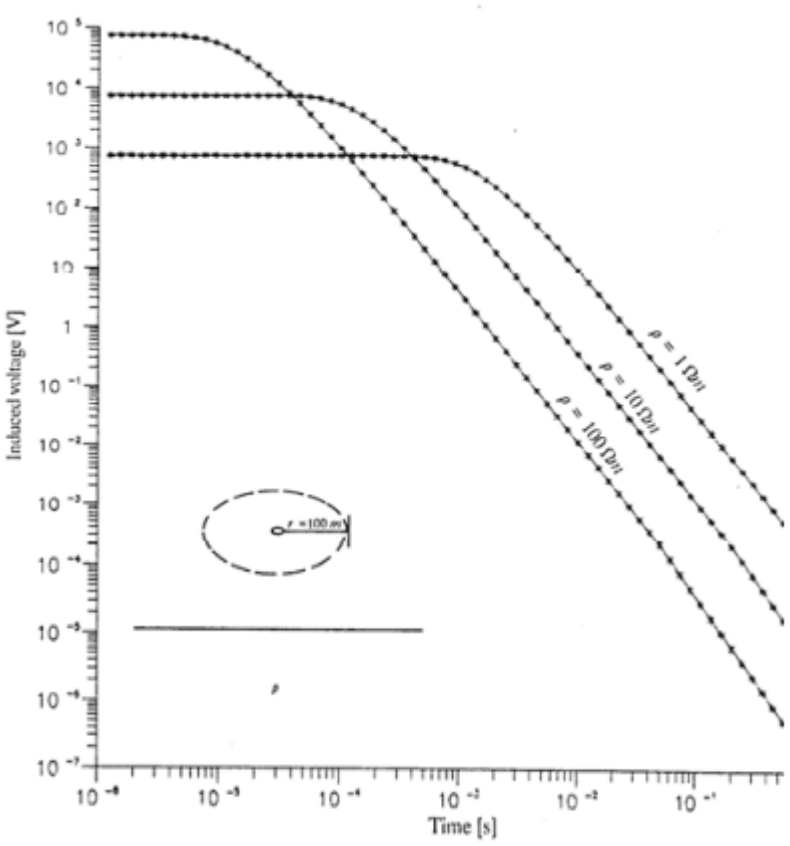

Figure 3.6: Voltage response for homogenous half space (modified from Árnason, 1989)

In the intermediate stage, the induced voltage begins to decay with time and with constantly growing gradient on the log-log scale until it attains the late stage. The

response voltage then decreases with time such that the logarithm of the induced voltage decreases linearly as a function of the logarithm of time. In the late stage, the slope of the response is easily seen to be $\frac{-5}{2}$ an indication that the induced voltage varies as $t^{\frac{-5}{2}}$ (Equation 3.57). From Figure 3.6, we can also observe that the early stage voltage response grows with increasing resistivity of the half space medium. Also, the transitions from early to intermediate and from intermediate to late stages get shifted towards earlier times but in such a way that the shape of the response curve remains unchanged.

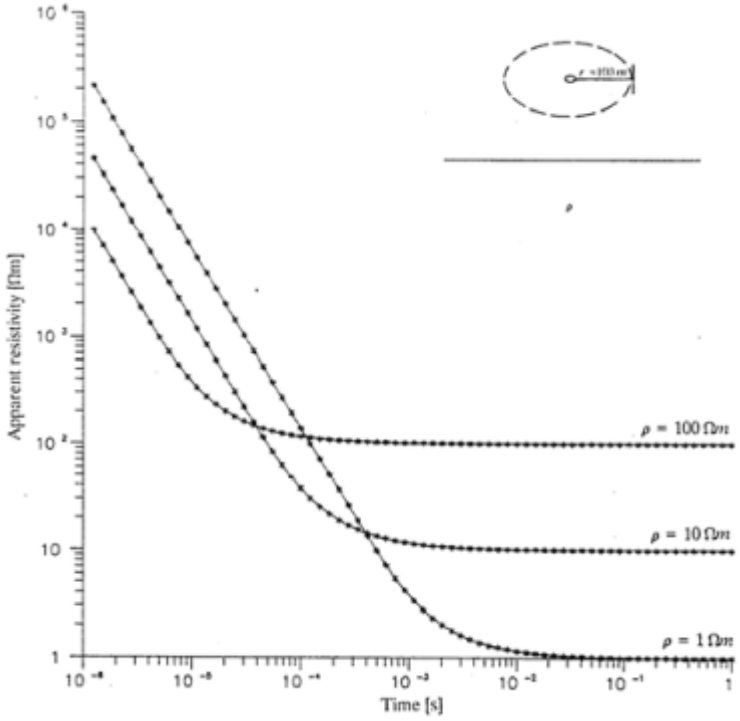

Figure 3.7: Late time apparent resistivity for homogenous half space (mod. from Árnason, 1989)

For a homogenous earth of resistivity ρ, the apparent resistivity (Equation 3.57) at late times gives the true resistivity. This can be seen from Figure 3.7 where the transient response for uniform half-space with resistivities, ρ = 1, 10 and 100 Ωm and for r = 100 m are shown as an apparent resistivity vs. time according to Equation 3.57 (Árnason, 1989). From Figure 3.7 it can also be seen that the apparent resistivity approaches the true resistivity of the half-space at later times as the resistivity gets lower.

3.3 Anomalous distortions in the Earth

There are two types of electromagnetic distortions; the galvanic distortion which is generated by excess charges and the induction distortion which reflects the inductive interaction between the excess currents. Galvanic distortions occur when currents causing a distortion flow across boundaries in electrical conductivity. Induction effects occur when the currents causing a distortion flow entirely within a bounded region (eddy currents) (Muturia, 2013). The major difference between the two is that galvanic distortions occur due to secondary electric field arising from electric charge build-up on boundaries of different conductivities and they persist over the whole frequency range and do not vanish with lowering frequency, whereas the induction distortions result from induced currents within anomalous conductivity bodies which appear at high frequencies and vanish at low frequencies. A weakness in MT sounding is that inhomogeneities in the uppermost layers may severely distort the electric field and consequently the impedance tensor along with the apparent resistivities. The dominant distortions are of galvanic nature and they extend over the whole range of frequencies, causing static shifts of the apparent resistivity curves. The near-surface inhomogeneities

affect the apparent resistivities no matter how low the frequency is. The galvanic distortions are very serious because they persist at low frequencies when the penetration depth of the normal field far exceeds the dimensions and depth of the inhomogeneities. Near-surface distortions also result from the effects caused by variations in conductance of sediments underlain with resistive basements or by structures in the basement topography.

3.3.1 The Magnetotelluric static shift problem

Static shift in MT is a phenomenon that arises due to local surface or near-surface conductivity contrasts which change the electric field in direction and magnitude. This phenomenon occurs when the dimensions of the anomalous body are much less than the skin depth. Static shift is a common problem to all resistivity methods that measure electric field at the ground surface. It is occasioned by the accumulation of charges at the resistivity boundaries causing the electric field to be discontinuous close to the boundary. Static shifts result from two main phenomenon i.e; voltage distortion and current distortion (Árnason, *et al.*, 2010). The static shift is expressed by scaling of the apparent resistivity by an unknown factor (shifted on log scale), so that apparent resistivity curves plot parallel to their true level. This shift is independent of frequency (Jones, 1988) and does not affect the phase curve.

The static shift factor cannot be determined directly from MT data recorded at a single station. A parallel shift between two polarizations of the apparent resistivity curves is a clear indicator that static shift is present in the data. The correct level of the apparent resistivity curves may lie above, below or between the measured responses. The parallel

shifts in apparent resistivity curve can bring about huge inconsistencies in the inverted data. For example, a shift down by S=0.1 will in interpretation, result in ten times too low resistivity values and about three times too small depths to resistivity boundaries (Árnason, 2008). 2-D and 3-D models may contain extraneous structure if static shifts are not corrected for data collected in environments with extreme near surface resistivity variations such as in volcanoes. A static shift multiplier below 1 results in decreased depth to boundaries and lower resistivities whereas a multiplier above 1 results in increased depth to boundaries and higher resistivities. Therefore, taking measurements directly over surficial resistive bodies, MT curves are shifted upwards, and shifted downwards when measuring over conductive bodies.

A number of methods have been proposed as possible solutions for the static shift problem in MT measurements. It has been claimed that the static shift problem can be dealt with by resolving the shallow resistivity structure around the dipole by measuring at high enough frequencies. This would be true if the earth was a pure Ohmic conductor, but in reality, both capacitive and inductive effects are at play. Ogawa and Ushida (1996) as well as DeGroot-Hedlin (1991) suggested that static shift correction could be done on MT data by use of an inversion algorithm. The main assumption in this case is that the shift multipliers for many functions are close to one. This assumes that for many soundings, the shift multipliers are close to unity. The assumption may not be absolutely true as will be seen later in the analysis of shift parameters in the Arus field. Another way and the one that has been used in this work, is the use of the TEM method for static shift correction by conducting a joint inversion of both TEM and MT (Pellerin and Hohmann, 1990). The principle behind this is based on the fact that for TEM

measurements at late time, the near surface inhomogeneities do not cause any distortions since TEM does not measure electrical field. Model calculations have been used to test this fact (e.g Sternberg *et al*., 1988, Árnason, 2008) and proven to be a reliable technique to correct for static shifts in MT soundings. It must therefore be born in mind that authenticity of the static shift correction greatly determines the success of MT data interpretation.

3.4 Application of resistivity methods in geothermal exploration

Resistivity surveys have become the most preferable methods in exploration for geothermal resources over the years. These methods relate directly to the properties that characterize geothermal systems such as salinity, porosity, degree of hydrothermal alteration of the rocks, permeability and temperature (Hersir and Björnsson, 1991). The measurements of the Geoelectrical fields provide information on the subsurface resistivity structure distribution owing to zones of hydrothermal alteration (Árnason *et al.*, 2000). The flow of high temperature geothermal fluids within the geothermal system results in a sequence of hydrothermal minerals. By use of resistivity methods, the conductivity patterns of the subsurface rocks can be determined both laterally and with depth. These methods include the controlled-source induction (active) methods (e.g TEM) as well as the natural-source (passive) methods (e.g MT). Electromagnetic techniques are more sensitive to low resistivity structures compared to direct current (DC) techniques.

3.4.1 Resistivity of Rocks

Most rocks are formed from electrical insulating minerals. Electrical resistivity of rocks within the subsurface is generally dependent on the presence of conductive minerals within the rock matrix as well as the flow of electrically charged particles suspended in the fluids found within the pores of the rocks. Despite the fact that water is poor conductor of electrical energy, groundwater usually contains dissolved salts and minerals which greatly boost its electrical conductivity. Thus, fluid saturation and connected porosity more often than not dominate electrical resistivity together with mineral alteration. Low resistivity is not only contributed to by pores but also fractures filled with conducting fluids within crystalline rock. Electrical resistivity ρ of a material is the product of the electrical resistance R of the material and its cross-sectional area A per unit length L. Thus:

$$\rho = \frac{RA}{L} \tag{3.58}$$

where R = Resistance (Ω)

A = Area (m^2)

L = Length (m)

ρ = Specific resistivity (Ωm)

Electrical resistivity of rocks depends on the porosity, degree of saturation and the electrical conductivity of the fluid present within the pores of the rocks (Palacky, 1987). If the rock is fractured, then its permeability and porosity are governed by those of the fractures. Generally, porosity of rocks decreases with depth hence reducing the effects of pore fluid conditions. The mineral composition of the rocks, in particular the type

and amount of clays present, has the biggest contribution to the bulk resistivity of the rock mass. The relation between the water in the pores of sediment or rock and its resistivity can be expressed with Archie's Law (1942)

$$\rho_0 = a\rho_f \varphi^{-m} \tag{3.59}$$

where ρ_0 = Bulk resistivity (Ωm);

ρ_f = Resistivity of the pore fluid (Ωm);

φ = Porosity expressed as a fraction per unit volume of rock;

m = Cementing factor, usually lies between 1.5 and 2.0.

a depends on the pore geometry.

CHAPTER FOUR

MATERIALS AND METHODS

4.1 Introduction

The survey covered an area of about 160 Km^2 and consisted of 5 profiles spaced 2 Km apart. A total of 48 MT soundings and 50 TEM soundings were conducted with a spacing of 2 Km apart. Each profile line thus had 10 soundings of both MT and TEM carried along it, with the TEM soundings conducted at the same points with the MT soundings. In this study, the data was acquired using two different instruments, for MT and TEM. The MT and TEM stations in the study area are shown on Figure 4.1.

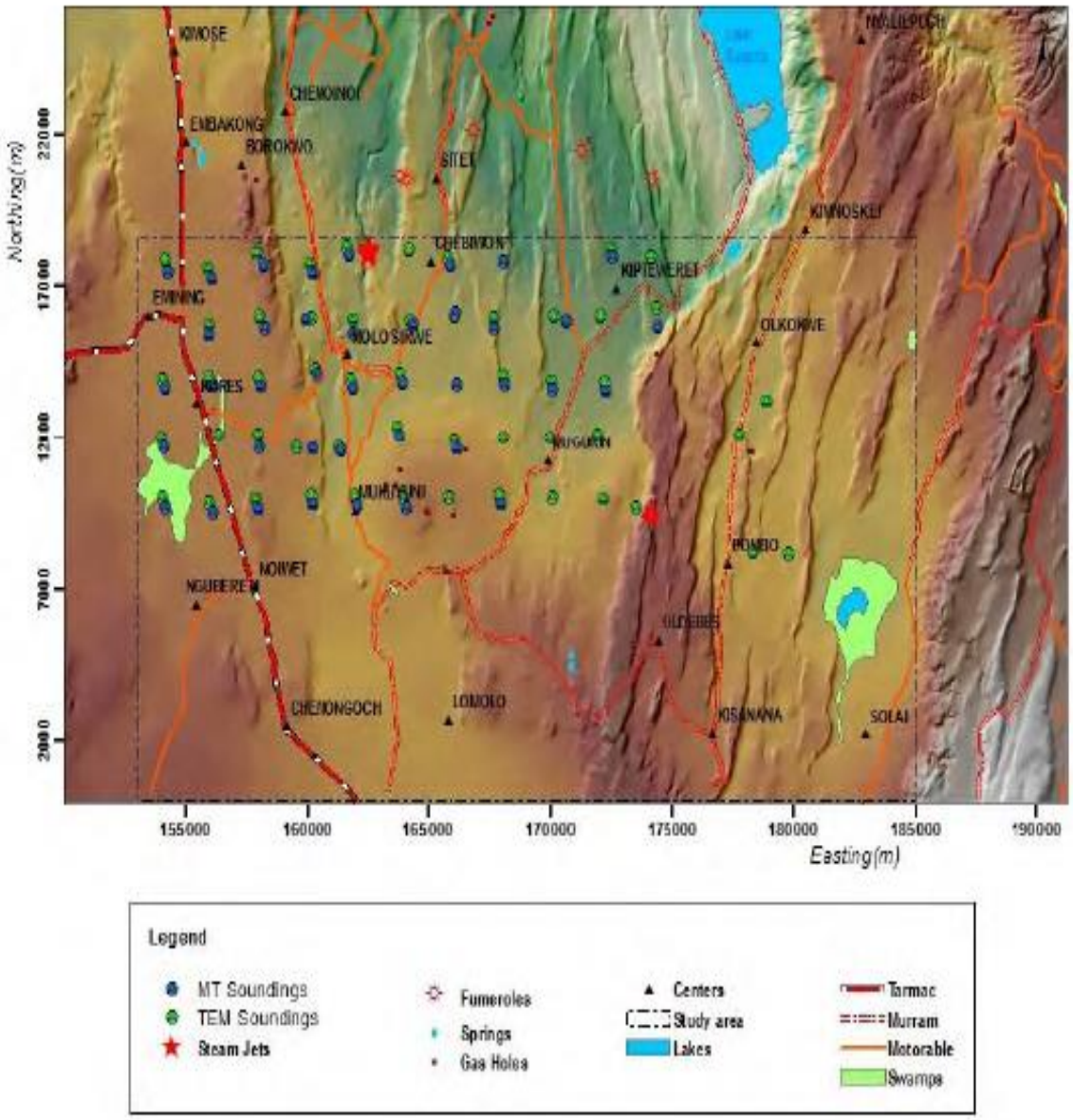

Figure 4.1: Location of the Magnetotelluric and Transient Electromagnetics soundings

4.2 Magnetotelluric (MT) Method

In the magnetotelluric technique (MT) the fluctuations of the earth's natural electrical and magnetic currents are measured. Lower frequency waves penetrate deeper while the

higher frequency ones map the shallow subsurface. The data was acquired using five sets of 5-channel MT data acquisition systems, commonly referred to as MTU-5A from Phoenix Geophysics, Canada. The instrumentation comprises of:

- MT unit (MTU-5A) data recorder
- Flash memory for data recording
- Non-polarizing electrodes
- Global Positioning System (GPS)
- Magnetic compass
- Induction coils
- Telluric and magnetic cables
- 12 V battery

The layout is made such that the electric dipoles are aligned in magnetic North-South (E_x) and East-West (E_y) directions respectively, with corresponding magnetic channels (H_x and H_y) in orthogonal directions. The third channel (H_z) is positioned vertically in the ground, as demonstrated in Figure 4.2 below.

To ensure good conductivity, the ports were soaked with clean water that had been salted with common salt (sodium chloride solution). A 12V battery was used to power the system. Prior to data collection using the MTU-5A recorder, a start up file containing input variables such as time for data collection, gains, filters and the equipment and coils calibrations is prepared and saved on a memory card which is then stashed in a port in the MTU-5A data recorder. While placing the electric dipoles at

their appropriate positions in the ground, the resistance of the ground is measured in order to determine the electrode coupling to the ground and a high pass filter - an anti-aliasing filter with a frequency of 0.005 Hz is used to prevent aliasing and also eliminate from the electric dipoles the effect of self-potential.

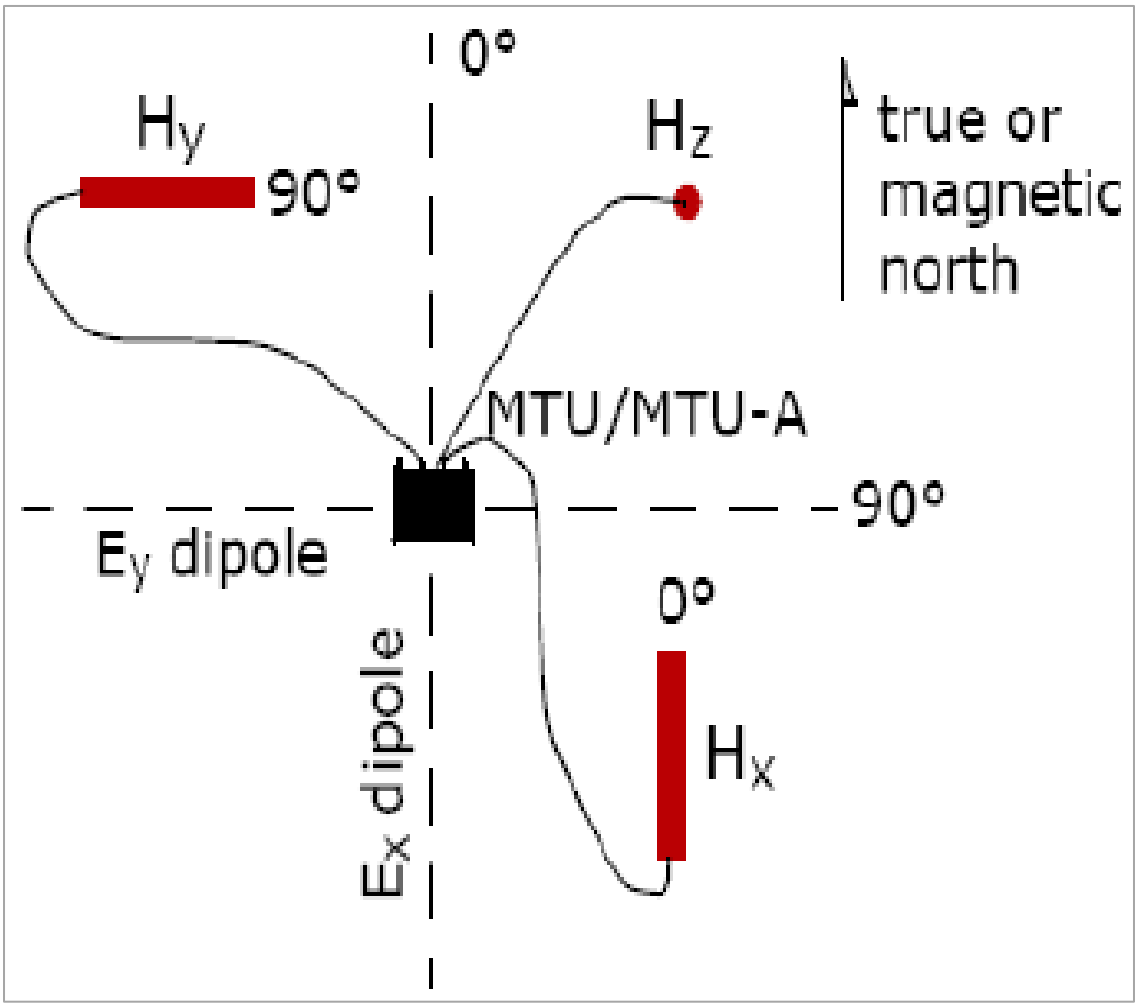

Figure 4.2: A field array for a 5 channel Magnetotelluric data acquisition system (Phoenix Geophysics)

In the field set-up at Arus-Bogoria, magnetic sensors and lead chloride porous pots were used to measure the magnetic and electric fields respectively. To achieve this purpose, both the pots and the magnetic sensors, in their respective positions, were buried in the ground about 30 cm below the surface in order to minimize effects temperature differences between day and night and the noise due to wind.

MT data were acquired for duration of about 20 hours, giving the range from a frequency of 320 Hz down to a few thousandths Hertz. This enabled acquisition of subsurface information to a depth of several tens of kilometres. In this survey the long period data were not achieved at most of the stations because signals were drowned in noise at low frequencies. The depth of penetration of the EM wave is dependent on the frequency of propagation. It follows thus that low frequency waves have the greatest penetration depth compared to waves of high frequency. All stations in Arus geothermal prospect were time synchronized through GPS satellites signals so that the acquired time-series data were processed in combination with other data collected at the same time from other stations far away so as to improve the signal to noise ratio and consequently improve the quality of the field results. A total of 47 MT soundings were considered for interpretation from the Arus study area.

TEM soundings were carried out at the same stations with MT so that the static shift problem with MT could be resolved using TEM results.

4.3 Transient Electromagnetic (TEM) method

The TEM equipment used in this survey is from Zonge and consists of the following:

- A current transmitter
- XMT transmitter controller
- GDP-32 data logger
- A receiver coil with an effective area of 10,000 m^2
- A 120 VA power generator
- A voltage regulator
- A transmitter loop

Before data acquisition, both the receiver and the transmitter controller high-precision crystals are warmed up for a period of about an hour and then synchronized to make sure that induced voltage is measured by the receiver at the correct time after current turn-off.

In the field setup, a 300 m × 300 m transmitter wire loop was used (Figure 4.3) and a current of 13A was transmitted in the wire at frequencies of 16 and 4Hz. The transient signal was recorded in the time interval of 36.14μs to 96.85ms at logarithmically spaced sampling gates after current turn-off. Several repeated transients were stacked and stored, for each frequency, in the internal memory of the Zonge GDP-32 data logger and later transferred to a personal computer for processing. The decay rate of the secondary magnetic field and the current distribution depend on the resistivity structure of the rocks beneath. The rate of decay recorded as a function of time after the current

in the transmitter loop is turned off can, therefore, be interpreted in terms of the subsurface resistivity structure. The depth of penetration in the central loop TEM-sounding is dependent on how long the induction in the receiver coil can be traced in time before it is drowned in noise (Hersir and Björnsson, 1991).

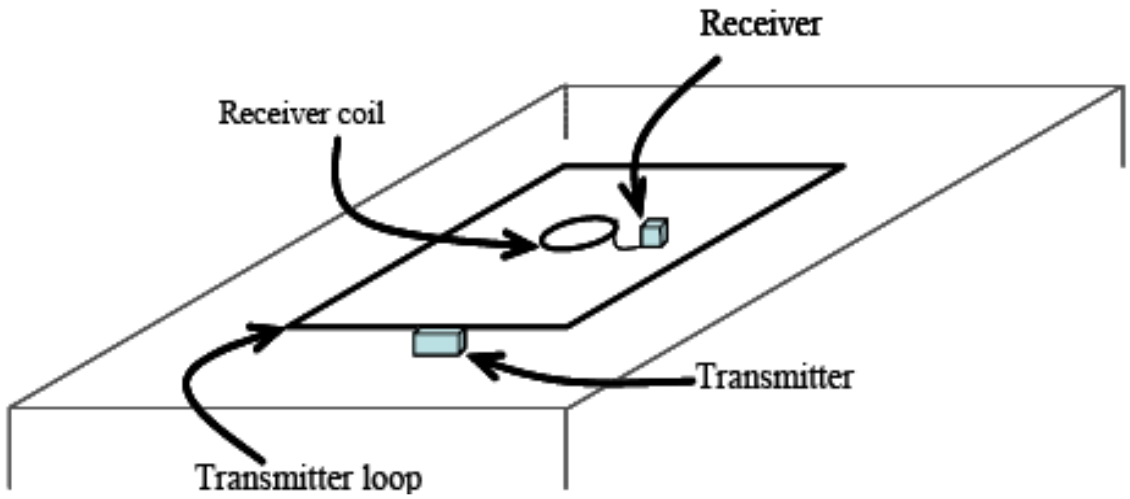

Figure 4.3: Central-loop time domain Transient Electromagnetics field layout (Muturia, 2013)

4.4 Data processing

4.4.1 Magnetotelluric data processing

After downloading time-series data from the MT equipment the data is inspected using a program called Synchro-Time Series Viewer which is provided by equipment manufacturer, Phoenix Geophysics of Canada (Phoenix Geophysics, 2005). The Synchro-Time Series Viewer program permits the operator to view and print the power spectra derived from the raw time-series data, the graphical representations of the raw

time-series data as well as the coherence between pairs of orthogonal magnetic and electric components. SSMT2000 program, which is provided by the manufacturer of the equipment, (Phoenix Geophysics, 2005) is used to process raw the time-series data. Prior knowledge of magnetic declination is needed to be provided into the start-up file so that the program spins to the geographic N-S, the impedance tensor elements. In Arus-Bogoria area magnetic declination was zero and therefore rotation was not necessary. The parameter file was first edited to reflect the data acquisition setup and then the time-series data Fourier transformed to frequency domain.

4.4.1.1 Time series to frequency domain conversion

Fast Fourier Transforms (FFT) are commonly used to transform the measured time series to the frequency domain (Vozoff, 1991). Usually a raw spectrum with a number of data points divided into 2 frequencies is obtained. These frequencies are equally distributed on a logarithmic scale, ideally 6-10 periods in every decade. To smoothen the final spectra, a window function is used to average over the neighboring frequencies. The auto- and cross-spectra segments which are products of the field components and their complex conjugate are computed from the portions of the original time series for every frequency. The time series data is then transformed to frequency domain through Fourier transform as shown in Eqn 4.1 below:

$$H_x(t) \rightarrow H_x(\omega); \qquad H_y(t) \rightarrow H_y(\omega); \tag{4.1a}$$

$$E_x(t) \rightarrow E_x(\omega); \qquad E_y(t) \rightarrow E_y(\omega); \tag{4.1b}$$

4.4.1.2 Magnetotelluric transfer function estimation

The evaluation of MT transfer functions needs averaging of spectra over a number of closely spaced frequencies of the corresponding field components in the frequency domain, which can be obtained from the electric and magnetic field spectra segments as:

$$E_x = Z_{xx}H_x(\omega) + Z_{xy}H_y(\omega) \tag{4.2a}$$

$$E_y = Z_{yx}H_x(\omega) + Z_{yy}H_y(\omega) \tag{4.2b}$$

The impedance equations are solved assuming Z_{ij} to be constant over an averaging band (window), which is physically reasonable if the bands are narrow enough. In each band, each equation has cross-power taken with H_x and H_y in turn giving equations:

$$\langle E_x H_x^* \rangle = Z_{xx}\langle H_x H_x^* \rangle + Z_{xy}\langle H_y H_x^* \rangle \tag{4.3a}$$

$$\langle E_y H_x^* \rangle = Z_{yx}\langle H_x H_x^* \rangle + Z_{yy}\langle H_y H_x^* \rangle \tag{4.3b}$$

$$\langle E_x H_y^* \rangle = Z_{xx}\langle H_x H_y^* \rangle + Z_{xy}\langle H_y H_y^* \rangle \tag{4.3c}$$

$$\langle E_y H_y^* \rangle = Z_{yx}\langle H_x H_y^* \rangle + Z_{yy}\langle H_y H_y^* \rangle \tag{4.3d}$$

where $H_x^*(\omega)$ and $H_y^*(\omega)$ are conjugates of the horizontal magnetic field components.

Equations 4.3a-d can be solved for Z_{ij} as follows:

$$Z_{xx} = \frac{\langle E_x H_x^* \rangle \langle H_y H_y^* \rangle - \langle E_x H_y^* \rangle \langle H_y H_x^* \rangle}{\langle H_x H_x^* \rangle \langle H_y H_y^* \rangle - \langle H_x H_y^* \rangle \langle H_y H_x^* \rangle} \tag{4.4a}$$

$$Z_{xy} = \frac{\langle E_x H_x^* \rangle \langle H_x H_y^* \rangle - \langle E_x H_y^* \rangle \langle H_x H_x^* \rangle}{\langle H_y H_x^* \rangle \langle H_x H_y^* \rangle - \langle H_y H_y^* \rangle \langle H_x H_x^* \rangle} \tag{4.4b}$$

$$Z_{yx} = \frac{\langle E_y H_x^* \rangle \langle H_y H_y^* \rangle - \langle E_y H_y^* \rangle \langle H_y H_x^* \rangle}{\langle H_x H_x^* \rangle \langle H_y H_y^* \rangle - \langle H_x H_y^* \rangle \langle H_y H_x^* \rangle} \tag{4.4c}$$

$$Z_{yy} = \frac{\langle E_y H_x^* \rangle \langle H_x H_y^* \rangle - \langle E_y H_y^* \rangle \langle H_x H_x^* \rangle}{\langle H_y H_x^* \rangle \langle H_x H_y^* \rangle - \langle H_y H_y^* \rangle \langle H_x H_x^* \rangle} \quad (4.4d)$$

4.4.1.3 Remote-reference estimates

In remote referencing method (Gamble *et al.*, 1979; Clarke *et al.*, 1983) sensors are deployed at a site remote from the local measurement site. The natural part of the induced EM field can remain consistent for several kilometres. By measuring selected electromagnetic components at both remote and local stations, we can remove the bias effects produced by noise that is uncorrelated between sites. However correlated noise present in remote as well as local stations cannot be removed by the anticipated noise source, intended frequency range of measurement and general conductivity of the sounding locations. The noise can be wind-induced noise, for which the remote needs to be some hundreds of metres away, or due to cultural disturbances, for which in extreme cases the remote has to be many tens to hundreds of kilometres away.

Both at the local and remote site, the magnetic and electric field spectrum are related linearly. Multiplying these equations by spectra ${R_x}^*(\omega)$ and ${R_y}^*(\omega)$ and averaging over frequency intervals, we get:

$$\langle E_x {R_x}^* \rangle = Z_{xx} \langle H_x {R_x}^* \rangle + Z_{xy} \langle H_y {R_x}^* \rangle \quad (4.5a)$$

$$\langle E_y {R_y}^* \rangle = Z_{yx} \langle H_x {R_y}^* \rangle + Z_{yy} \langle H_y {R_y}^* \rangle \quad (4.5b)$$

$$\langle E_x {R_y}^* \rangle = Z_{xx} \langle H_x {R_y}^* \rangle + Z_{xy} \langle H_y {R_y}^* \rangle \quad (4.5c)$$

$$\langle E_y {R_x}^* \rangle = Z_{yx} \langle H_x {R_x}^* \rangle + Z_{yy} \langle H_y {R_x}^* \rangle \quad (4.5d)$$

These four equations can be solved for the four desired estimates for the remote reference of the impedance tensor elements Z_{ij} as follows:

$$Z_{xx} = \frac{\langle E_x R_x^* \rangle \langle H_y R_y^* \rangle - \langle E_x R_y^* \rangle \langle H_y R_x^* \rangle}{\langle H_x R_x^* \rangle \langle H_y R_y^* \rangle - \langle H_x R_y^* \rangle \langle H_y R_x^* \rangle} \quad (4.6a)$$

$$Z_{xy} = \frac{\langle E_x R_x^* \rangle \langle H_x R_y^* \rangle - \langle E_x R_y^* \rangle \langle H_x R_x^* \rangle}{\langle H_y R_x^* \rangle \langle H_x R_y^* \rangle - \langle H_y R_y^* \rangle \langle H_x R_x^* \rangle} \quad (4.6b)$$

$$Z_{yx} = \frac{\langle E_y R_x^* \rangle \langle H_y R_y^* \rangle - \langle E_y R_y^* \rangle \langle H_y R_x^* \rangle}{\langle H_x R_x^* \rangle \langle H_y R_y^* \rangle - \langle H_x R_y^* \rangle \langle H_y R_x^* \rangle} \quad (4.6c)$$

$$Z_{yy} = \frac{\langle E_y R_x^* \rangle \langle H_x R_y^* \rangle - \langle E_y R_y^* \rangle \langle H_x R_x^* \rangle}{\langle H_y R_x^* \rangle \langle H_x R_y^* \rangle - \langle H_y R_y^* \rangle \langle H_x R_x^* \rangle} \quad (4.6d)$$

where the remote fields are denoted by R_x and R_y.

As with single-station estimation, typically the magnetic field contains less noise than the electric fields, and thus the remote fields R_x and R_y used for the above equations are the remote magnetic fields.

In Arus data set the Fourier transform band averaged cross- and auto- powers were calculated using robust processing method. The cross-powers were then edited using the MTEditor program by masking the noisy data points in order to evaluate coherences for both phase and apparent resistivity (Figure 4.4). The MTEditor program accepts MT plots output by SSMT2000, merges the cross-powers and displays MT parameters graphically. It also enables elimination of cross-powers from the calculations and hence the possibility of editing out poor quality data.

The primary objective of editing is to create a smooth resistivity curve by eliminating those cross- powers that have been moved too far from the mean by noise and related effects. Though it is possible to eliminate data points from being considered, the software does not delete them completely. It places a mask on those unwanted cross-powers, allowing one to revert to the original data at any time. The final cross- and

auto- powers, as well as all relevant MT parameters calculated from them (impedances, apparent resistivity, phase coherences, strike directions etc) are stored in Electrical Data Interchange format (EDI) files. These files can then be exported for inversion and interpretation by the WinGlink Integrated software.

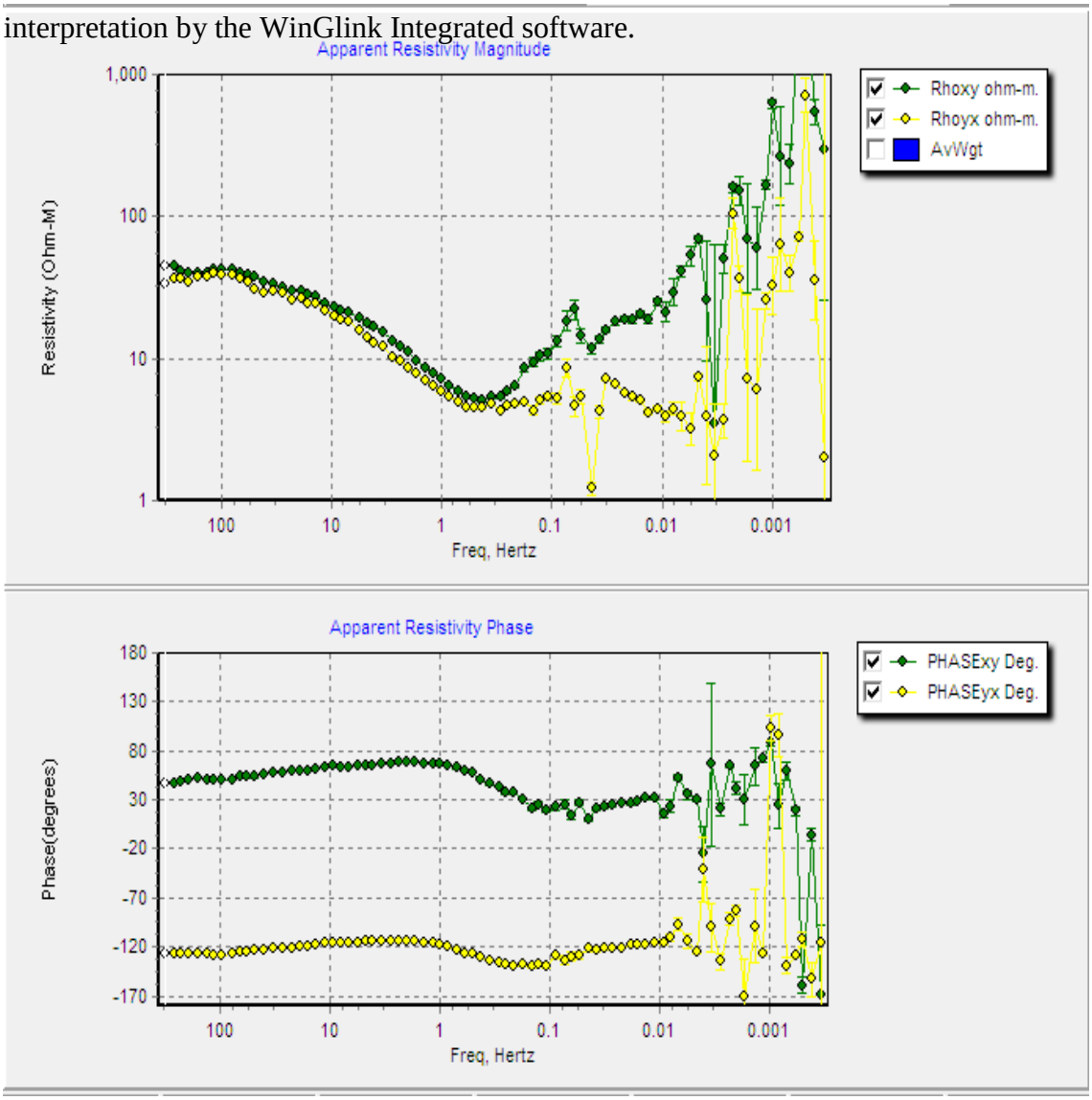

Figure 4.4: MTEditor plot showing apparent resistivity and phase curves

The EDI file from MTEditor was then run through WinGlink Interpretation software for further editing; and the result was then ready for interpretation. Figure 4.5 illustrates

typical examples of processed MT apparent resistivity and phase curves from Arus-Bogoria area. Generally at periods below one second they exhibit 1-D response with both values of apparent resistivity and phase decreasing as the period increases. For periods above ten seconds all curves split apart implying non one-dimensionality with one apparent resistivity increasing as the other decreases. High phase values (>45°) at short periods indicate a conductor at shallow depth.

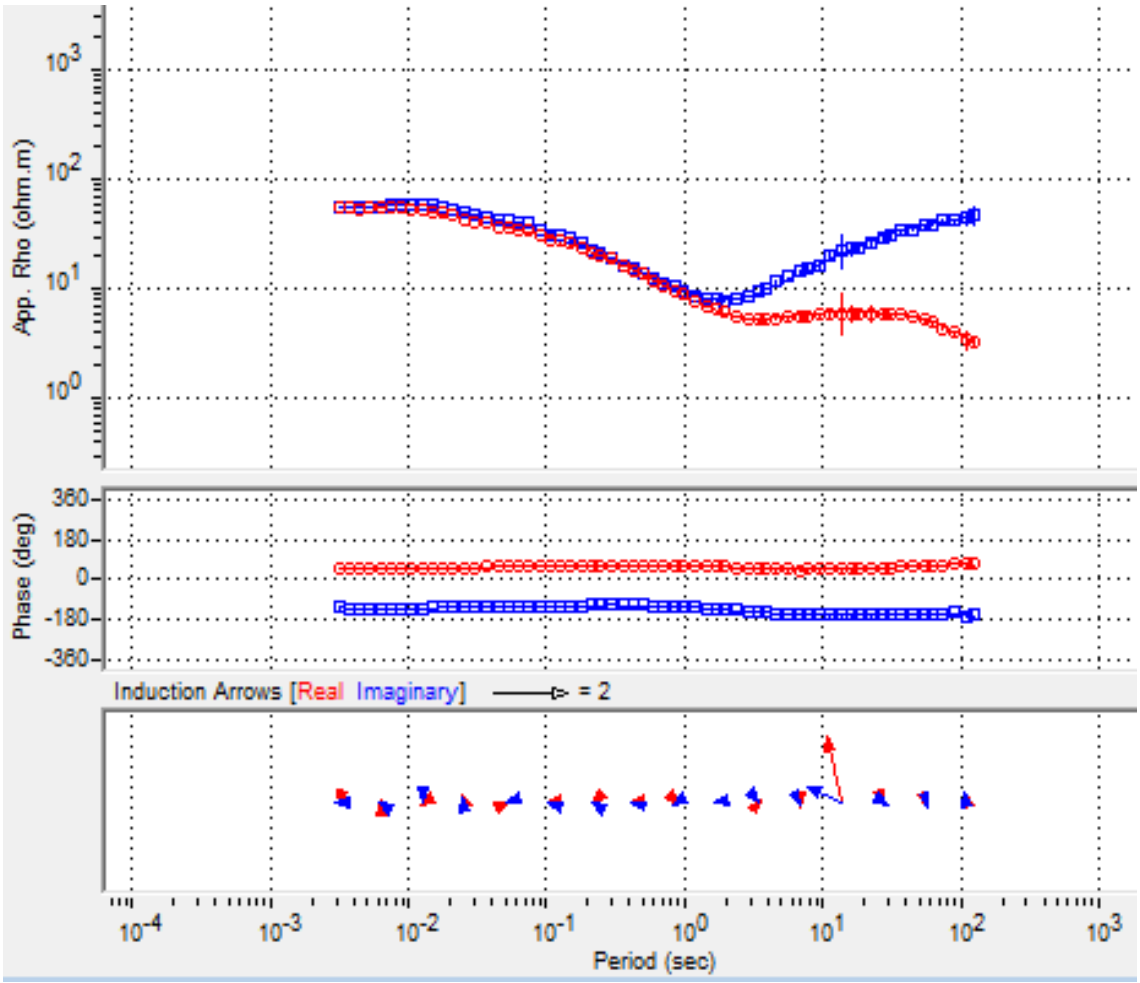

Figure 4.5: Typical examples of apparent resistivity and phase curves of Magnetotelluric soundings in the Arus area.

4.4.2 TEM data processing

The raw TEM data was downloaded from the GDP-32 data logger and fed into a personal computer where it was processed using the program TemxZ. The program averages data collected at same frequency and computes late time apparent resistivity as a function of time after current turn-off. TemxZ program also enables manual editing of the raw data to eliminate inconsistent data points and outliers before the data can be used for interpretation.

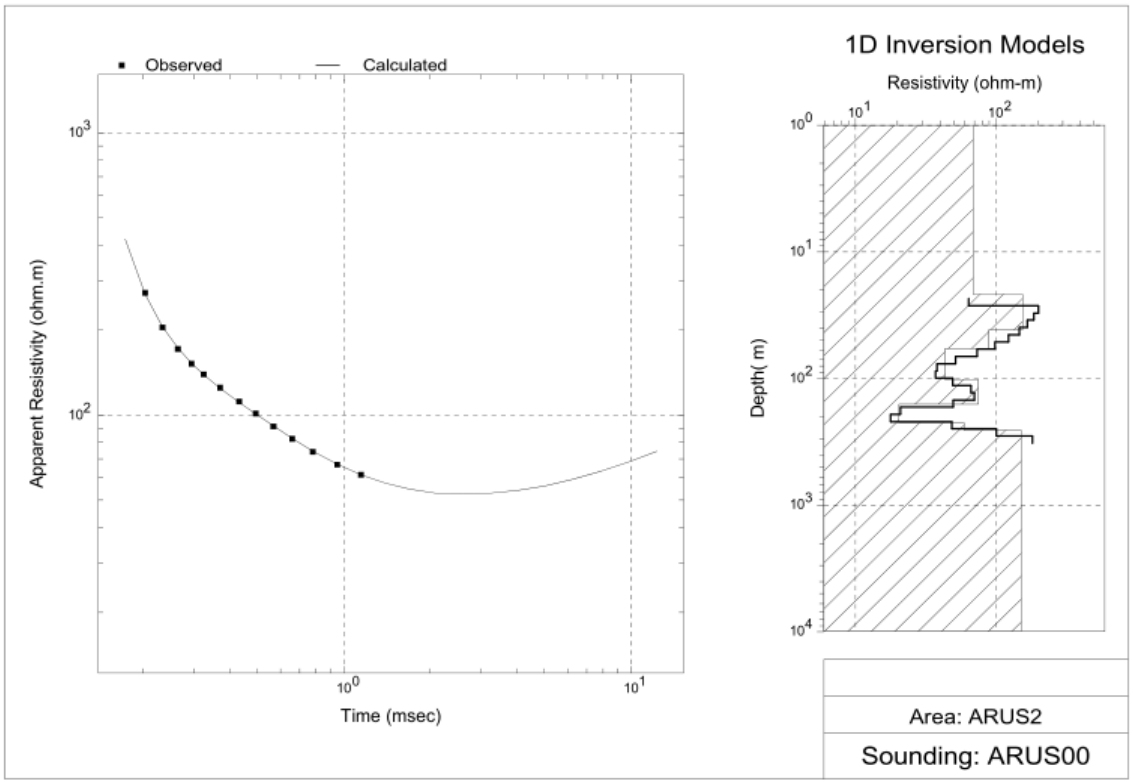

Figure 4.6: Transient Electromagnetics sounding ARUS00 and its 1-D inversion.

The TEM soundings in Arus-Bogoria geothermal prospect were interpreted by 1-D (layered earth) inversion. The resultant curves and their associated 1-D models are presented in Appendix IV. The inversion was done by Occam inversion (Constable *et al.,* 1987) and figure 4.6 shows inversion result from one station ARUS00. The figure illustrates TEM apparent resistivity cure and its interpretation. On the figure, the black solid line is the calculated apparent resistivity obtained from the model shown alongside whereas the black dots are measured late-time apparent resistivities.

In 1-D (layered earth) inversion, it is assumed that the earth has only horizontal layers with varying thicknesses and resistivities. In layered inversion we invert for resistivity values as well as layer thicknesses; in Occam (minimum structure) inversion, layer thicknesses increase exponentially with depth, and we invert for resistivity values. TEM 1-D aims at finding the layered model in which the response best fits the measured values.

CHAPTER FIVE

RESULTS AND DISCUSSION

5.1 Introduction

This section presents the results and deductions arrived at after the data analysis procedures outlined in chapter four were applied. The main software used in the interpretation of these data is WinGlink software. It is based on nonlinear conjugate gradient (NLCG) inversion code which is a forward and inverse modeling algorithm developed by Rodi and Mackie (2001). The forward model is computed using finite difference equations while the inversion seeks to achieve the lowest root mean square error and the smoothest model.

In 2-D case, Maxwell's equations can be written in terms of decoupled TE and TM polarizations for current flowing parallel and perpendicular to strike; thus the complex resistivities for the TE and TM mode are expressed as:

$$\rho_{TE} = \frac{1}{\omega\mu}\left|\frac{E_x}{H_y}\right|^2 \quad \text{and} \quad H_y = \frac{1}{i\omega\mu}\frac{\partial E_x}{\partial z} \tag{5.1}$$

$$\rho_{TM} = \frac{1}{\omega\mu}\left|\frac{E_y}{H_x}\right|^2 \quad \text{and} \quad E_y = \rho\frac{\partial H_x}{\partial z} \tag{5.2}$$

The algorithms used by Rodi and Mackie (2001), solve Eqns. 5.1 and 5.2 by segmenting the half space into rectangular blocks of different dimensions, each assigned a constant resistivity.

5.2 1-D iso-resistivity maps

In this sub-section, contoured resistivity distribution maps based on Occam inversion were prepared using the WinGlink software. The resistivity is coloured and contoured in a logarithmic scale. The values used to build up these maps are of two kinds: the values of the parameter at each data collection station and the interpolated values of the same parameter. The general elevation of Arus is about 1300 – 1600 m.a.s.l. In this section the iso-resistivity maps are presented from 1000 m.a.s.l down to 4500 m.b.s.l. The maps are plotted at constant depth which is dimmed to be more representative since electrical resistivity of the subsurface varies with topography.

5.2.1 Resistivity Map at 1000 m.a.s.l

The resistivity map at 1000 m.a.s.l is shown on Figure 5.1 below. The relatively low resistivity predominantly covers almost the entire study area with a very low resistive zone (marked by resistivity < 8 ohm-m) observed at the central part of Arus, towards the west of the study area. This low resistivity can be interpreted to be related to hydrothermal alteration and also to show the depth of the clay cap around the prospect.

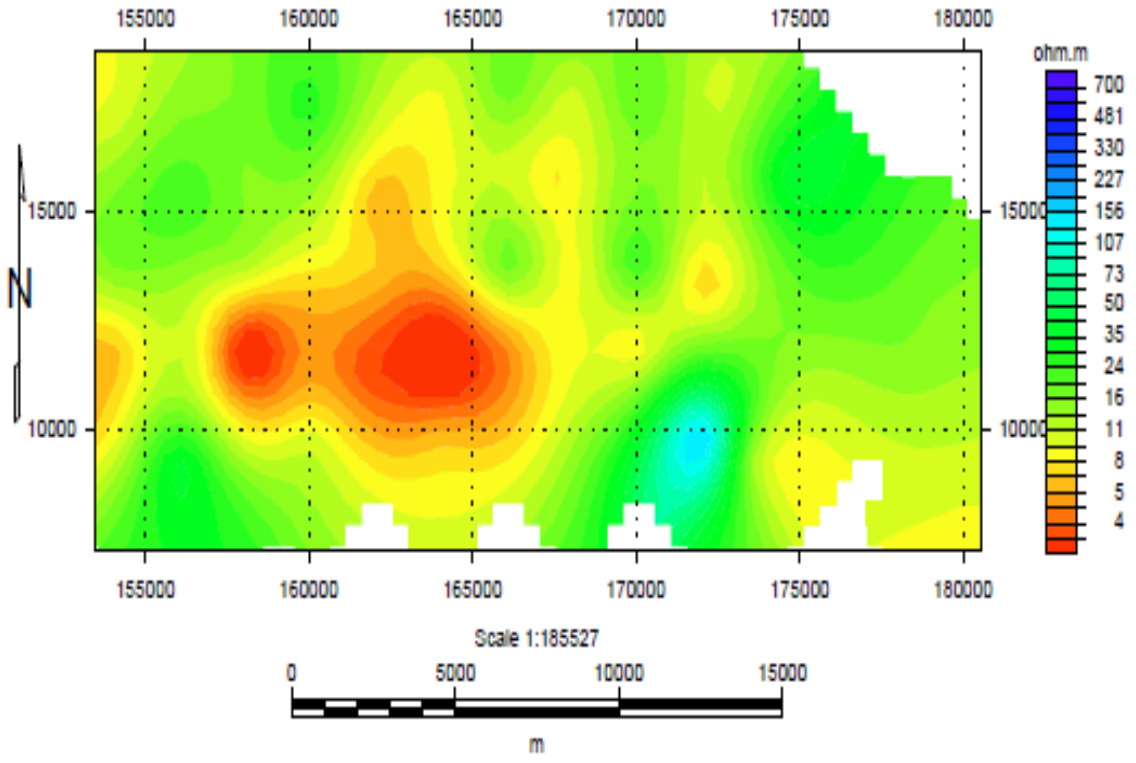

Figure 5.1: Resistivity map at 1000 m.a.s.l based on Occam inversion

5.2.2 Resistivity at sea level

Figure 5.2 below shows the resistivity map at sea level. This elevation is approximately 1.5 km below the surface. A fairly high resistivity is evident to the south of the prospect area cutting through the centre and extending northward. The fairly high resistivity zone is around Molo Sirwe, Mugurin and Mukuyuni and it can be attributed to be due to hydrated mineralogy. Low resistivity anomaly is seen on the western part of the prospect area and can be interpreted to be acting as the seal to the geothermal system. Generally the resistivity distribution at sea level can be inferred to delineate the reservoir level around the prospect area.

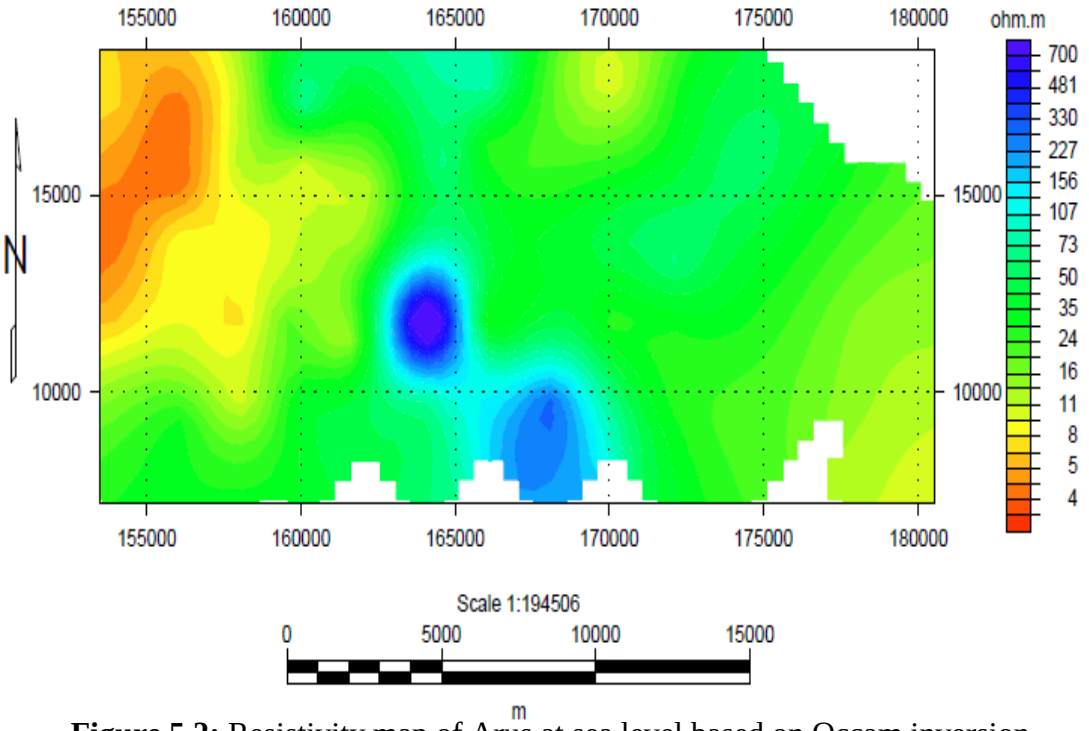

Figure 5.2: Resistivity map of Arus at sea level based on Occam inversion

5.2.3 Resistivity at 1000 m.b.s.l

The resistivity map at 1000 m.b.s.l is shown on Figure 5.3 below. At this elevation high-temperature alteration (resistive core) is visible from the prospect area and covering entirely the study area, marked by resistivity > 20 ohm-m. This high resistivity could probably be as a result of high temperature minerals like epidote and chlorite. A structural control can be seen in the central part of the plot and appearing to be aligned in the North-West direction. A very high resistive zone occurs at the middle of the plot around Molo Sirwe and this can be discerned to be an intrusive (hot) body.

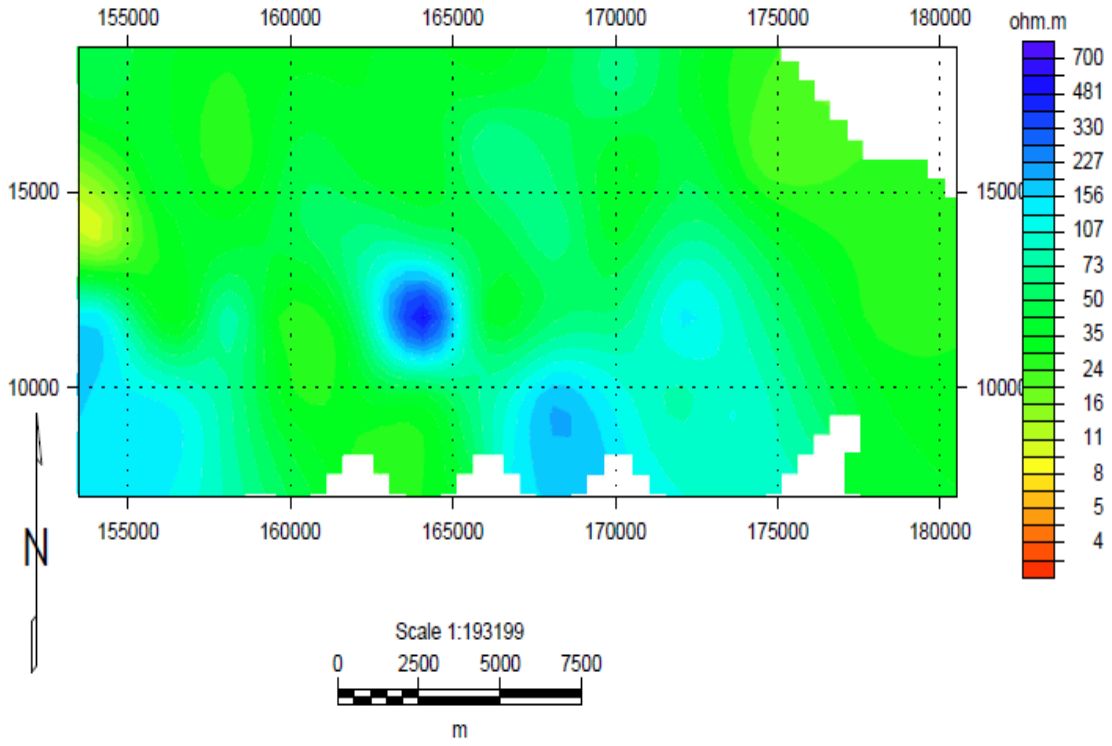

Figure 5.3: Resistivity map at 1000 m.b.s.l based on Occam inversion

5.2.4 Resistivity at 2500 m.b.s.l

Resistivity map at 2500 m.b.s.l is shown on Figure 5.4 below. A high resistivity persists throughout the plot. The high resistivity could still be related to high temperature mineral alteration. The structural control in the middle of the plot aligned in the North-West direction can now be clearly seen, showing some lineaments in that direction. The very high resistive body is seen to spread northwesterly towards Chebiwon.

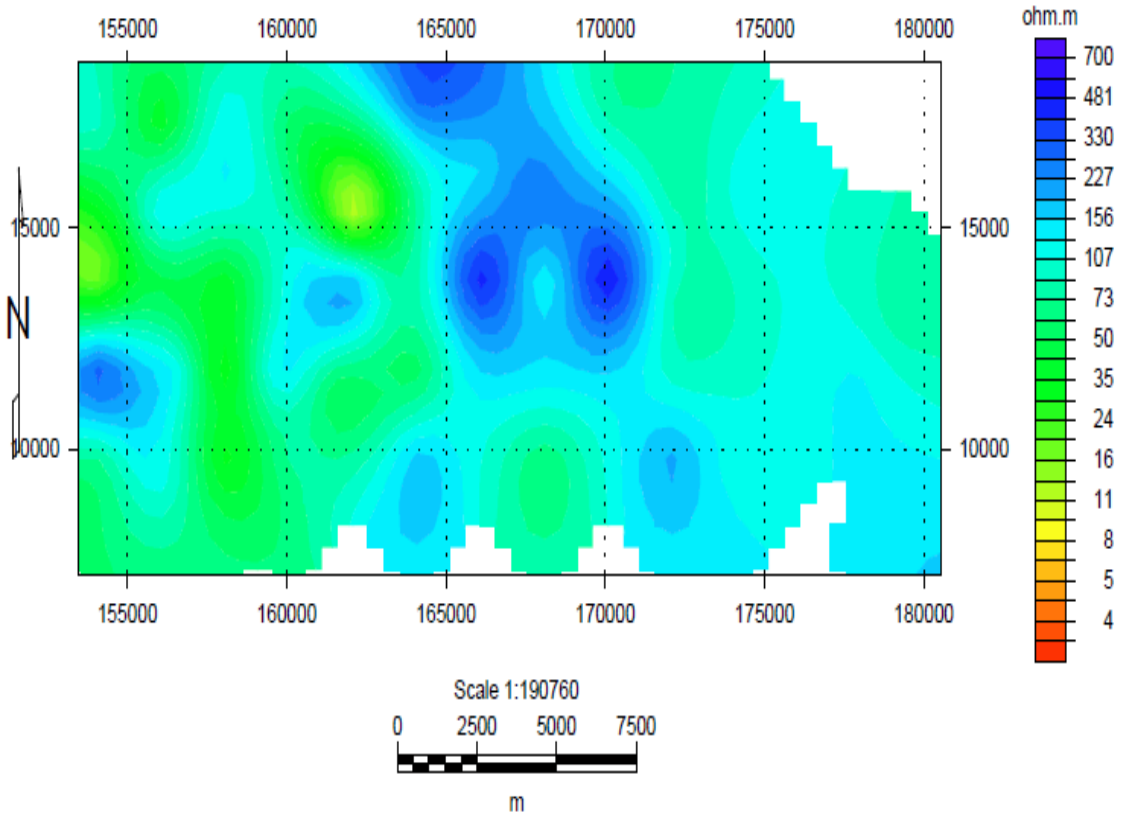

Figure 5.4: Resistivity map at 2500 m.b.s.l based on Occam inversion

5.2.5 Resistivity at 4500 m.b.s.l

Figure 5.5 shows the resistivity plot at 4500 m.b.s.l. This elevation is about 6 km below the surface. A very high resistivity covers entirely the eastern part of the plot whereas a fairly low resistivity could be traced on some parts of the western section. It shows clearly the distinction between the eastern part and the western part of the prospect area. This reveals a structural control between the active system around Molo Sirwe and cold intrusions on the eastern part of the prospect.

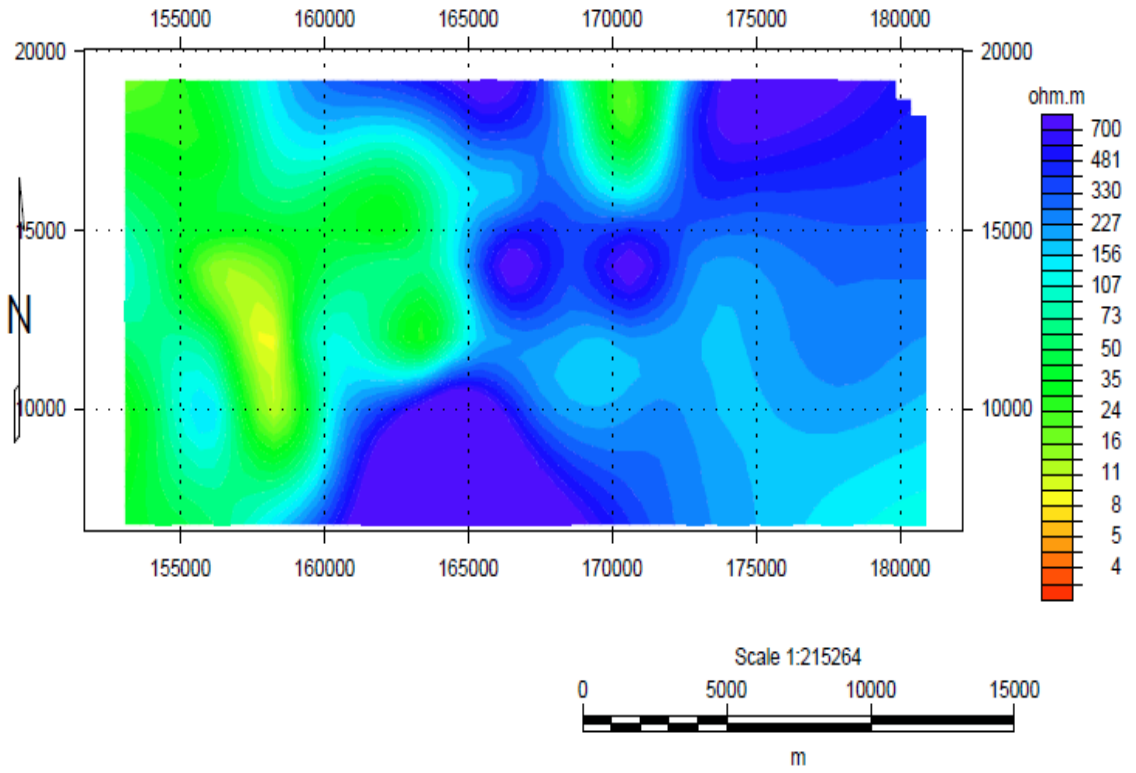

Figure 5.5: Resistivity map at 4500 m.b.s.l based on Occam inversion

5.3 2-D Resistivity cross-sections

To better examine the resistivity variations at depth, five cross sections were taken across the geological structures in the area. These 2-D cross sections are shown in Figures 5.6 to 5.10.

5.3.1 Resistivity cross-section West - East1

The resistivity cross-section shown in Figure 5.6 below is along West- East direction and cuts the Northern part of the prospect. It reveals a typical resistivity structure for a geothermal system on the western part as described above. On the eastern part the deep resistive body could be an intrusion on that part of the prospect.

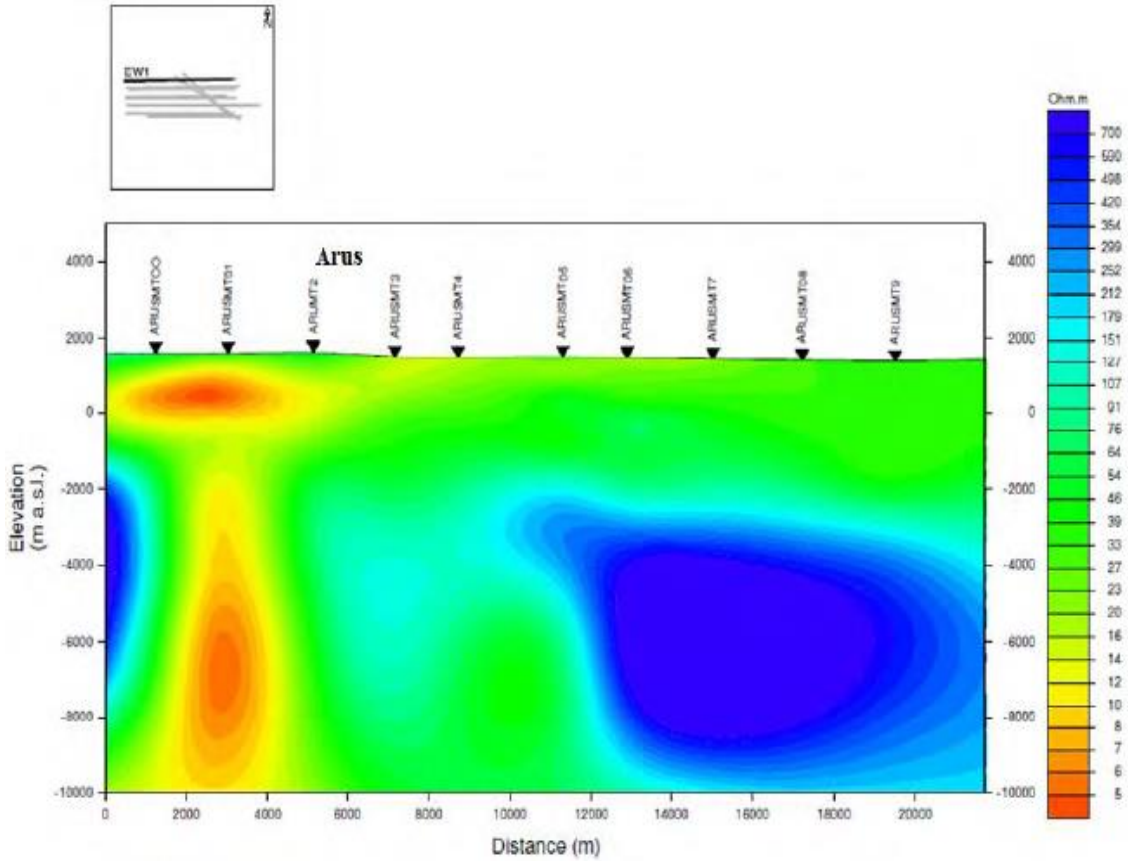

Figure 5.6: Resistivity cross-section West - East1

5.3.2 Resistivity cross-section West - East2

A closer look at the cross-section below (Figure 5.7) taken across Molo Sirwe shows that there is a clear hydrothermal activity on the western part of the prospect and a structure can be seen in the middle of the plots which can be a clear indication of a structurally controlled activity at Molo Sirwe. At deeper depths resistive bodies are seen on both parts of the plot (Western and Eastern). On the western part it could be a zone of high temperature hydrated minerals and on the eastern part it is a cooling intrusion since we also don't see much activity at the surface to prove that it's a high temperature zone.

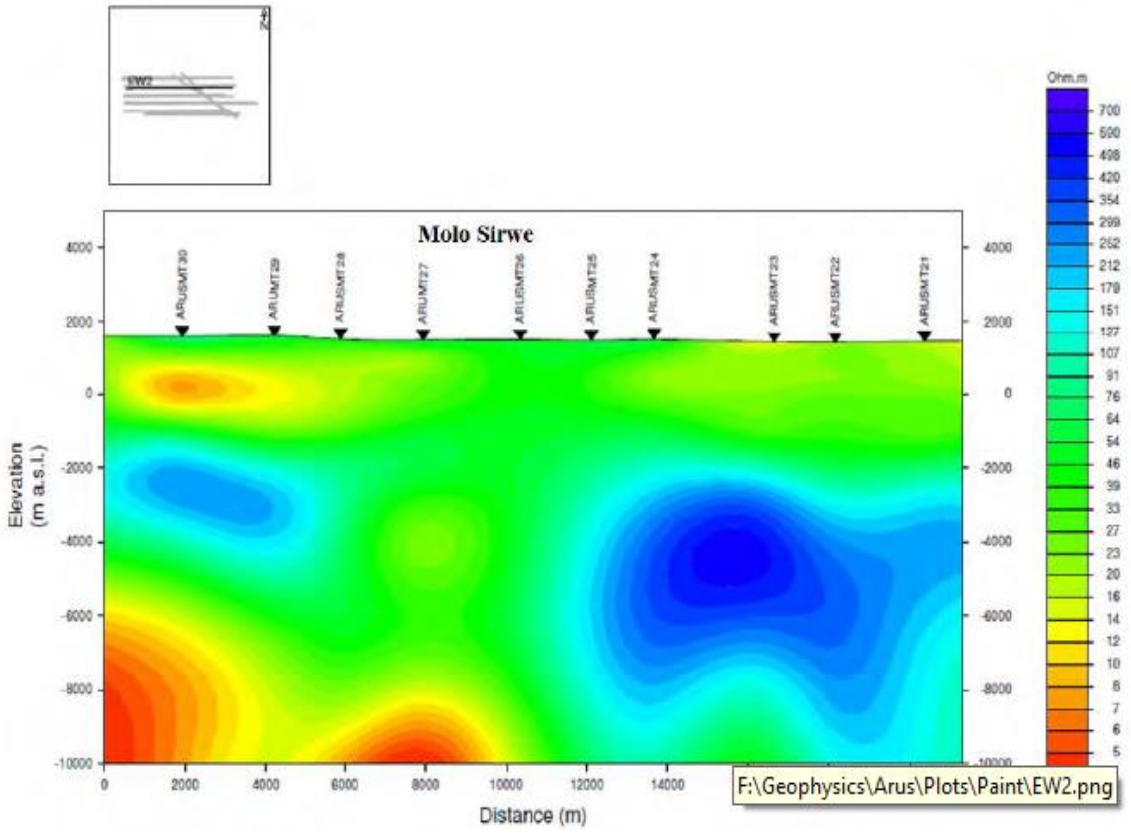

Figure 5.7: Resistivity cross-section West - East2

5.3.3 Resistivity cross-section West - East5

This section on Figure 5.8 is taken almost in the middle of the prospect and a fairly high resistivity is distinct from the system seen on the western part showing some structural controls. The high resistivity anomaly is beneath the area with numerous gas holes on the surface indicative of carbon dioxide reservoirs around the area. The presence of carbon dioxide gas is a further proof of the presence of a hot body beneath.

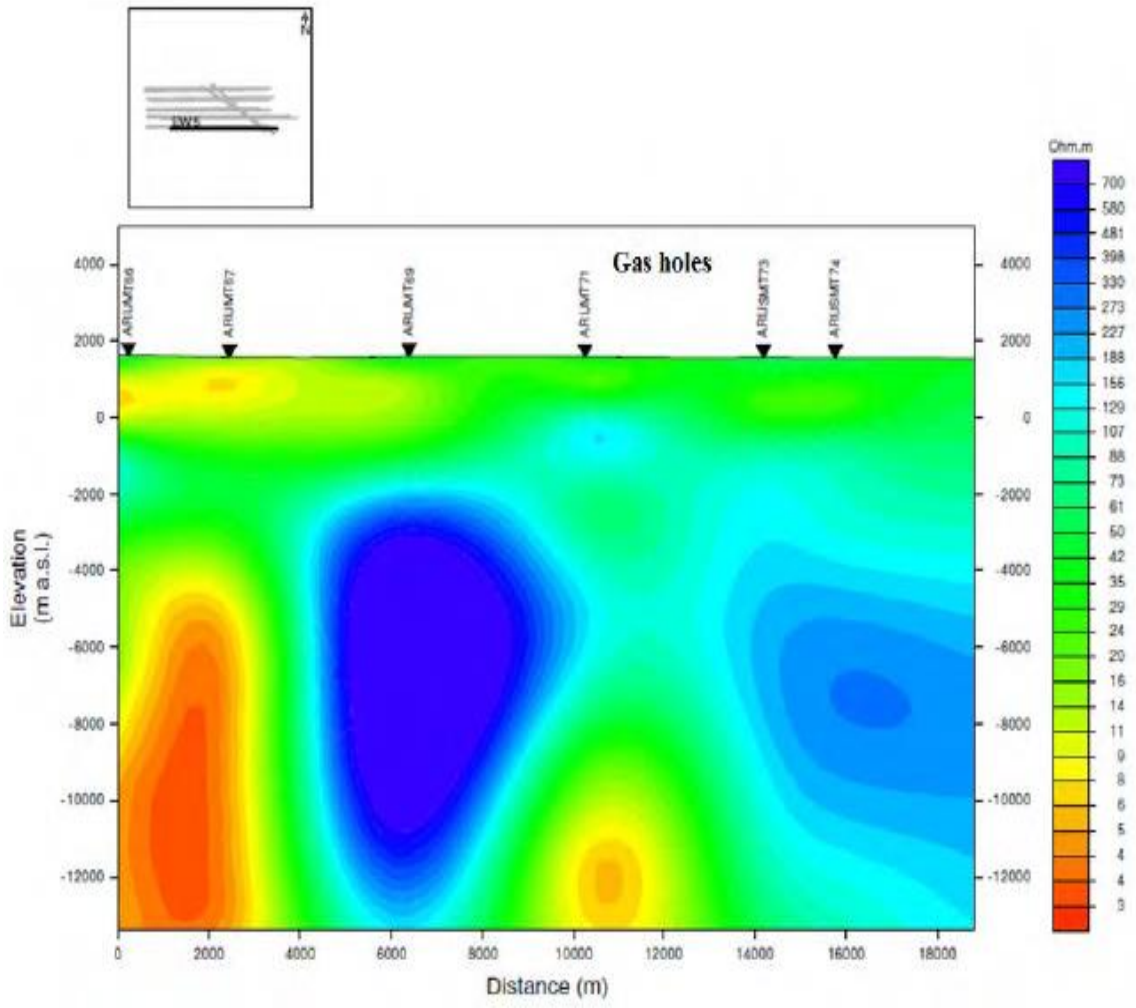

Figure 5.8: Resistivity cross-section West - East5

5.3.4 Resistivity cross-section West - East1 at shallow depths

A look at shallow TEM profiles reveals a zone of alteration near the surface at Arus where several hot springs and fumaroles are found. Also a zone of hydrothermal alteration is seen which seems to be structurally controlled as it outflows near the surface. This can also be interpreted as our outflow zone.

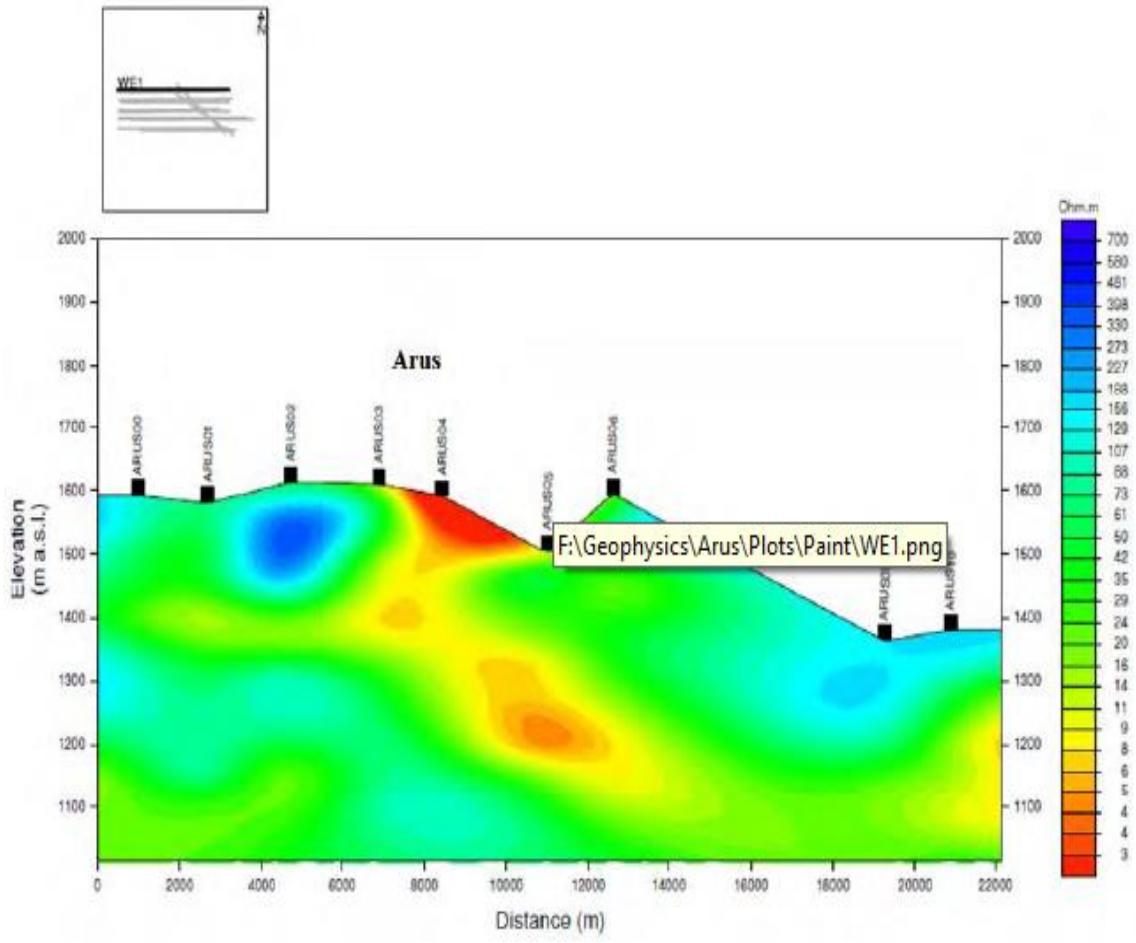

Figure 5.9: Transient Electromagnetics Resistivity cross-section West - East1.

5.3.5 Resistivity cross-section West - East5 at shallow depths

In the middle part of the prospect where several gas holes are found (Figure 5.10) a fairly resistive anomaly is seen at about 150 meters below the surface which is probably the gas reservoirs which overlays a conductive zone of hydrothermally altered minerals or clays.

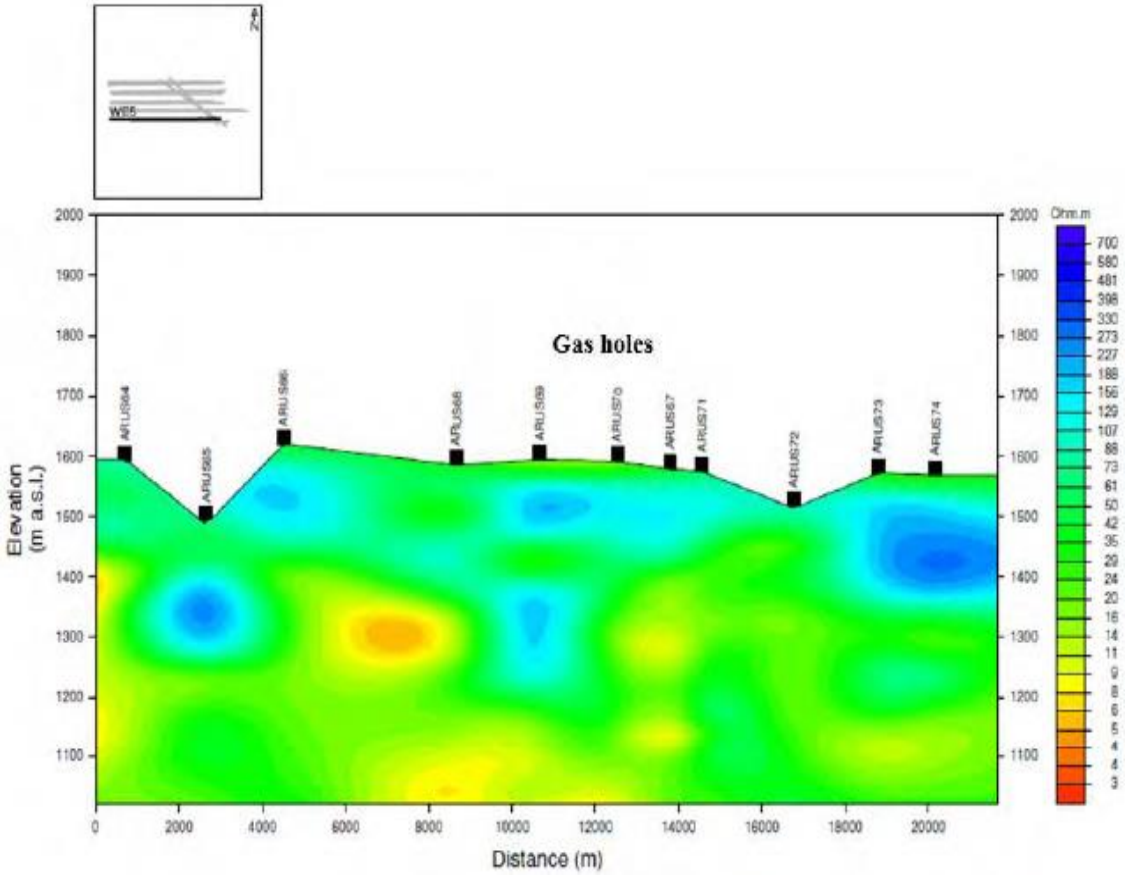

Figure 5.10: Transient Electromagnetics resistivity cross-section West - East5

CHAPTER SIX

CONCLUSIONS AND RECOMMENDATIONS

6.1 Conclusions

The interpretation of the integrated MT and TEM data and the consequent resistivity distribution maps and cross-sections from Arus geothermal prospect reveals that:

A geothermal system exists to the west of the prospect area. The hotter reservoir conditions can be clearly discerned in this area, around Molo Sirwe. This area is potentially a good high-temperature area. This may also be the upflow of the geothermal system. The resistivity distribution confirms a possible geothermal system upflowing to the Northwest and is structurally controlled.

TEM imaging shallower depth indicates a small irregular relatively resistive anomalous body that may be gas reservoirs. This may explain the numerous gas emitting holes in Mukuyuni area.

6.2 Arus Geothermal Prospect Conceptual Model

Conceptual models are an important basis of field development plans, i.e. in selecting locations and targets of wells to be drilled (Axelsson, 2013) and ultimately the foundation for all geothermal resource assessments, particularly volumetric assessments and geothermal reservoir modelling (Axelsson, 2013). In developing a conceptualized model for Arus prospect, the following were taken into consideration:

Heat source: The Arus geothermal prospect is not associated with any central volcano however; a heat source can be postulated to be dike intrusive at depth where there is

deep fluids circulation and heating by the intrusives. This is based on experiences in other fields. The Arus model is that of fluids from edges of rift axially flows deep due to the near vertical faults seen in the area, the fluids are then heated up by deep intrusive and due to buoyancy they flow back towards the sources where they manifests as the fumaroles and hot springs.

Hydrogeology (*Fluid & permeability*): The location of Arus prospect on the rift floor where hydro geologic regime comprise of recharge from the higher rift scarps and the intense rift floor fracture/faulting resulting from extensional tectonics of continental rifting. The extensional tectonics is coupled with strike-oblique faults and transfer zones. This provides a good structural set up that allows water from the rift scarps to penetrate deep into the crust towards the magma bodies under the rift floor and normal faults conducting hot fluids from deep into possible geothermal reservoirs at shallower depth.

System Capping: The rocks in the area are mainly Pliestocene lavas with resent sediments in discrete graben in the area. The expected capping is this sediment with intermittent lavas. However resistivity data points to shallow conductive body to the west that could be considered a clay capping system. The clay cap is confined to the west and is not present on the other parts.

Conceptualized model

Based on geophysics and surface geology work; a conceptualized model was generated (Figure 6.1). The geothermal system may mainly be to the west of the area and probable

smaller system to the east. The two proposed systems are divided by the Kisanana-Hannigton fault.

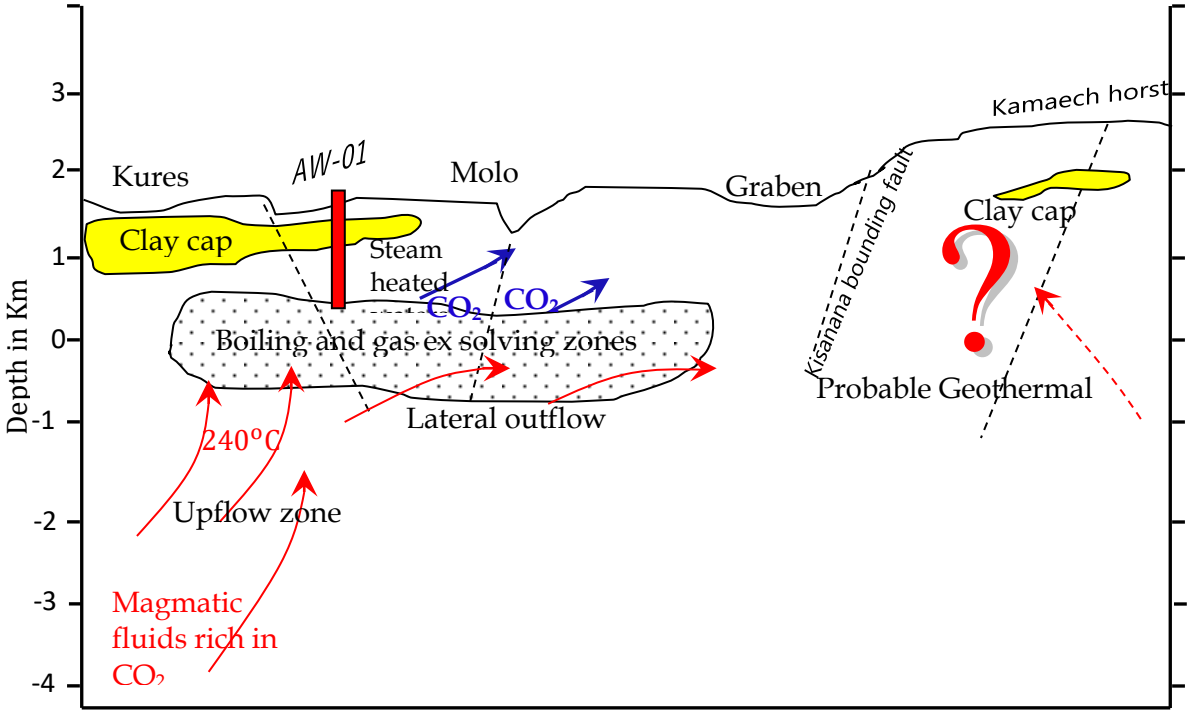

Figure 6.1: Arus geothermal prospect conceptual model

6.2 Recommendations

Based on the coverage it is recommended that one deep vertical exploratory well (AW-01) be drilled in area between Kures and Arus area. The coordinate location is northing 14000 and easting 16100 (Figure 6.2 below).

Other geophysical exploration methods such as gravity, ground magnetic and seismic should be applied for a better resolution and mapping of the depth, nature and size of the intrusive body. More advance gravity data interpretation methods like Tensor Euler deconvolution technique to be conducted in Arus-Bogoria for further verification of the

findings. Tensor Euler deconvolution has added advantage over conventional Euler in that it uses measured gradients rather than calculated gradients, this honors the multidimensional responses, and the deconvolution can be implemented without gridding or profiling the data which by its nature is interpolation.

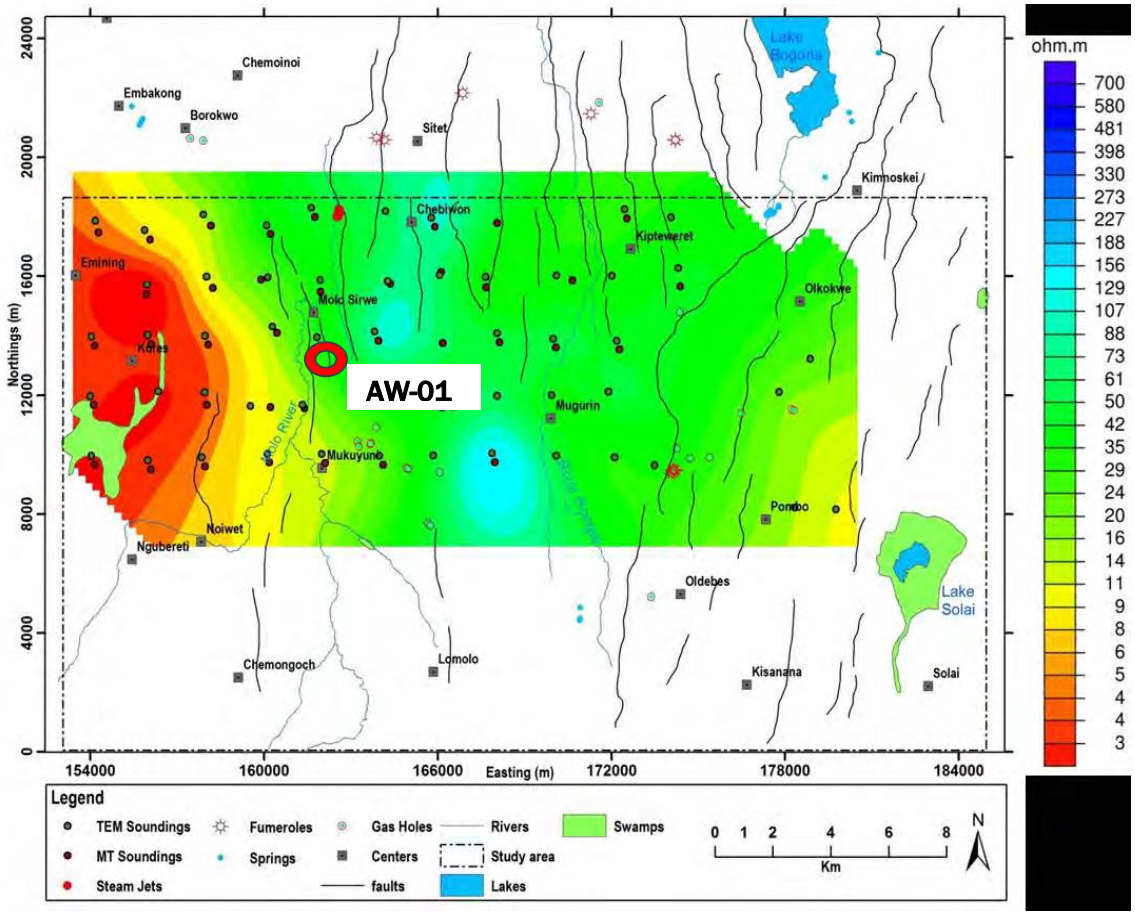

Figure 6.2: Proposed exploratory well site (AW-01) in Arus prospect

More infill data need to be collected on the western part and the eastern parts of the prospect in order to clearly define the geothermal system seen on the western part and also the cooling system on the eastern part. This will also closely map the structural controls evident between the western and the eastern part.

REFERENCES

Árnason, K., (1989). *Central loop transient electromagnetic sounding over a horizontally layered earth.* Orkustofnun, Reykjavík, report OS-89032/JHD-06, 129 pp.

Árnason, K., Karlsdóttir, R., Eysteinsson, H., Flóvenz, Ó.G. and Gudlaugsson, S.Th. (2000). The resistivity structure of high-temperature geothermal systems in Iceland. *Proceedings of the World Geothermal Congress 2000, Kyushu -Tohoku, Japan*, 923–928.

Árnason, K. (2008). *The magneto-telluric static shift problem*. Iceland GeoSurvey – ISOR, report, ISOR08088. pp17.

Árnason, K., Eysteinsson, H., Hersir, G. P. (2010). Joint 1D inversion of TEM and MT data and 3D inversion ofMT data in the Hengill area, SW Iceland. *Geothermics*, **39**: 13–34

Archie, G.E., 1942: The electrical resistivity log as an aid in determining some reservoir C-characteristics. *Journal of the Society of the American Institute of Mining, Metallurgical, and Petroleum Engineers*, **146**: 54-67.

Axelsson, G., (2013). Dynamic modelling of geothermal systems. *Proceedings* of the "Short Course onConceptual Modelling of Geothermal Systems", organized by UNU-GTP and LaGeo, Santa Tecla, El Salvador, 21 pp.

Christensen, A., Auken, E., and Sørensen, K. (2006). The transient electromagnetic method. *Groundwater Geophysics*, **71**: 179-225.

Clarke, J., Gamble, T.D., Goubau, W.M., Koch, R.H., Miracky, R.F. (1983). Remote reference magnetotellurics: Equipment and procedures. *Geophysical Prospecting Journal*, **31**: 149-170.

Constable, S.C., Parker, R.L., Constable, C.G. (1987). Occam's inversion: a practical algorithm for generating smooth models from electromagnetic data. *Journal of Geophysics,* **52**: 289–300.

DeGroot-Hedlin, G. (1991). Removal of static shift in 2 dimensions by regularized inversion. *Journal of Geophysics*, **56**: 2102-2106.

Fairhead, J.D. (1976). The structure of the lithosphere beneath the eastern rift, East Africa, deduced from gravity studies. *Tectonophysics*, **30**: 269-298.

Gamble, T.D., Goubau, W.M., and Clarke, J. (1979). Magnetotelluric with a remote magnetic reference. *Journal of Geophysics,* **44**: 53-68.

Geotermica Italiana Srl., 1987: *Geothermal reconnaissance survey in the Menengai-Bogoria area of the Kenya Rift Valley*. UN (DTCD)/ GOK.

Glover, R.B., (1972). Chemical Characteristics of Water and Steam Discharges in the Rift Valley of Kenya. *Unpublished report, Geothermal Resources Exploration Project, United Nations – East Africa Power and Lighting, Nairobi, Kenya*

Griffiths, P.W., (1977), Geology of the Lake Hannington (Bogoria) – Perkerra River area, Kenya Rift Valley: *Ph.D.thesis, Royal Holloway, University of London*

Hamilton, R.M., and Muffler, L.J.P., (1972). Microearthquakes at The Geysers geothermal area, California. *Journal of Geophysical Research*, **77**: 2081-2086

Hersir, G.P., and Björnsson, A. (1991). *Geophysical exploration for geothermal resources. Principles and applications*. UNU-GTP, Iceland, report 15, pp.94

Jones, A.G., (1988). Static shift of magnetotelluric data and its removal in a sedimentary basin environment. *Journal of Geophysics,* **53**: 967-978.

Jones, A.G., and Groom, R.W. (1993). Strike-angle determination from the magnetotelluric impedance tensor in the presence of noise and local distortion: rotate at your peril! *Geophysical Journal International,* **113**: 524-534.

Karingithi, C. (2006). The Geochemistry of Arus and Bogoria geothermal prospects. *Proceedings*, 11th conference of the Geological Society of Kenya, Geology for Industrial Growth, Wealth Creation and Poverty alleviation, Nairobi Kenya 17-19th August, 2006: 62-65

Keary, P., Brooks, M., and Hill, I. (2002). *An introduction to geophysical exploration.* Blackwell Scientific Publications, Oxford, pp. 208-209

Lagat, J. (2008). Geology and geothermal resource utilization options at Arus-Lake Bogoria prospect, northern Kenya rift. In: *Proceedings* of ARGeo-C2 Conference Entebbe Uganda 24-28th November, 2008: 71-73

Lúdvík, S. G. (2009). Geophysical methods used in geothermal exploration. Report IV In:Geothermal training in Iceland 2009. UNU-GTP, Iceland, 409-439.

Mariita, N.O. (2003). An Integrated geophysical study of the northern Kenya rift crustal structure: Implications for geothermal energy prospecting for Menengai area. *PhD dissertation, University of Texas at El Paso, USA.*

Muñoz, G. (2014). Exploring for geothermal resources with electromagnetic methods. *Survey Geophysics*, **35**:101–122

Muturia, C.L. (2013). Multi-dimensional interpretation of Electromagnetic data from Silali geothermal field in Kenya: comparison 1-D, 2-D and 3-D MT inversion. *MSc thesis, United Nations University, Iceland. Pp. 3-36.*

NOCK (1987). Aeromagnetic data interpretation of the Winam Gulf and the East African Rift areas in Kenya. *National Oil Corporation of Kenya, unpubl. report no. 26/2 16D.*

Ogawa, Y., and Ushinda, T., (1996). A two-dimensional magnetotelluric inversion assuming Gaussian static shift. *Geophysical Journal International,* **126**: 69-76

Palacky, G.J. (1987). Resistivity characteristics of Geologic targets. In: *Electromagnetic methods in applied geophysics,1. Theory.* Society of Exploration Geophysics, Tusla, OK, USA.

Parkinson, W.D. (1959). Direction of rapid geomagnetic fluctuations. *Geophysics J.* 2 1-14.

Pellerin, L. and Hohmann, G.W. (1990). Transient electromagnetic inversion – a remedy for magnetotelluric static shifts, *Journal of Geophysics,* **55**: 1242-1250.

Phoenix Geophysics (2005). *Data processing User's Guide*. Phoenix Geophysics Limited, Toronto.

Rodi, W.L., Mackie, R.L. (2001). Nonlinear conjugate gradients algorithm for 2-D magnetotelluric inversion. *Journal of Geophysics*, **66**: 174-187.

Rooney, D. and Hutton, V. R. S. (1977). A magnetotelluric and magnetovariational study of the Gregory Rift Valley, Kenya. *Geophysical Journal of the Royal Astronomical Society,* **51**: (1): 91-119.

Simiyu, S.M., and Keller, G.R.(1997). Integrated geophysical analysis of the East African plateau from gravity and recent seismic studies. In: Stress and stress release in the lithosphere, Eds: Fuchs, K., Altheer, R., Muller, B.,and Prodehl, C., *Tectonophysics*,**278**: 291-314.

Simiyu, S.M., and Keller, G.R. (2001). An integrated geophysical analysis of the upper crust of the southern Kenya rift. *Geophysics Journal International*, **147**: 543-561.

Simpson, F., and Bahr, K. (2005). *Practical magnetotellurics*. Cambridge University Press, Cambridge, UK, **254**: 124-132.

Sternberg, B.K., Washburne, J.C., and Pellerin, L. (1988). Correction for the static shift in magnetotellurics using transient electromagnetic soundings. *Journal of Geophysics*, **53**: 1459-1468.

Swain, C.J.(1992). The Kenya rift axial gravity high: a reinterpretation. *Tectonophysics*, **204**: 59-70.

Swain, C.J., Khan, M.A., Wilton, T.J., Maguire, P.K.H., and Griffiths, D.H. (1981). Seismic and gravity surveys in the Lake Baringo-Tugen Hills area, Kenya rift valley. *Journal ofGeological Society of London*, **138**: 93-102.

Swain, C.J., Maguire, P.K.H. and Khan, M.A. (1994) Geophysical experiments and models of the Kenya rift before 1989.In: Crustal and Upper Mantle Structure of the Kenya Rift, eds. Prodehl, C., Keller, G.R., and Khan, M.A. *Tectonophysics*, **236**: 23-32.

Tongue, J., Maguire, P., and Burton, P. (1994). An earthquake study in the Lake Baringo basin of the central Kenya Rift. *Tectonophysics*, **236**: 151-164.

Ussher, G., Harvey, C., Johnstone, R., Anderson, E. (2000) Understanding the resistivities observed in geothermal systems. In: *proceedings world geothermal congress, Kyushu-Tohoku, Japan,* pp 1915–1920

Vozoff, K. (1991). *The magnetotelluric method*. In: Nabighiam, M.N. (Ed.), Electromagnetic methods in applied geophysics. *Society of Exploration Geophysicist,***2***: 641-712*

Wiese, H., (1962). Geomagnetische Tiefensondierung. Teil II: Die Streichrichtung der Untergrundstrukturen des elektrischen Widerstandes, erschlossen aus geomagnetischen Variationen. *Geofisica Pura et Applicata,* **52**: 83-103

Young, P.A.V., Maguire, P.K.H., Laffoley, N.d'A., and Evans, J.R. (1991). Implications of the distribution of seismicity near Lake Bogoria in the Kenya Rift. *Geophysics Journal International*, **105**: 665-674.

Zhang, P., Roberts, R.G. and Pedersen, L.B., (1987). Magnetotelluric strike rules. *Geophysics*, **52**, 267-278.

Zieke, O., and M. R. Strecker. (2009). Recurrence of large earthquakes in magmatic continental rifts: Insights from a paleoseismic study along the Laikipia–Marmanet fault, Subukia Valley, Kenya Rift, *Bulletin of Seismological Society of America*. **99**: 61-70

Zonge International Inc. (2015). *Data processing User Guide*. Zonge Limited, 3781 Tucson Arizona, USA.

APPENDICES

Appendix I: Arus Stations Coordinates

MT stations coordinates

STATION	X(m)	Y(m)	ELEVATION(m)
ARUMT2	158157.663	17705.671	1625.000
ARUMT27	161946.171	15482.358	1470.000
ARUMT29	158213.087	15618.119	1608.000
ARUMT50	178932.205	12895.050	1514.000
ARUMT51	177879.805	11810.057	1529.000
ARUMT56	166158.492	11599.058	1551.000
ARUMT58	163840.143	12048.128	1536.000
ARUMT59	161397.841	11562.625	1488.000
ARUMT60	159736.519	12059.390	1574.000
ARUMT61	158017.616	11673.634	1588.000
ARUMT62	156457.491	11836.736	1587.000
ARUMT63	154107.936	11674.023	1599.000
ARUMT64	154144.901	9672.490	1600.000
ARUMT65	156088.909	9506.307	1589.000
ARUMT66	157958.616	9613.762	1621.000
ARUMT67	160168.794	9745.781	1571.000
ARUMT69	164106.127	9662.455	1591.000
ARUMT71	167969.060	9754.372	1584.000
ARUMT93	179847.897	7844.549	1539.000
ARUSMT01	156061.929	17235.589	1581.000
ARUSMT05	164323.720	17735.499	1499.000
ARUSMT06	165902.317	17673.782	1460.000
ARUSMT08	170248.042	17802.265	1387.000
ARUSMT21	174376.651	15665.219	1430.000
ARUSMT22	172160.555	15653.204	1405.000
ARUSMT23	170647.053	15862.437	1407.000
ARUSMT24	167663.244	15635.334	1496.000
ARUSMT25	166112.584	16148.931	1443.000
ARUSMT26	164357.493	15755.658	1484.000
ARUSMT28	159893.962	15888.445	1493.000
ARUSMT3	160209.912	17425.596	1488.000
ARUSMT30	155937.851	15393.983	1577.000
ARUSMT32	154145.301	13675.548	1589.000
ARUSMT33	156092.422	13727.587	1587.000
ARUSMT34	158070.458	13705.835	1586.000
ARUSMT36	161942.853	13653.125	1471.000
ARUSMT37	163948.673	13837.354	1487.000
ARUSMT38	166161.813	13757.170	1503.000
ARUSMT39	168130.402	13784.615	1476.000

ARUSMT4	161751.514	18003.348	1474.000
ARUSMT40	170071.079	13603.022	1444.000
ARUSMT41	172268.634	13541.297	1443.000
ARUSMT54	172023.939	11792.168	1508.000
ARUSMT55	170064.683	11607.908	1483.000
ARUSMT7	168047.351	17796.437	1428.000
ARUSMT73	171918.522	9707.946	1561.000
ARUSMT74	173487.729	9440.380	1563.000
ARUSMT9	172541.569	17952.562	1364.000
ARUSMTOO	154275.823	17481.815	1591.000
SUSMT35	160438.534	14105.231	1479.000

TEM Stations Coordinates

STATION	**X(m)**	**Y(m)**	**ELEVATION(m)**
ARUS00	154275.881	17480.007	1593.000
ARUS01	156056.524	17258.110	1581.000
ARUS02	158145.812	17733.603	1613.000
ARUS03	160211.357	17448.307	1610.000
ARUS05	164342.449	17765.302	1501.000
ARUS04	161730.839	18050.598	1592.000
ARUS06	165909.414	17670.204	1596.000
ARUS09	172533.406	17987.199	1363.000
ARUS10	174062.000	17993.000	1381.000
ARUS21	174409.016	15736.533	1404.000
ARUS22	172177.277	15673.134	1403.000
ARUS23	170657.795	15895.031	1405.000
ARUS24	167666.315	15673.134	1494.000
ARUS25	166146.833	16243.726	1489.000
ARUS26	164366.191	15799.932	1486.000
ARUS27	161944.516	15514.637	1474.000
ARUS28	159878.971	15926.730	1481.000
ARUS29	158217.037	15641.435	1605.000
ARUS30	155914.073	15419.538	1584.000
ARUS32	154157.172	13707.765	1586.000
ARUS33	156104.008	13739.464	1583.000
ARUS34	158098.328	13739.464	1585.000
ARUS35	160425.035	14151.558	1478.000
ARUS36	161992.000	13644.366	1480.000
ARUS37	163915.094	13866.262	1490.000
ARUS39	168164.895	13802.863	1482.000
ARUS40	170064.248	13644.366	1581.000
ARUS41	172295.987	13549.267	1570.000
ARUS50	178967.462	12883.577	1514.000
ARUS51	177875.334	11805.794	1529.000

ARUS54	172034.826	11805.794	1468.000
ARUS55	170064.248	11647.296	1483.000
ARUS56	168048.000	11986.000	1541.000
ARUS57	166170.575	11583.897	1557.000
ARUS58	163843.869	12059.390	1536.000
ARUS59	161398.453	11583.897	1493.000
ARUS60	159736.519	12091.090	1591.000
ARUS61	158003.360	11742.395	1590.000
ARUS62	156460.137	11742.395	1537.000
ARUS63	154133.430	11710.695	1600.000
ARUS64	154133.430	9713.626	1595.000
ARUS65	156056.524	9523.429	1487.000
ARUS66	157962.174	9567.304	1621.000
ARUS67	160163.874	9777.025	1490.000
ARUS68	161987.000	9913.000	1621.000
ARUS69	164105.030	9713.626	1613.000
ARUS70	165699.151	9946.811	1593.000
ARUS71	167974.960	9777.025	1468.000
ARUS72	169885.712	9915.230	1404.000
ARUS73	171939.858	9777.025	1489.000
ARUS74	173530.566	9364.932	1591.000
ARUS92	177899.076	8065.252	1474.000
ARUS93	179869.654	7843.355	1584.000

Appendix II: Sample Arus MT static shift corrected curves using TEM

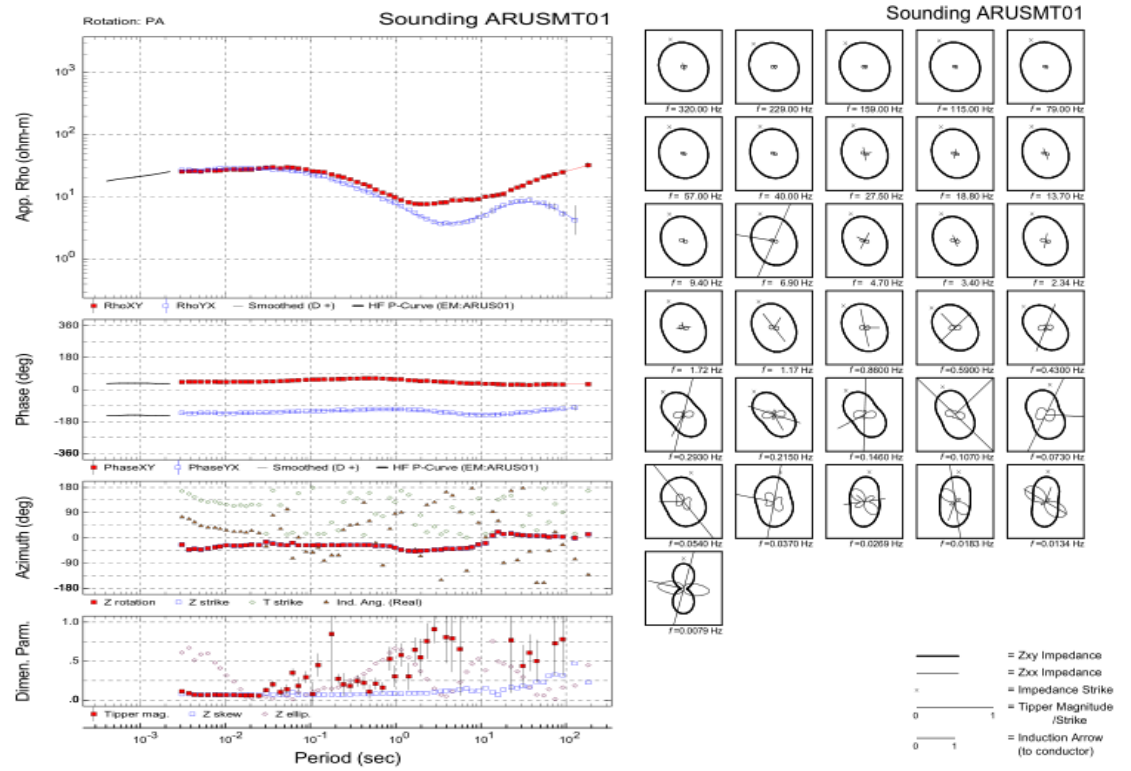

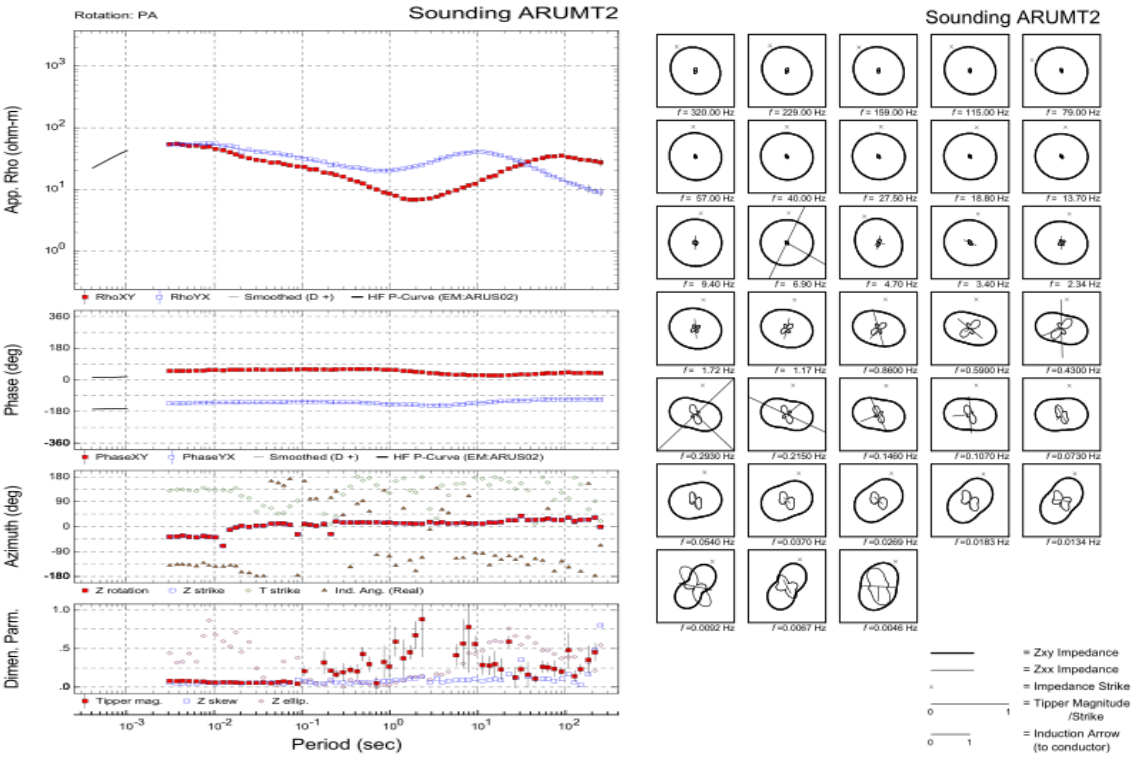

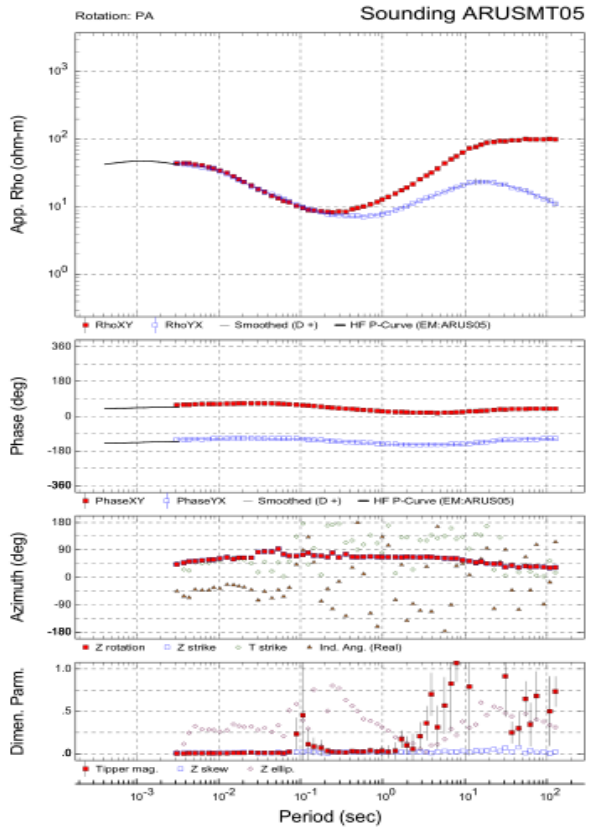
Rotation: PA
Sounding ARUSMT05
App. Rho (ohm-m)
RhoXY
RhoYX
Smoothed (D +)
HF P-Curve (EM:ARUS05)
Phase (deg)
PhaseXY
PhaseYX
Azimuth (deg)
Z rotation
Z strike
T strike
Ind. Ang. (Real)
Dimen. Parm.
Tipper mag.
Z skew
Z ellip.
Period (sec)

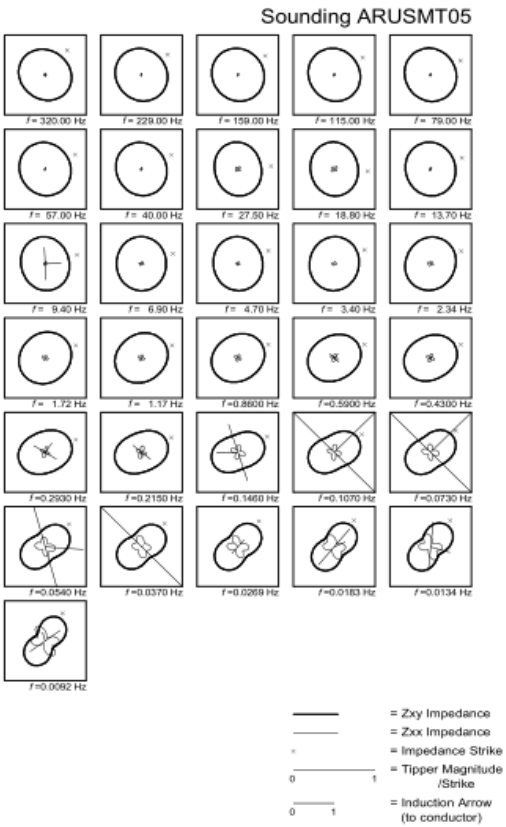
Sounding ARUSMT05
= Zxy Impedance
= Zxx Impedance
= Impedance Strike
= Tipper Magnitude /Strike
= Induction Arrow (to conductor)

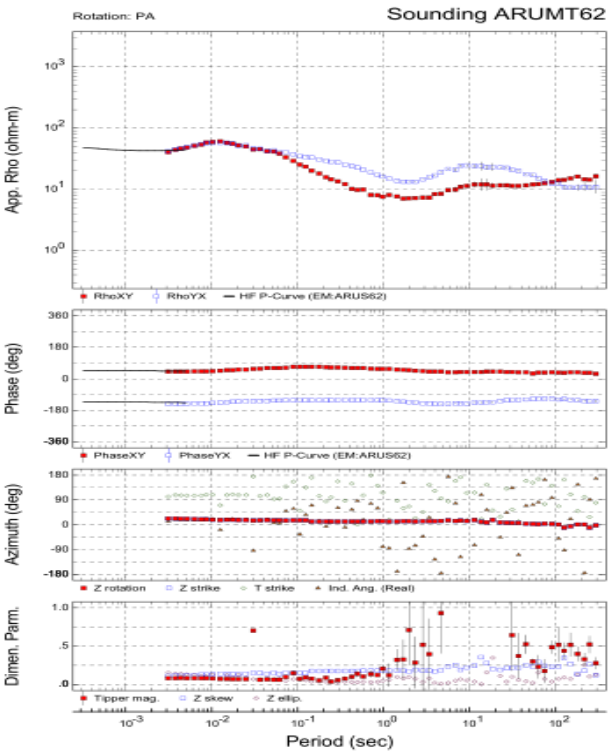
Rotation: PA
Sounding ARUMT62
App. Rho (ohm-m)
RhoXY
RhoYX
HF P-Curve (EM:ARUS62)
Phase (deg)
PhaseXY
PhaseYX
HF P-Curve (EM:ARUS62)
Azimuth (deg)
Z rotation
Z strike
T strike
Ind. Ang. (Real)
Dimen. Parm.
Tipper mag.
Z skew
Z ellip.
Period (sec)

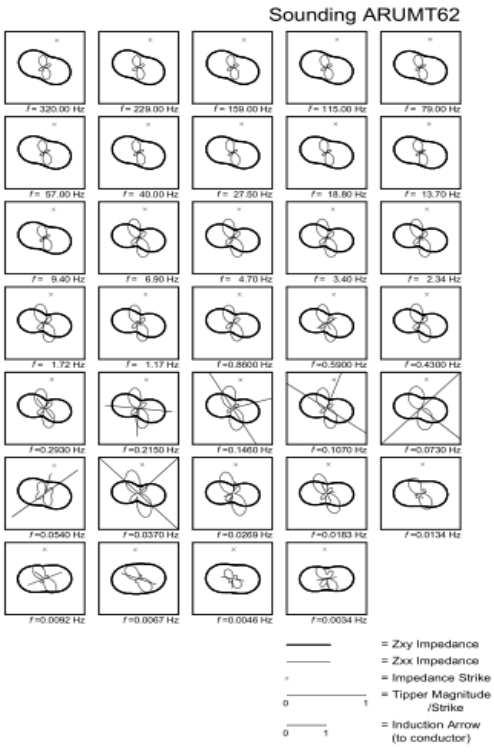
Sounding ARUMT62
= Zxy Impedance
= Zxx Impedance
= Impedance Strike
= Tipper Magnitude /Strike
= Induction Arrow (to conductor)

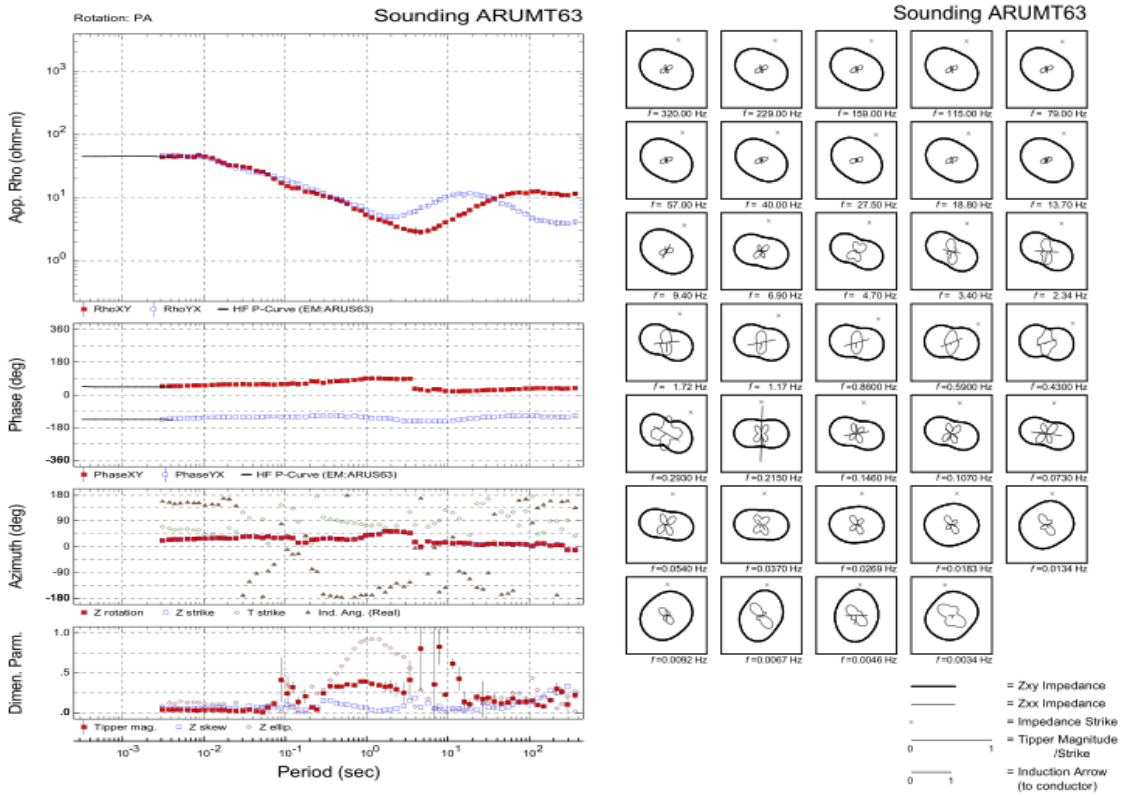
Rotation: PA
Sounding ARUMT63
App. Rho (ohm-m)
RhoXY
RhoYX
HF P-Curve (EM:ARUS63)
Phase (deg)
PhaseXY
PhaseYX
HF P-Curve (EM:ARUS63)
Azimuth (deg)
Z rotation
Z strike
T strike
Ind. Ang. (Real)
Dimen. Parm.
Tipper mag.
Z skew
Z ellip.
Period (sec)
Sounding ARUMT63
= Zxy Impedance
= Zxx Impedance
= Impedance Strike
= Tipper Magnitude /Strike
= Induction Arrow (to conductor)

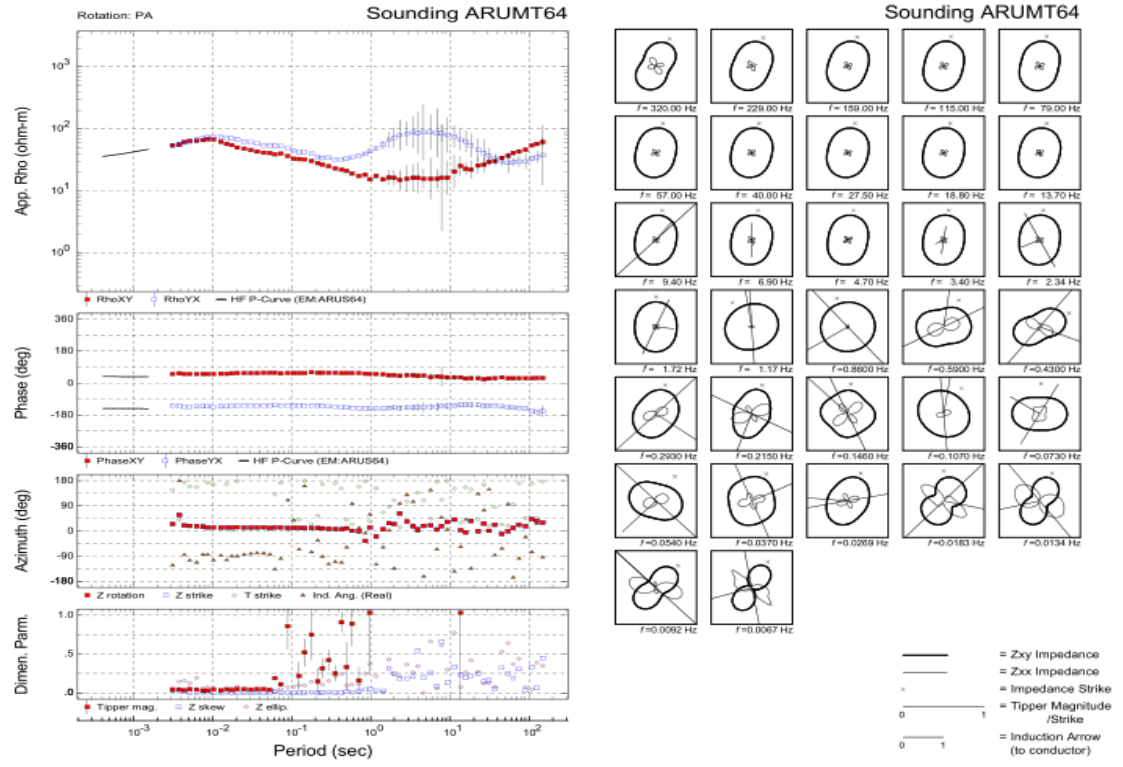
Rotation: PA
Sounding ARUMT64
App. Rho (ohm-m)
RhoXY
RhoYX
HF P-Curve (EM:ARUS64)
Phase (deg)
PhaseXY
PhaseYX
HF P-Curve (EM:ARUS64)
Azimuth (deg)
Z rotation
Z strike
T strike
Ind. Ang. (Real)
Dimen. Parm.
Tipper mag.
Z skew
Z ellip.
Period (sec)
Sounding ARUMT64
= Zxy Impedance
= Zxx Impedance
= Impedance Strike
= Tipper Magnitude /Strike
= Induction Arrow (to conductor)

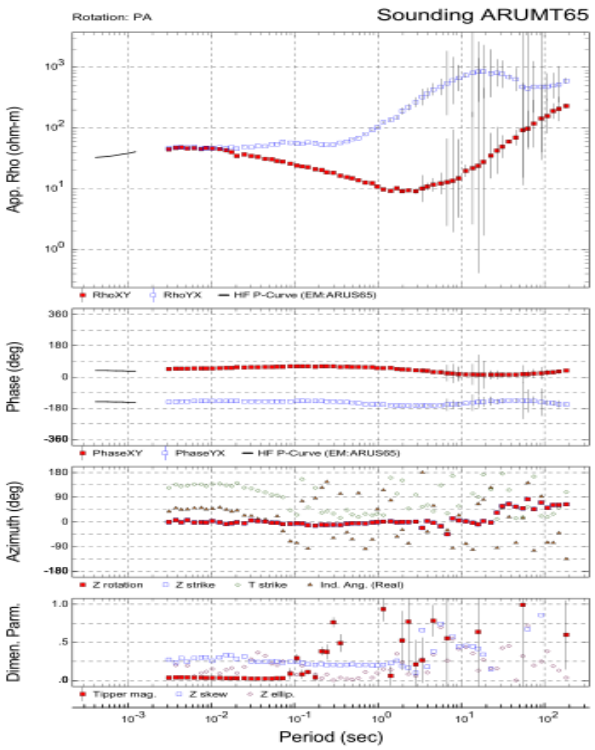
Rotation: PA
Sounding ARUMT65
App. Rho (ohm-m)
RhoXY
RhoYX
HF P-Curve (EM:ARUS65)
Phase (deg)
PhaseXY
PhaseYX
HF P-Curve (EM:ARUS65)
Azimuth (deg)
Z rotation
Z strike
T strike
Ind. Ang. (Real)
Dimen. Parm.
Tipper mag.
Z skew
Z ellip.
Period (sec)

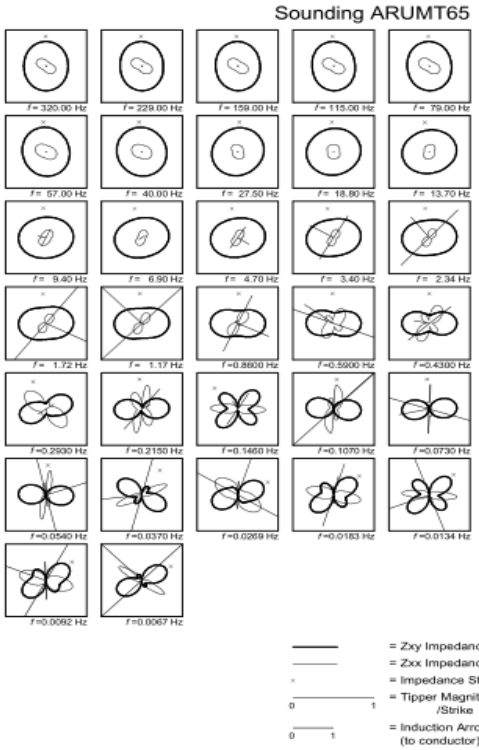
Sounding ARUMT65
f = 320.00 Hz
f = 229.00 Hz
f = 159.00 Hz
f = 115.00 Hz
f = 79.00 Hz
f = 57.00 Hz
f = 40.00 Hz
f = 27.50 Hz
f = 18.80 Hz
f = 13.70 Hz
f = 9.40 Hz
f = 6.90 Hz
f = 4.70 Hz
f = 3.40 Hz
f = 2.34 Hz
f = 1.72 Hz
f = 1.17 Hz
f =0.8600 Hz
f =0.5900 Hz
f =0.4300 Hz
f =0.2930 Hz
f =0.2150 Hz
f =0.1460 Hz
f =0.1070 Hz
f =0.0730 Hz
f =0.0540 Hz
f =0.0370 Hz
f =0.0269 Hz
f =0.0183 Hz
f =0.0134 Hz
f =0.0092 Hz
f =0.0067 Hz
= Zxy Impedance
= Zxx Impedance
= Impedance Strike
= Tipper Magnitude /Strike
= Induction Arrow (to conductor)

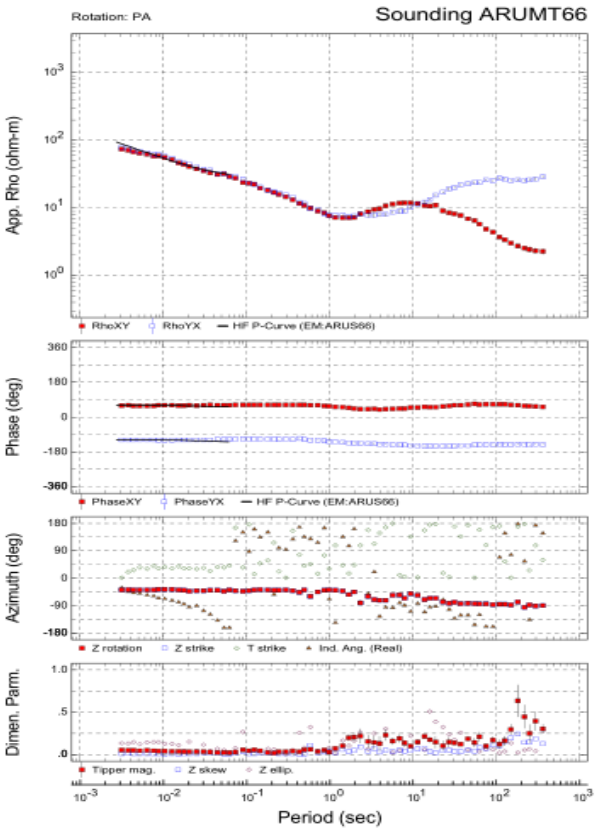
Rotation: PA
Sounding ARUMT66
App. Rho (ohm-m)
RhoXY
RhoYX
HF P-Curve (EM:ARUS66)
Phase (deg)
PhaseXY
PhaseYX
HF P-Curve (EM:ARUS66)
Azimuth (deg)
Z rotation
Z strike
T strike
Ind. Ang. (Real)
Dimen. Parm.
Tipper mag.
Z skew
Z ellip.
Period (sec)

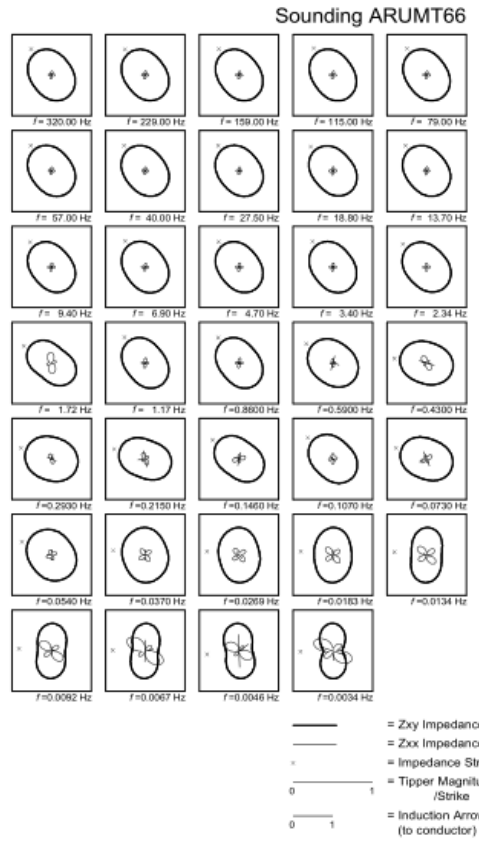
Sounding ARUMT66
f = 320.00 Hz
f = 229.00 Hz
f = 159.00 Hz
f = 115.00 Hz
f = 79.00 Hz
f = 57.00 Hz
f = 40.00 Hz
f = 27.50 Hz
f = 18.80 Hz
f = 13.70 Hz
f = 9.40 Hz
f = 6.90 Hz
f = 4.70 Hz
f = 3.40 Hz
f = 2.34 Hz
f = 1.72 Hz
f = 1.17 Hz
f =0.8600 Hz
f =0.5900 Hz
f =0.4300 Hz
f =0.2930 Hz
f =0.2150 Hz
f =0.1460 Hz
f =0.1070 Hz
f =0.0730 Hz
f =0.0540 Hz
f =0.0370 Hz
f =0.0269 Hz
f =0.0183 Hz
f =0.0134 Hz
f =0.0092 Hz
f =0.0067 Hz
f =0.0046 Hz
f =0.0034 Hz
= Zxy Impedance
= Zxx Impedance
= Impedance Strike
= Tipper Magnitude /Strike
= Induction Arrow (to conductor)

Appendix III: MT 1D Models

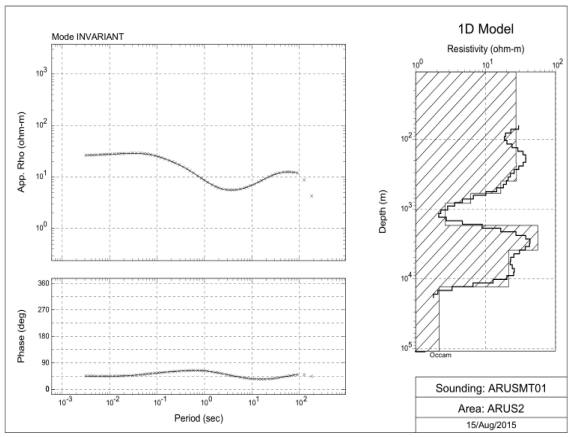

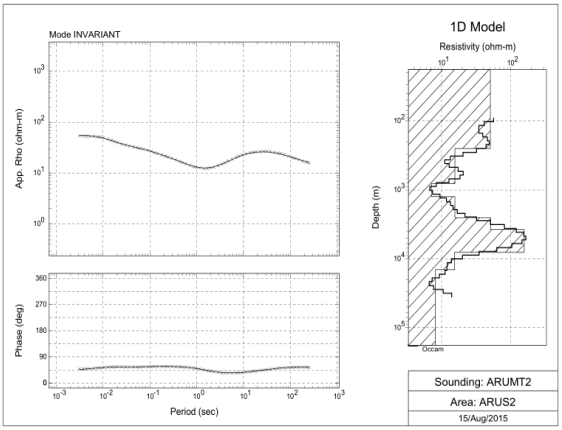

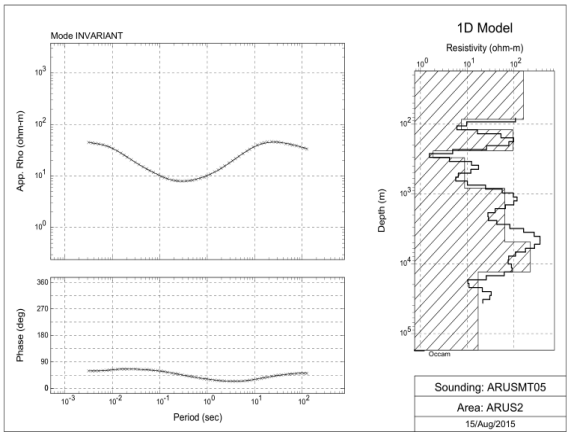

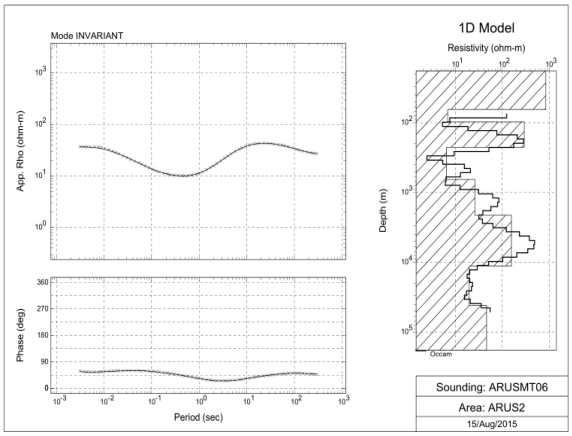

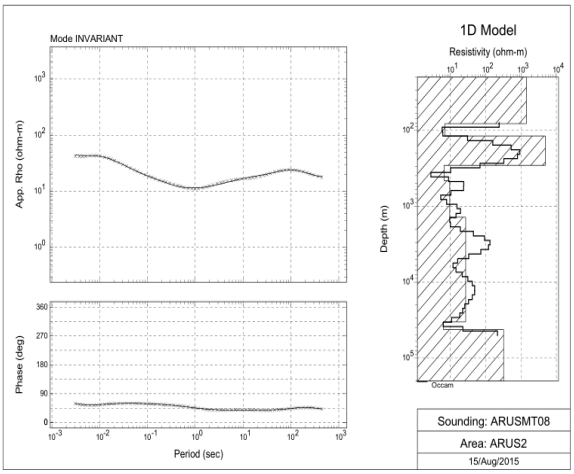

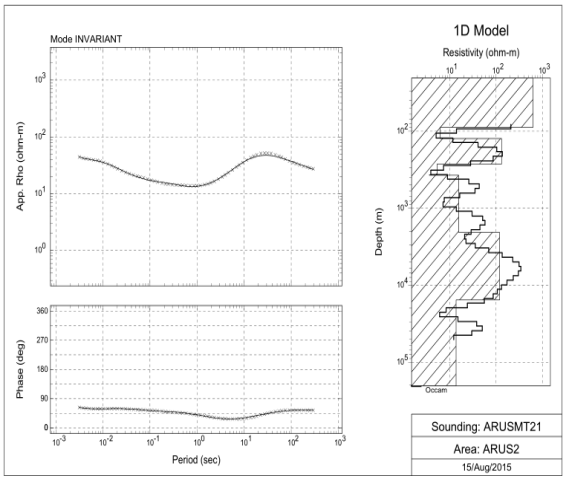

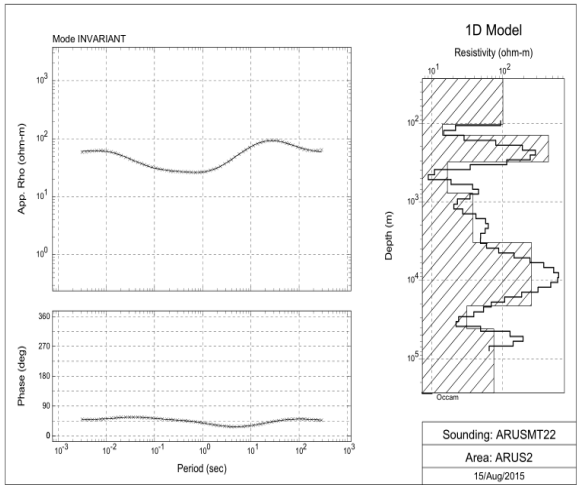
Mode INVARIANT
App. Rho (ohm-m)
Phase (deg)
Period (sec)
1D Model
Resistivity (ohm-m)
Depth (m)
Occam
Sounding: ARUSMT22
Area: ARUS2
15/Aug/2015

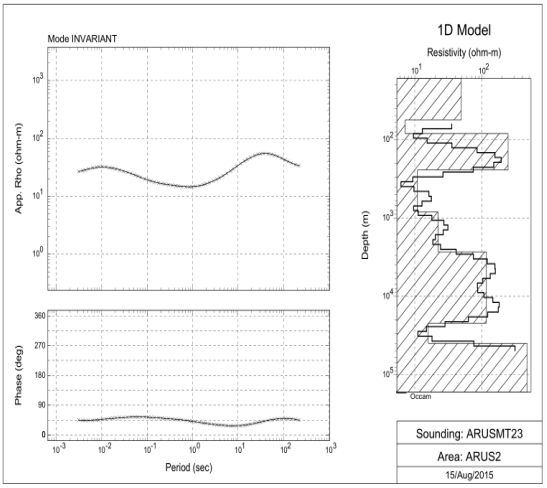
Mode INVARIANT
App. Rho (ohm-m)
Phase (deg)
Period (sec)
1D Model
Resistivity (ohm-m)
Depth (m)
Occam
Sounding: ARUSMT23
Area: ARUS2
15/Aug/2015

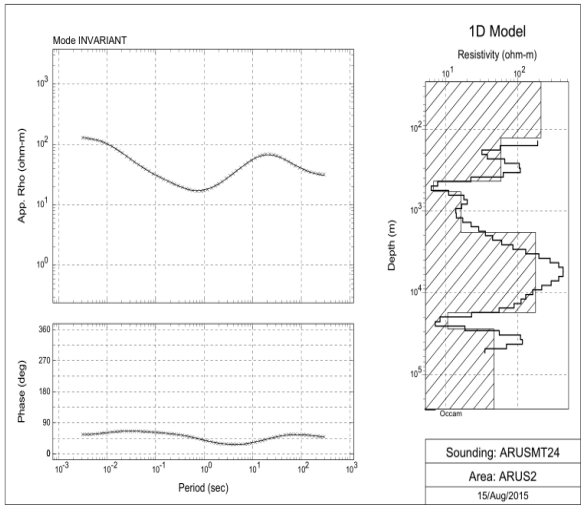
Mode INVARIANT
App. Rho (ohm-m)
Phase (deg)
Period (sec)
1D Model
Resistivity (ohm-m)
Depth (m)
Occam
Sounding: ARUSMT24
Area: ARUS2
15/Aug/2015

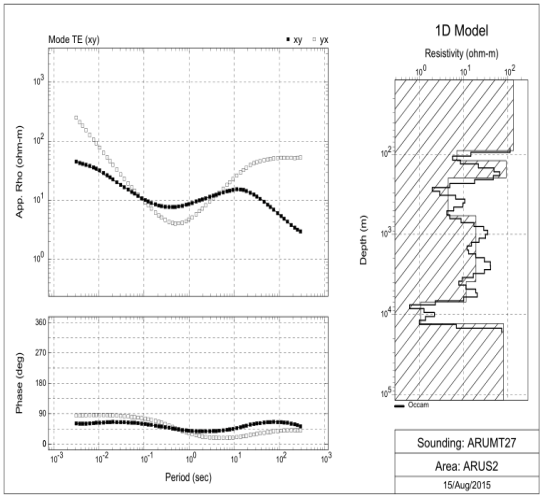
Mode TE (xy)
xy
yx
App. Rho (ohm-m)
Phase (deg)
Period (sec)
1D Model
Resistivity (ohm-m)
Depth (m)
Occam
Sounding: ARUMT27
Area: ARUS2
15/Aug/2015

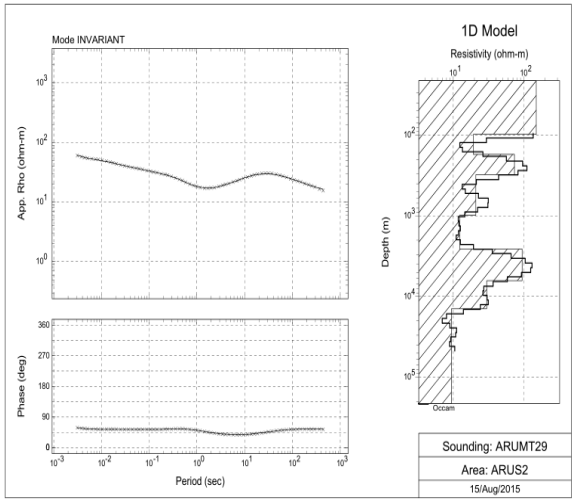
Mode INVARIANT
App. Rho (ohm-m)
Phase (deg)
Period (sec)
1D Model
Resistivity (ohm-m)
Depth (m)
Occam
Sounding: ARUMT29
Area: ARUS2
15/Aug/2015

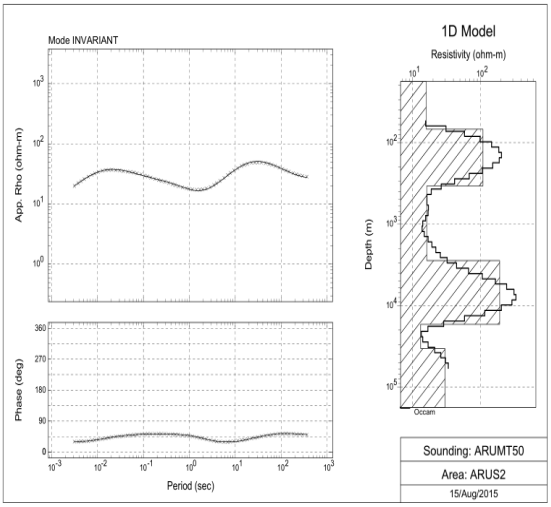
Mode INVARIANT
App. Rho (ohm-m)
Phase (deg)
Period (sec)
1D Model
Resistivity (ohm-m)
Depth (m)
Occam
Sounding: ARUMT50
Area: ARUS2
15/Aug/2015

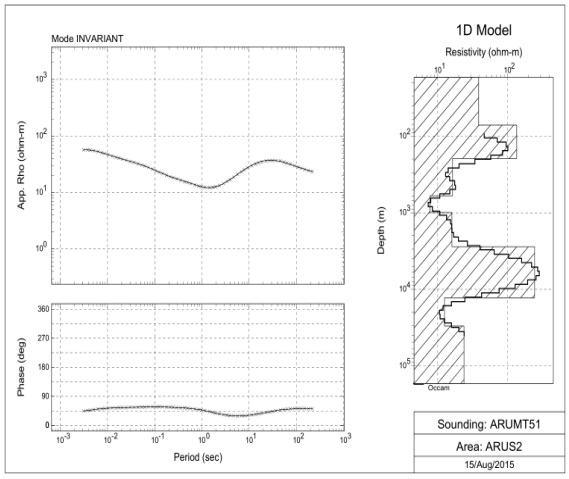
Mode INVARIANT
App. Rho (ohm-m)
Phase (deg)
Period (sec)
1D Model
Resistivity (ohm-m)
Depth (m)
Occam
Sounding: ARUMT51
Area: ARUS2
15/Aug/2015

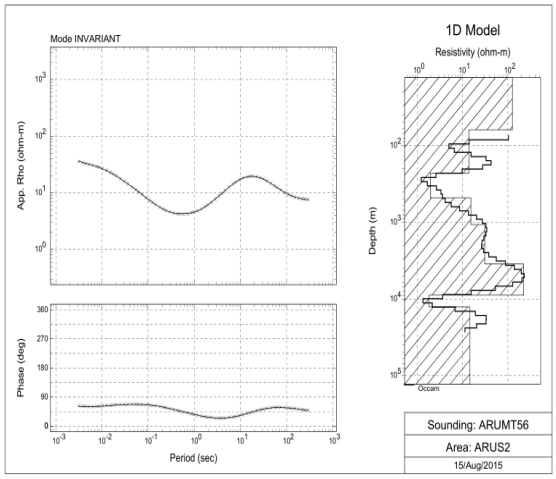
Mode INVARIANT
App. Rho (ohm-m)
Phase (deg)
Period (sec)
1D Model
Resistivity (ohm-m)
Depth (m)
Occam
Sounding: ARUMT56
Area: ARUS2
15/Aug/2015

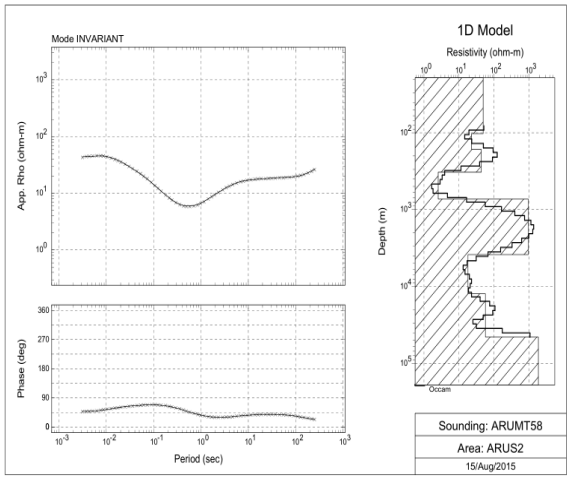
Mode INVARIANT
App. Rho (ohm-m)
Phase (deg)
Period (sec)
1D Model
Resistivity (ohm-m)
Depth (m)
Occam
Sounding: ARUMT58
Area: ARUS2
15/Aug/2015

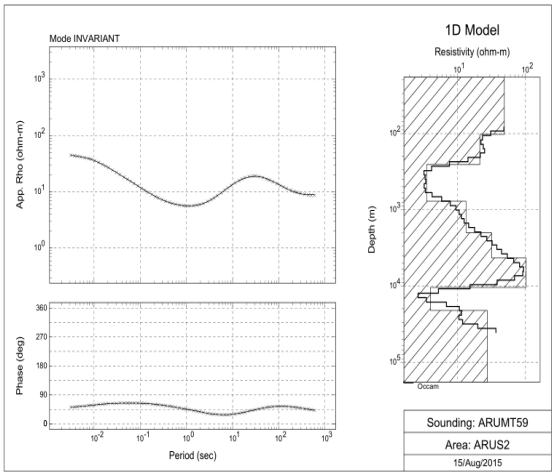
Mode INVARIANT
App. Rho (ohm-m)
Phase (deg)
Period (sec)
1D Model
Resistivity (ohm-m)
Depth (m)
Occam
Sounding: ARUMT59
Area: ARUS2
15/Aug/2015

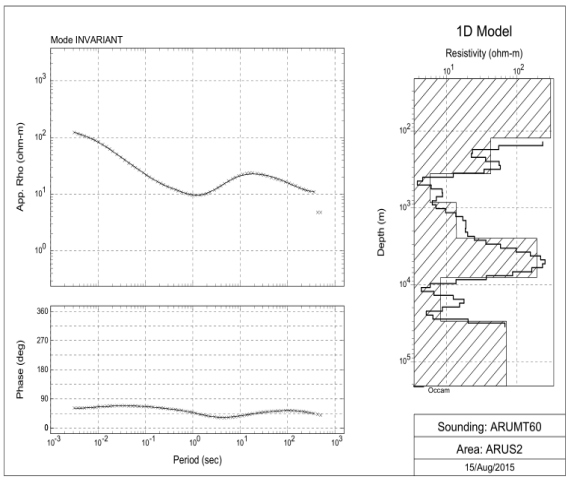
Mode INVARIANT
App. Rho (ohm-m)
Phase (deg)
Period (sec)
1D Model
Resistivity (ohm-m)
Depth (m)
Occam
Sounding: ARUMT60
Area: ARUS2
15/Aug/2015

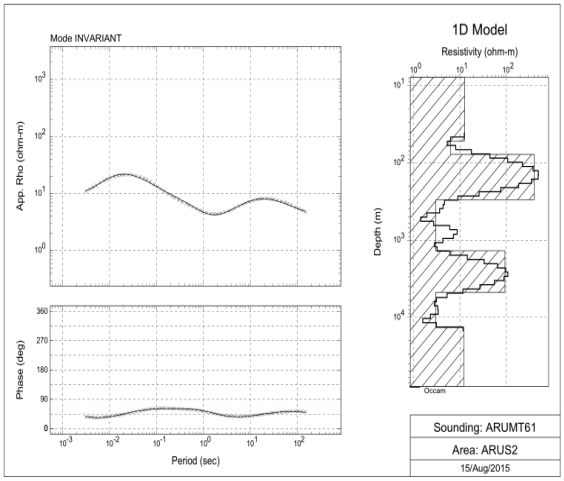
Mode INVARIANT
App. Rho (ohm-m)
Phase (deg)
Period (sec)
1D Model
Resistivity (ohm-m)
Depth (m)
Occam
Sounding: ARUMT61
Area: ARUS2
15/Aug/2015

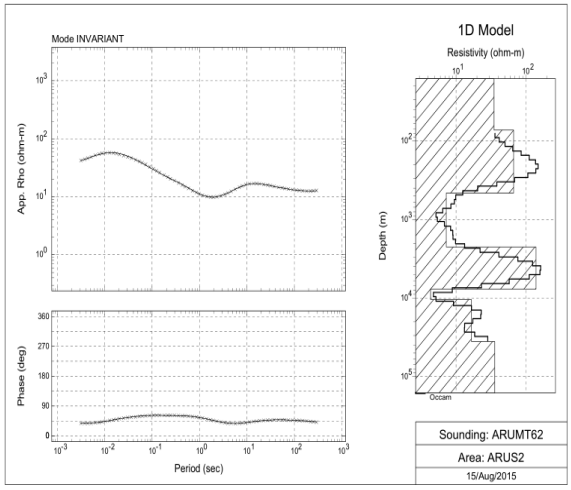
Mode INVARIANT
App. Rho (ohm-m)
Phase (deg)
Period (sec)
1D Model
Resistivity (ohm-m)
Depth (m)
Occam
Sounding: ARUMT62
Area: ARUS2
15/Aug/2015

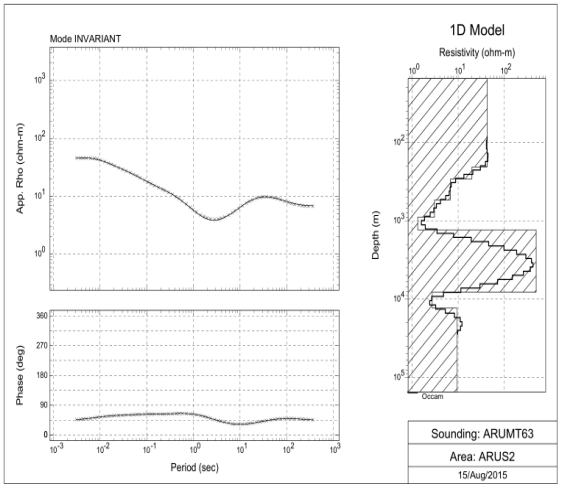
Mode INVARIANT
App. Rho (ohm-m)
Phase (deg)
Period (sec)
1D Model
Resistivity (ohm-m)
Depth (m)
Occam
Sounding: ARUMT63
Area: ARUS2
15/Aug/2015

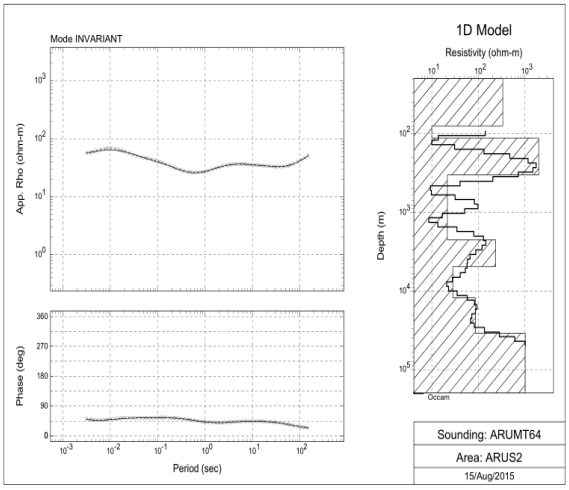
Mode INVARIANT
App. Rho (ohm-m)
Phase (deg)
Period (sec)
1D Model
Resistivity (ohm-m)
Depth (m)
Occam
Sounding: ARUMT64
Area: ARUS2
15/Aug/2015

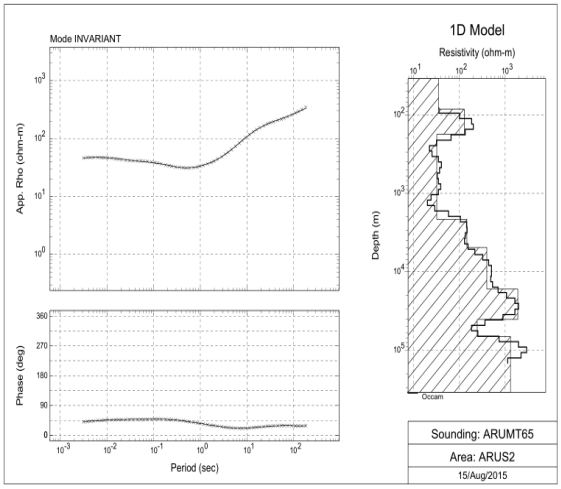
Mode INVARIANT
App. Rho (ohm-m)
Phase (deg)
Period (sec)
1D Model
Resistivity (ohm-m)
Depth (m)
Occam
Sounding: ARUMT65
Area: ARUS2
15/Aug/2015

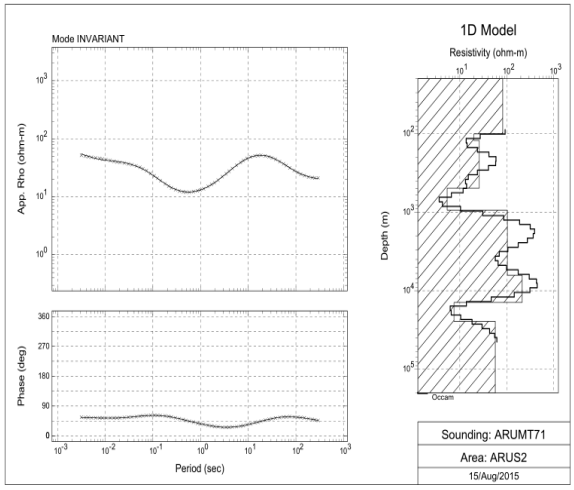
Mode INVARIANT
App. Rho (ohm-m)
Phase (deg)
Period (sec)
1D Model
Resistivity (ohm-m)
Depth (m)
Occam
Sounding: ARUMT71
Area: ARUS2
15/Aug/2015

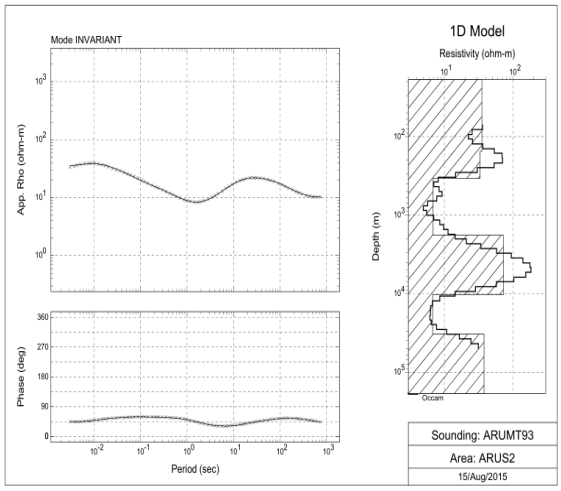
Mode INVARIANT
App. Rho (ohm-m)
Phase (deg)
Period (sec)
1D Model
Resistivity (ohm-m)
Depth (m)
Occam
Sounding: ARUMT93
Area: ARUS2
15/Aug/2015

Appendix IV: TEM 1D inversion models

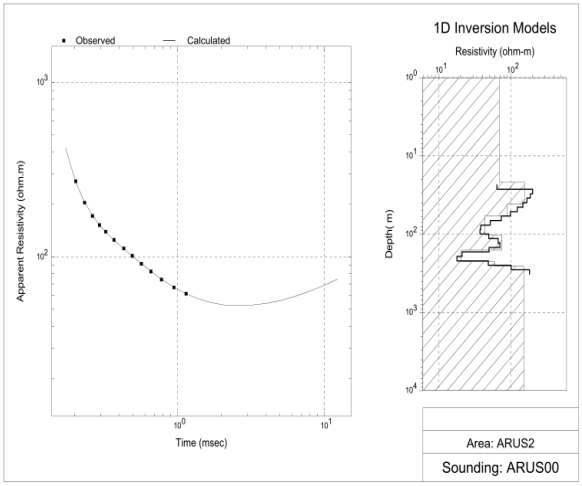

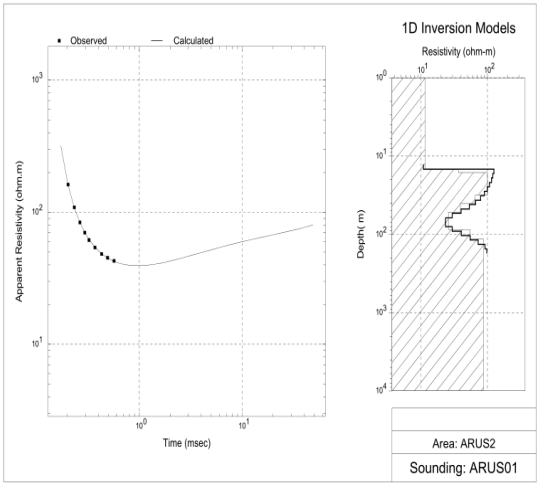

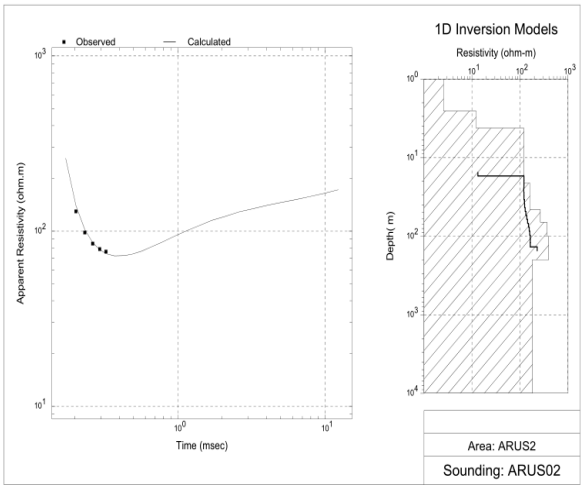

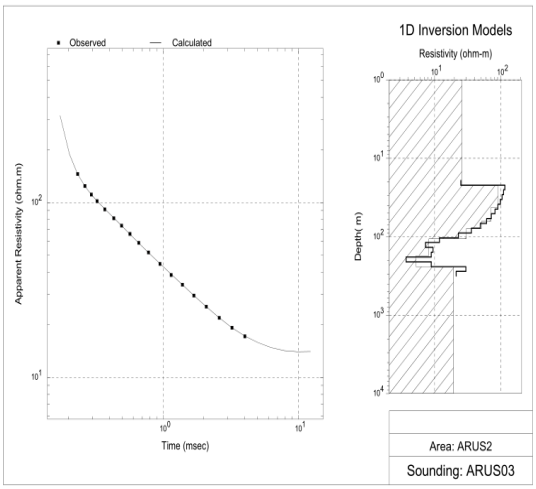

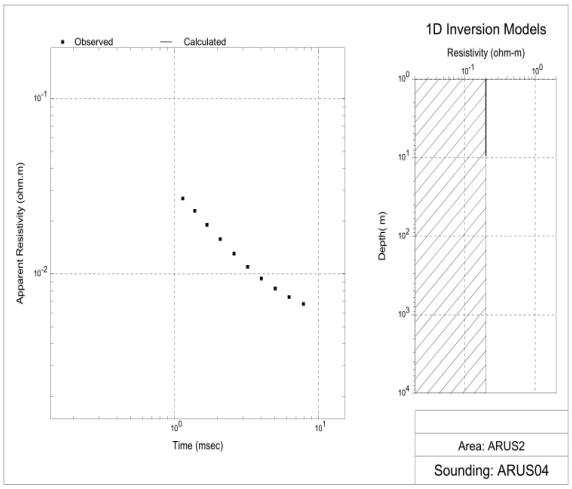

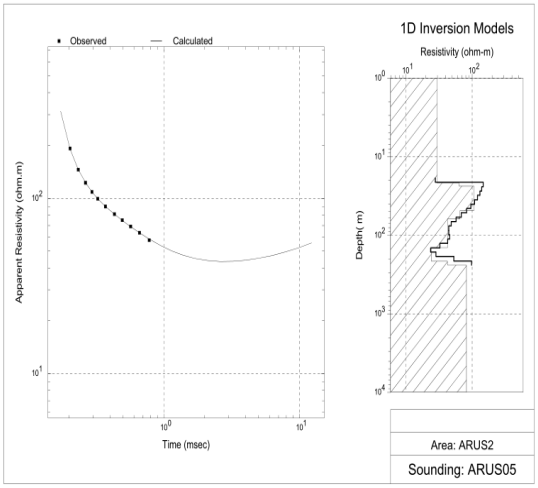

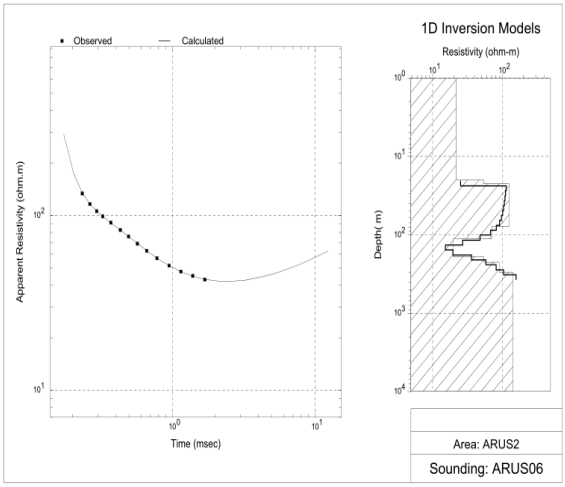
1D Inversion Models
Observed
Calculated
Apparent Resistivity (ohm.m)
Time (msec)
Resistivity (ohm-m)
Depth(m)
Area: ARUS2
Sounding: ARUS06

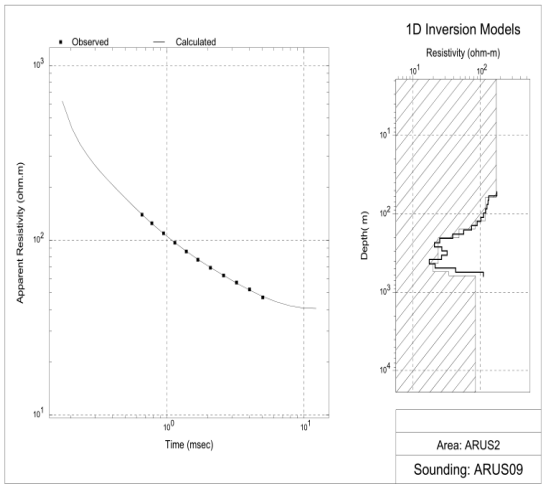
1D Inversion Models
Observed
Calculated
Apparent Resistivity (ohm.m)
Time (msec)
Resistivity (ohm-m)
Depth(m)
Area: ARUS2
Sounding: ARUS09

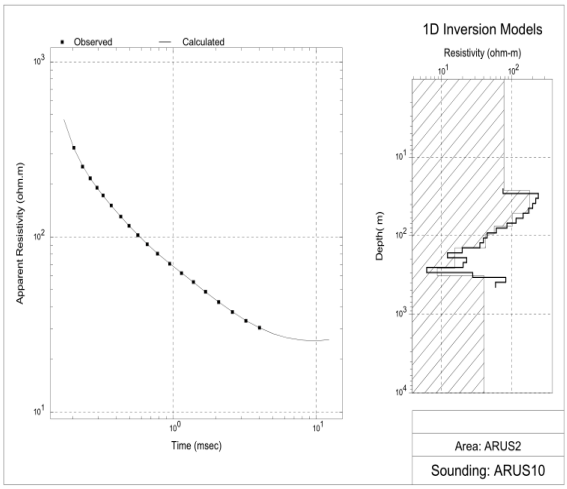
1D Inversion Models
Observed
Calculated
Apparent Resistivity (ohm.m)
Time (msec)
Resistivity (ohm-m)
Depth(m)
Area: ARUS2
Sounding: ARUS10

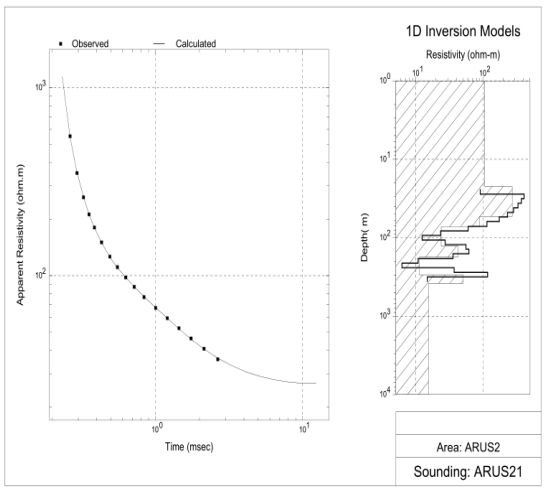
1D Inversion Models
Observed
Calculated
Apparent Resistivity (ohm.m)
Time (msec)
Resistivity (ohm-m)
Depth(m)
Area: ARUS2
Sounding: ARUS21

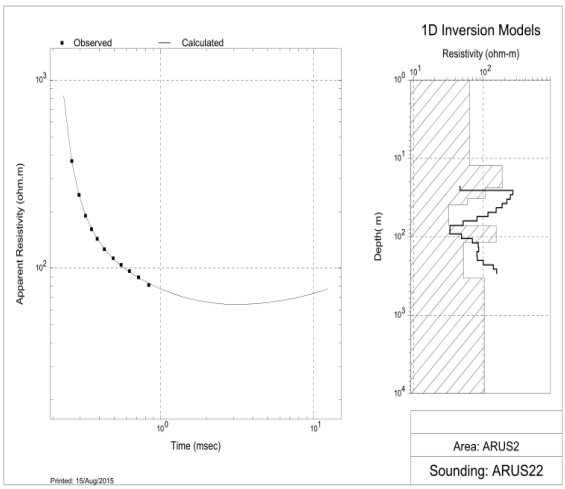
1D Inversion Models
Observed
Calculated
Apparent Resistivity (ohm.m)
Time (msec)
Resistivity (ohm-m)
Depth(m)
Area: ARUS2
Sounding: ARUS22
Printed: 15/Aug/2015

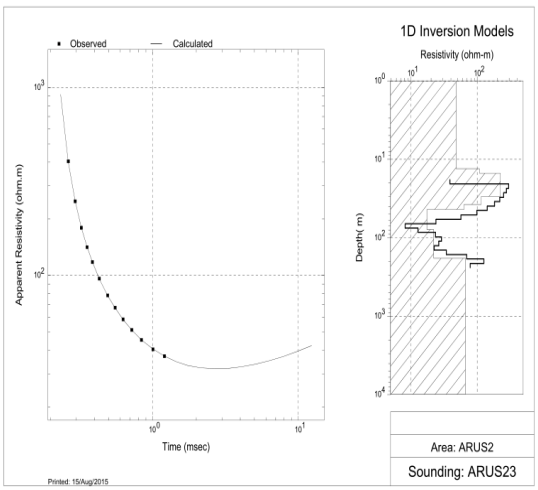
1D Inversion Models
Observed
Calculated
Apparent Resistivity (ohm.m)
Time (msec)
Resistivity (ohm-m)
Depth(m)
Area: ARUS2
Sounding: ARUS23
Printed: 15/Aug/2015

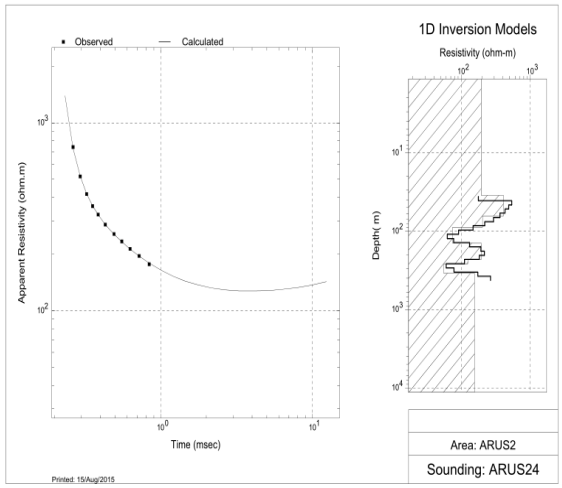
Observed
Calculated
Apparent Resistivity (ohm.m)
Time (msec)
1D Inversion Models
Resistivity (ohm-m)
Depth(m)
Area: ARUS2
Sounding: ARUS24
Printed: 15/Aug/2015

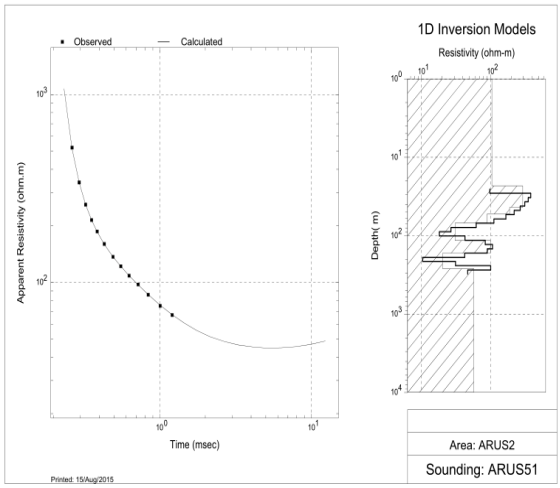
Observed
Calculated
Apparent Resistivity (ohm.m)
Time (msec)
1D Inversion Models
Resistivity (ohm-m)
Depth(m)
Area: ARUS2
Sounding: ARUS51
Printed: 15/Aug/2015

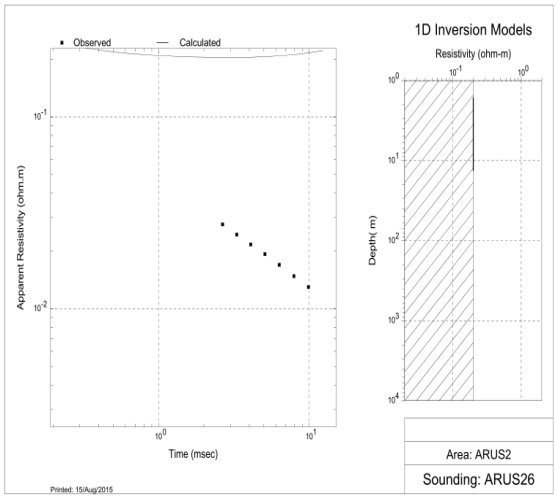
Observed
Calculated
Apparent Resistivity (ohm.m)
Time (msec)
1D Inversion Models
Resistivity (ohm-m)
Depth(m)
Area: ARUS2
Sounding: ARUS26
Printed: 15/Aug/2015

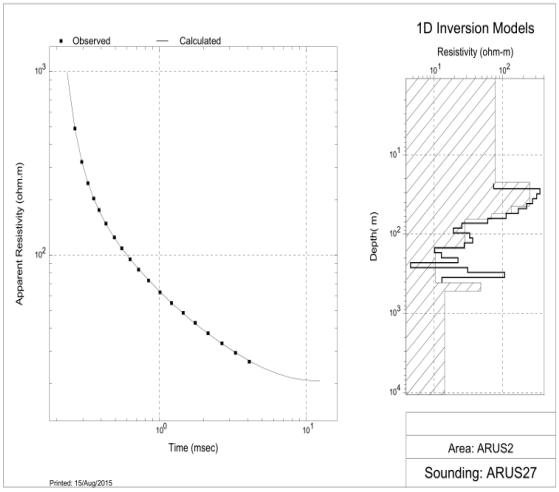
Observed
Calculated
Apparent Resistivity (ohm.m)
Time (msec)
1D Inversion Models
Resistivity (ohm-m)
Depth(m)
Area: ARUS2
Sounding: ARUS27
Printed: 15/Aug/2015

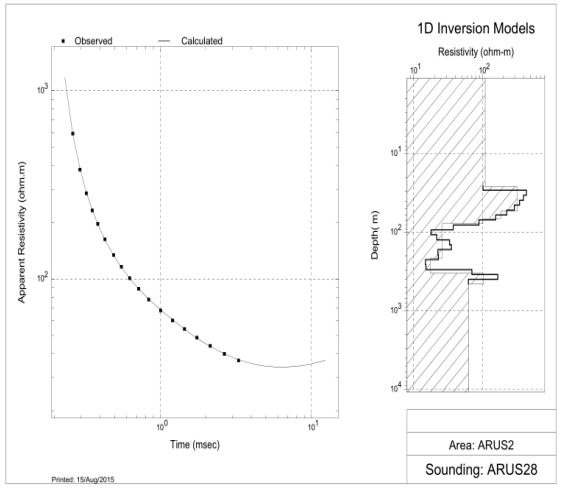
Observed
Calculated
Apparent Resistivity (ohm.m)
Time (msec)
1D Inversion Models
Resistivity (ohm-m)
Depth(m)
Area: ARUS2
Sounding: ARUS28
Printed: 15/Aug/2015

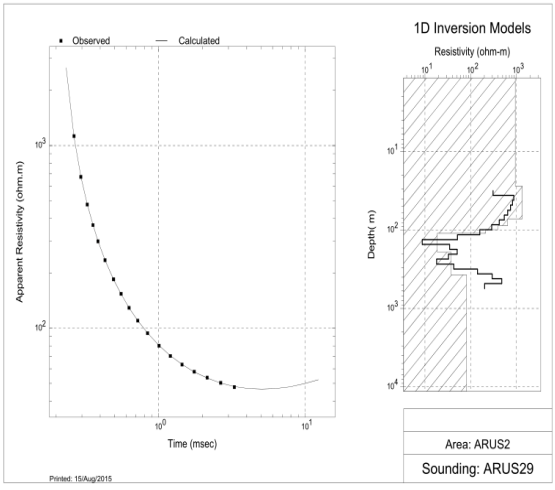
Observed
Calculated
Apparent Resistivity (ohm.m)
Time (msec)
1D Inversion Models
Resistivity (ohm-m)
Depth(m)
Area: ARUS2
Sounding: ARUS29
Printed: 15/Aug/2015

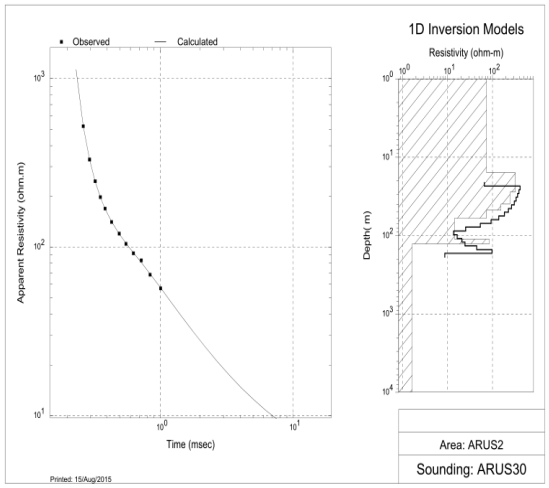
Observed
Calculated
Apparent Resistivity (ohm.m)
Time (msec)
1D Inversion Models
Resistivity (ohm-m)
Depth(m)
Area: ARUS2
Sounding: ARUS30
Printed: 15/Aug/2015

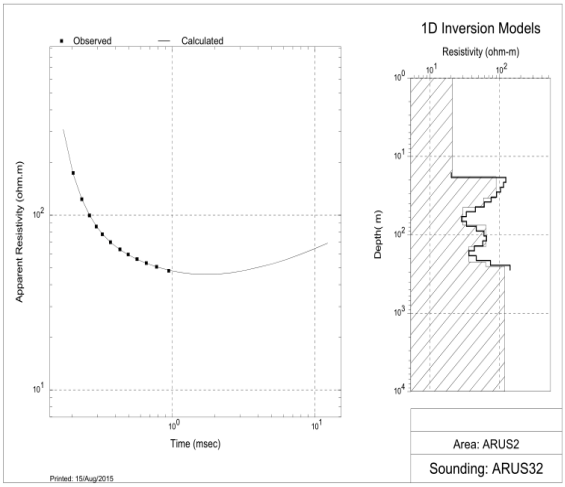
Observed
Calculated
Apparent Resistivity (ohm.m)
Time (msec)
1D Inversion Models
Resistivity (ohm-m)
Depth(m)
Area: ARUS2
Sounding: ARUS32
Printed: 15/Aug/2015

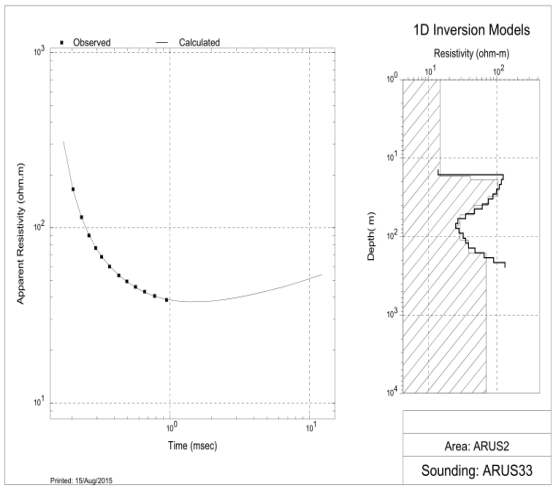
Observed
Calculated
Apparent Resistivity (ohm.m)
Time (msec)
1D Inversion Models
Resistivity (ohm-m)
Depth(m)
Area: ARUS2
Sounding: ARUS33
Printed: 15/Aug/2015

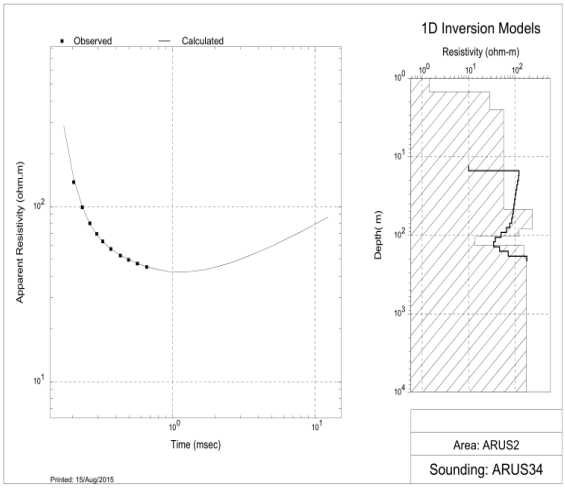
Observed
Calculated
Apparent Resistivity (ohm.m)
Time (msec)
1D Inversion Models
Resistivity (ohm-m)
Depth(m)
Area: ARUS2
Sounding: ARUS34
Printed: 15/Aug/2015

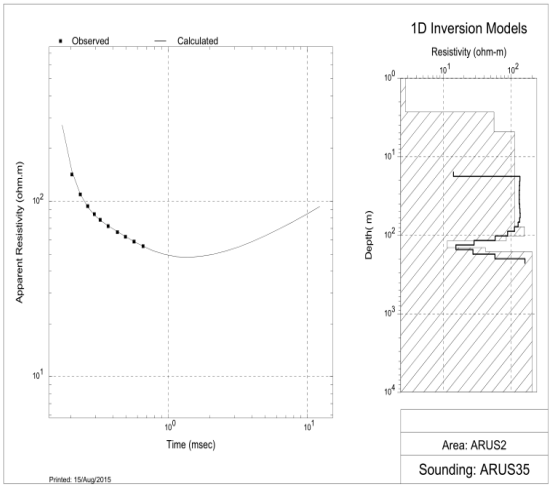
Observed
Calculated
Apparent Resistivity (ohm.m)
Time (msec)
1D Inversion Models
Resistivity (ohm-m)
Depth(m)
Area: ARUS2
Sounding: ARUS35
Printed: 15/Aug/2015

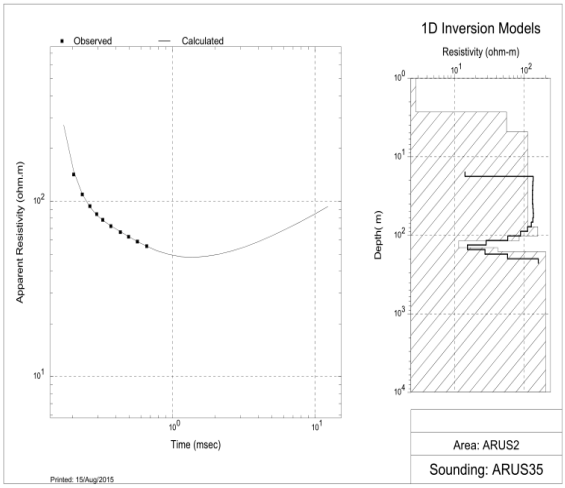
Observed
Calculated
Apparent Resistivity (ohm.m)
Time (msec)
1D Inversion Models
Resistivity (ohm-m)
Depth(m)
Area: ARUS2
Sounding: ARUS35
Printed: 15/Aug/2015

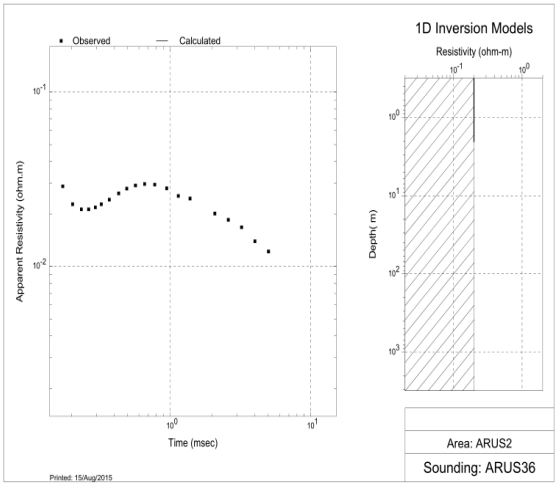
Observed
Calculated
Apparent Resistivity (ohm.m)
Time (msec)
1D Inversion Models
Resistivity (ohm-m)
Depth(m)
Area: ARUS2
Sounding: ARUS36
Printed: 15/Aug/2015

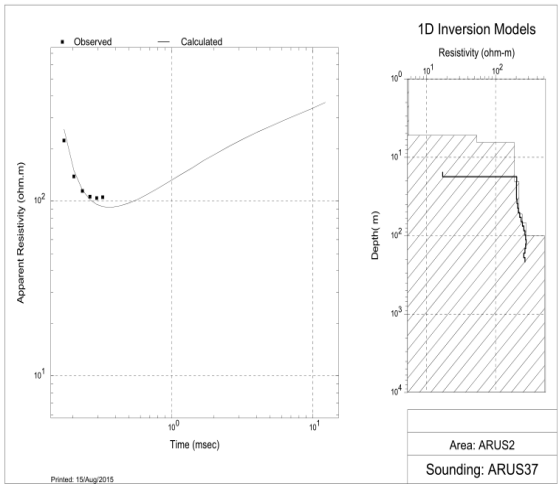
Observed
Calculated
Apparent Resistivity (ohm.m)
Time (msec)
1D Inversion Models
Resistivity (ohm-m)
Depth(m)
Area: ARUS2
Sounding: ARUS37
Printed: 15/Aug/2015

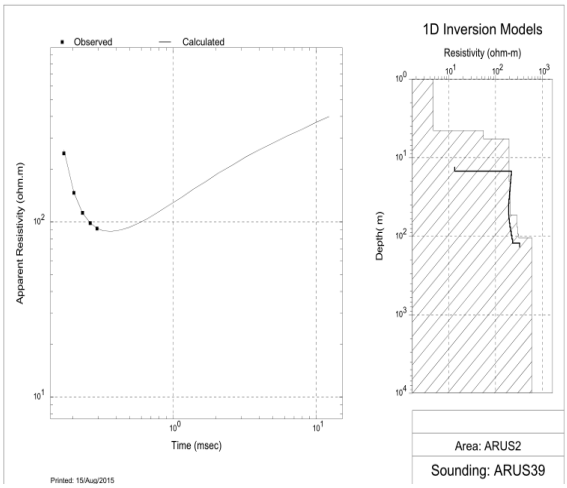
Observed
Calculated
Apparent Resistivity (ohm.m)
Time (msec)
1D Inversion Models
Resistivity (ohm-m)
Depth(m)
Area: ARUS2
Sounding: ARUS39
Printed: 15/Aug/2015

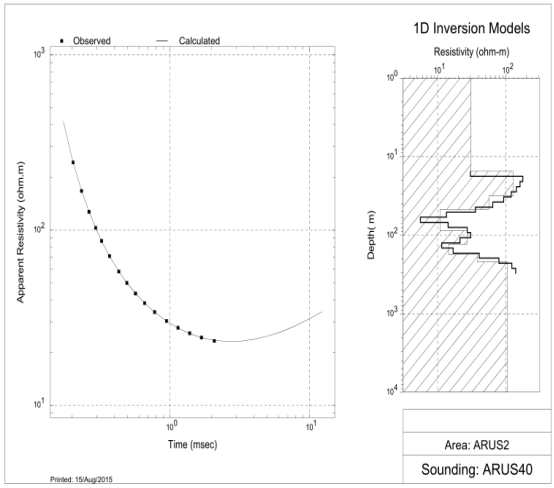
Observed
Calculated
Apparent Resistivity (ohm.m)
Time (msec)
1D Inversion Models
Resistivity (ohm-m)
Depth(m)
Area: ARUS2
Sounding: ARUS40
Printed: 15/Aug/2015

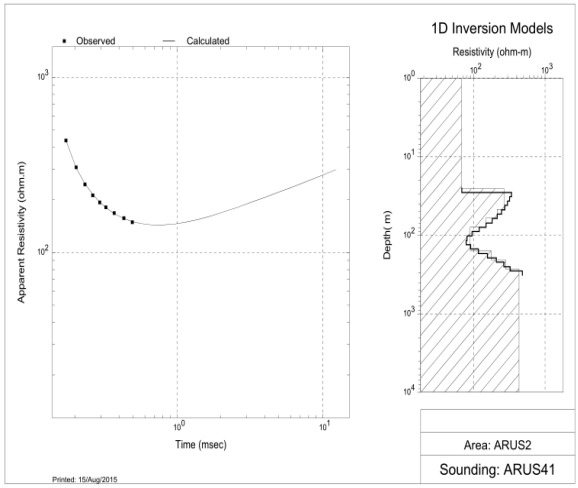
Observed
Calculated
Apparent Resistivity (ohm.m)
Time (msec)
1D Inversion Models
Resistivity (ohm-m)
Depth(m)
Area: ARUS2
Sounding: ARUS41
Printed: 15/Aug/2015

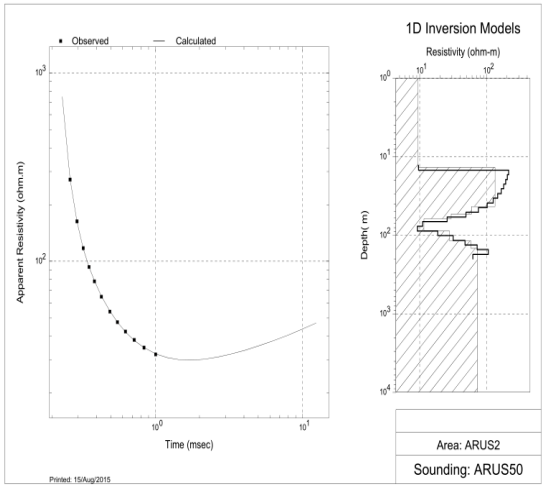
Observed
Calculated
Apparent Resistivity (ohm.m)
Time (msec)
1D Inversion Models
Resistivity (ohm-m)
Depth(m)
Area: ARUS2
Sounding: ARUS50
Printed: 15/Aug/2015

Appendix V: Cross-sections

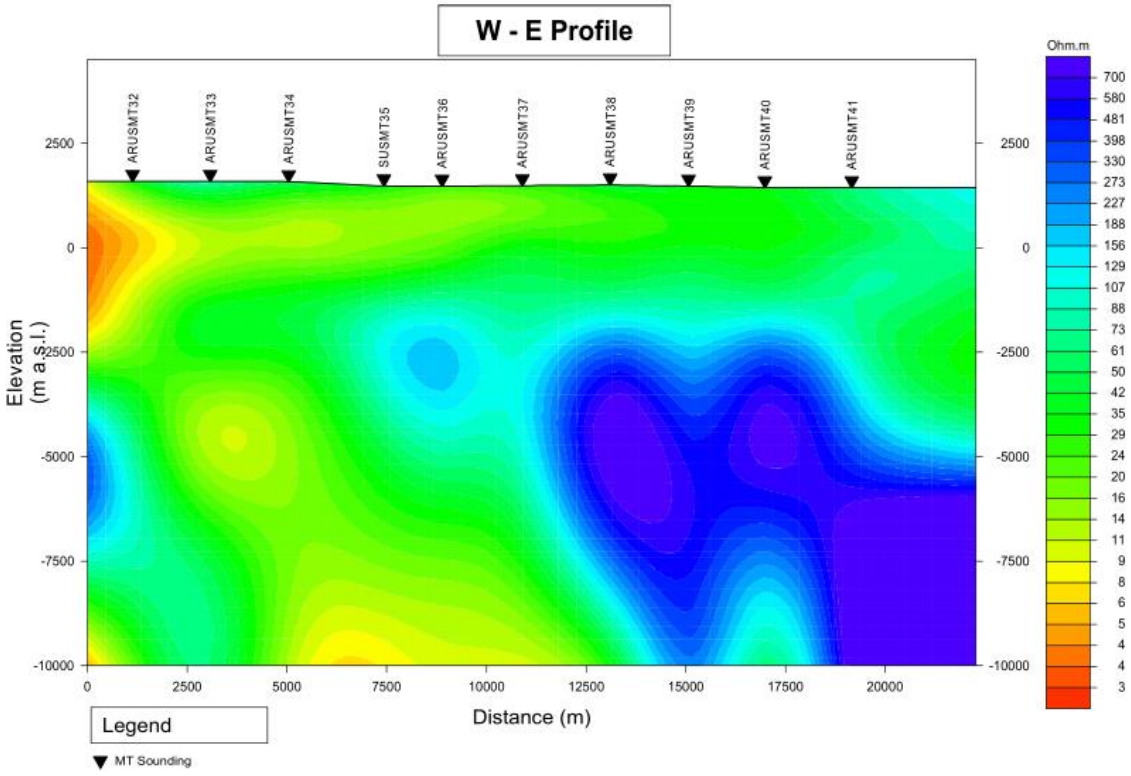

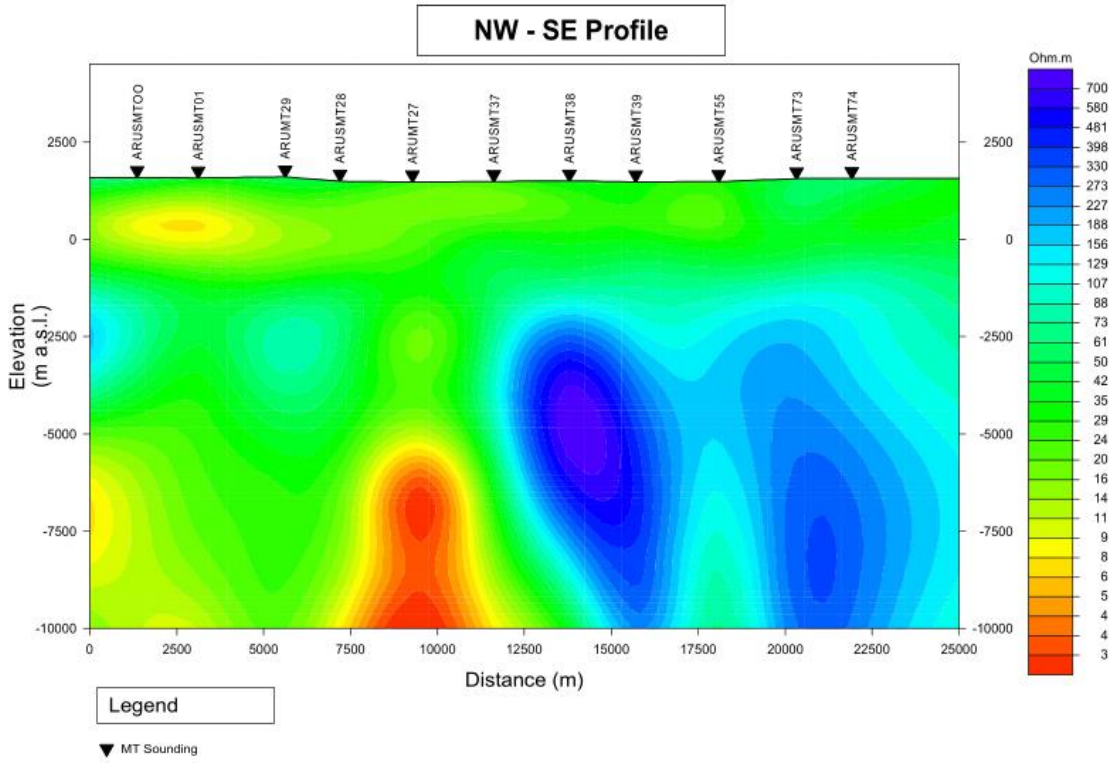

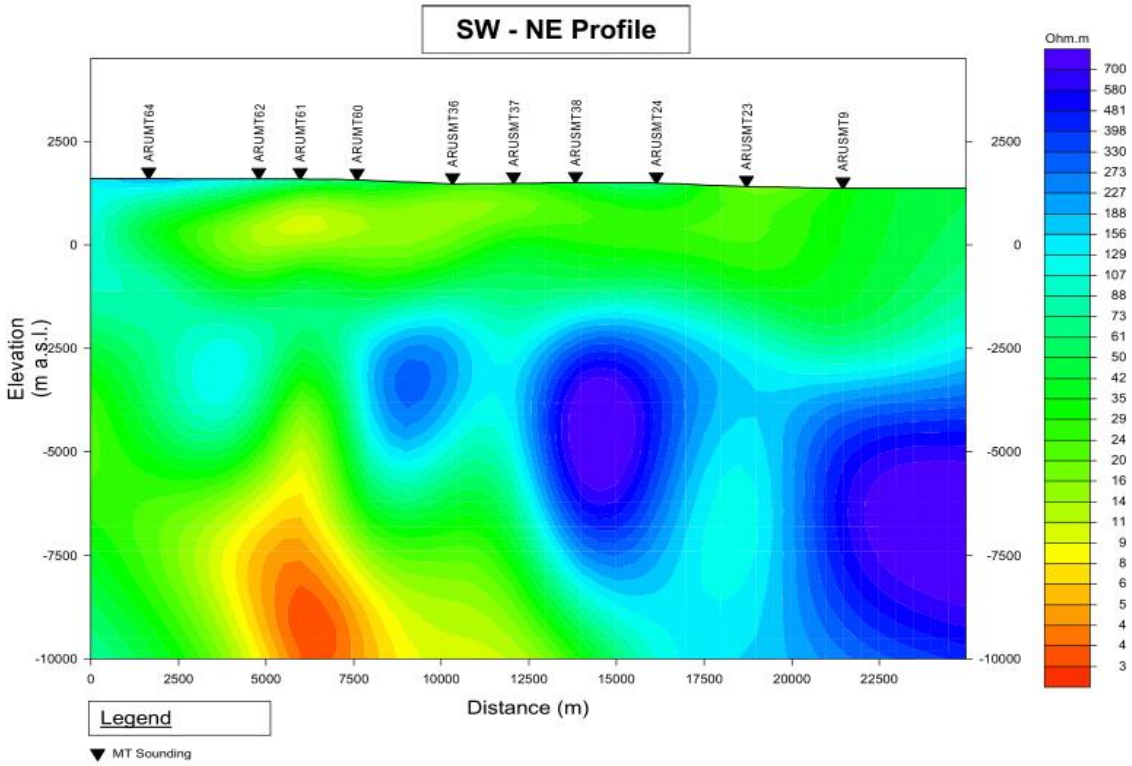
SW - NE Profile
ARUMT64
ARUMT62
ARUMT61
ARUMT60
ARUSMT36
ARUSMT37
ARUSMT38
ARUSMT24
ARUSMT23
ARUSMT9
Elevation (m a.s.l.)
Distance (m)
Ohm.m
700
580
481
398
330
273
227
188
156
129
107
88
73
61
50
42
35
29
24
20
16
14
11
9
8
6
5
4
4
3
Legend
MT Sounding

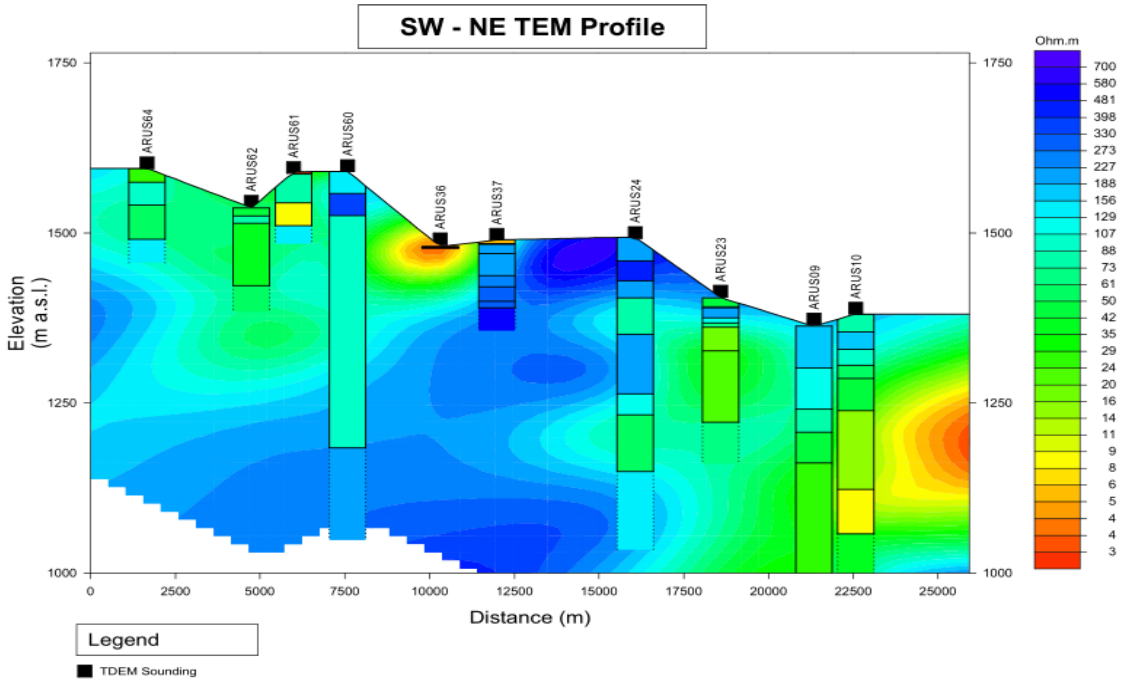
SW - NE TEM Profile
ARUS64
ARUS62
ARUS61
ARUS60
ARUS36
ARUS37
ARUS24
ARUS23
ARUS09
ARUS10
Elevation (m a.s.l.)
Distance (m)
Ohm.m
700
580
481
398
330
273
227
188
156
129
107
88
73
61
50
42
35
29
24
20
16
14
11
9
8
6
5
4
4
3
Legend
TDEM Sounding